

# THESIS

Quantum chemical studies: from semi-empirical calculations on  
large aromatic hydrocarbon networks via  
Density Functional Theory on Ru(II) intercalators in DNA,  
to highly correlated methods on silver halides

Michiko Atsumi

A Dissertation

in

Doctor of Louis Pasteur University

and

Graduate School of Humanities and Science  
Ochanomizu University

Presented to Louis Pasteur University and Ochanomizu University in partial fulfillment  
of the requirements for the degree of Doctor of Philosophy

March 2006



# THÈSE

Présentée à l'Institut de Chimie de Strasbourg  
UMR 7177 LC3 CNRS-ULP  
devant la Faculté de chimie  
de l'Université Louis Pasteur – Strasbourg I  
en vue de l'obtention du

*Doctorat de l'Université Louis Pasteur*

en chimie – spécialité chimie informatique et théorique

par

Michiko Atsumi

---

Calculs en chimie quantique : des approches semi-empiriques appliquées aux réseaux d'hydrocarbures polycycliques aromatiques, via l'étude de complexes de Ru(II) par la théorie de la fonctionnelle de la densité (DFT), aux méthodes hautement corrélées appliquées aux halogénures d'Ag (I)

---

soutenue le 2 mars 2006 devant la commission d'examen à Tokyo

Koichi Yamashita	Rapporteur, Professeur à l'Université de Tokyo, Tokyo
Shinichiro Nakamura	Rapporteur, Directeur de recherche au Mitsubishi Chemical Group Science and Technology Research Center, Inc., Yokohama
Marc Benard	Rapporteur, Directeur de recherche au CNRS, Strasbourg
Yoichi Nakatani	Examineur, Directeur de recherche au CNRS, Strasbourg
Keiko Takano	Co-directeur de thèse, Professeur à l'Université Ochanomizu, Tokyo
Chantal Daniel	Directeur de thèse, Directeur de recherche au CNRS, Strasbourg



お茶の水女子大学大学院

博士後期課程 学位論文

大型不飽和共役系ネットワーク、  
DNA へのルテニウム錯体の挿入、  
及び銀ハロゲン化物に関する量子化学計算

2006 年 3 月

お茶の水女子大学大学院人間文化研究科  
複合領域科学専攻

渥美裕子



*A ma famille*

En souhaitant que toutes le oeuvres 'brilliantes et lumineuses' rendent

l'être humain heureux

光彩陸離たる全ての研究が人々を幸せにすることを願って

2005年12月

渥美裕子

Michiko Atsumi





## *Acknowledgements*

First, I would like to thank my supervisors, Dr. Chantal Daniel at Louis Pasteur University and Dr. Keiko Takano at Ochanomizu University, for their invaluable support. Their abundant knowledge has taught me that science can be exciting.

Dr. Leticia González at Freie Universität Berlin has been my advisor since I went to Louis Pasteur University. She has a wide range of experience in quantum chemistry and my research has benefited from her advice.

Special appreciation goes to Dr. Tetsuya Taketsugu at Hokkaido University, with whom I began to study quantum chemistry. He directed me to this very exciting area in quantum chemistry.

For their support and advice, which have improved the quality of my work, and their important contributions over 3 years.

I would like to express my sincere appreciation to Professor emeritus Haruo Hosoya at Ochanomizu University for guiding me to studies. I am great thankful to Dr. Noriko Yamaguchi at Tokyo Woman's University and Professor emeritus Isao Tomita at Ochanomizu University for their advice. I would like to express my deepest thanks to Professor emeritus Mitsuo Sakai at the University of Tokyo for his advice since I decided to go France.

I would like to thank the member of my thesis committee, Professor Yoichi Nakatani at Louis Pasteur University, Dr. Marc Benard at Louis Pasteur University, Professor Koichi Yamashita at the University of Tokyo, Research Manager Dr. Shinnichiro Nakamura at Mitsubishi Chemical Group, Professor Hajime Nagano at Ochanomizu University, Professor Yutaka Fukuda and Professor Katsuyoshi Kobayashi, for their insightful comments and helpful suggestions.

Great appreciation goes to all the members at Quantum Chemistry Laboratory at Louis Pasteur University and Physical Chemistry Laboratory at Ochanomizu University,

for making the laboratories an enjoyable place to work.

I am particularly appreciative of French government since I was the beneficiaries of French government 2004-2005. I am also grateful to financial support of Ochanomizu University and Tokyo Woman's Christian University.

Lastly, I am dearly thankful to my family for the help and support they have provided over the years.

Michiko Atsumi

December 2005

## *Remerciements*

Je me permets d'écrire cette partie *Remerciements* sans demander la correction du français. Il est particulièrement à noter que cette thèse a été rédigée par cette manière, c'est-à-dire la mienne.

Au terme de ces trois années je remercie vivement Dr Chantal Daniel, directrice de ma thèse au sein du Laboratoire de Chimie Quantique à Strasbourg CNRS/Université Louis Pasteur. Je joins à ce remerciement Dr Keiko Takano, co-directrice de ma thèse au sein de l'Université Ochanomizu. Elles m'ont suivie pendant ces trois années avec grande disponibilité. Je tiens à remercier Dr Leticia González de Freie Universität Berlin. J'ai également à remercier Professeur Joern Manz de Freie Universität Berlin. J'exprime ma vive gratitude au Professeur Dr Yoichi Nakatani à CNRS/Université Louis Pasteur, Dr Marc Benard à CNRS/Université Louis Pasteur, Professeur Dr Koichi Yamashita à l'Université de Tokyo, Directeur de recherche Dr Shinnichiro Nakamura à Mitsubishi Groupe Chimique, Professeur Dr Hajime Nagano à l'Université Ochanomizu, Professeur Dr Yutaka Fukuda à l'Université Ochanomizu et Professeur Dr Katsuyoshi Kobayashi à l'Université Ochanomizu pour l'honneur qu'ils m'a fait en acceptant d'être rapporteur de ma thèse.

Le grand remerciement aux membres du Laboratoire de Chimie Quantique et Modélisation et de Simulations Moléculaires à Strasbourg :

Merci à Chantal, Alain D, Alain S, Elise, Marie-Madleine, Marc, Trond, Hélène, Nadia, Lylie, Sylvie, Emmanuelle, Elizabeth, Carole, Julien, Sébastien D, François-Paul, Sébastien V, Thomas, Boka, Alex, Georges, Alexandre, Rachel, Frank, Guillaume, Nicolas, Cédric, Denis et Alain! Jere Jef, Aziz! Gracias a Antonio y Xavier! Danke für Radovan! Shukran Ali! Dakejem, Miro!

Je vous adore !!!

Vous êtes ma famille de FRANCE !!!

HAPPY !!

Michiko

## 謝辞

本研究を進めるにあたり、熱心なご指導を賜りましたお茶の水女子大学人間文化研究科複合領域科学専攻（日本）の鷹野景子先生、ルイ・パスツール大学量子化学研究所（フランス）のシャンタル・ダニエル先生に深く感謝いたします。先生方からは研究の進め方や考え方を教えていただき、お忙しい中にも多くの時間をさいていただきました。先生方のご指導がなければ、研究を進めることが出来ませんでした。心より感謝いたします。またベルリン自由大学のヨルン・マンツ博士、レティシア・ゴンザレツ博士には量子化学の重要性、そして明るく楽しく研究に取り組むということを教えていただきました。本当にありがとうございました。

そして量子化学の基本から応用までを細かく教えてくださった北海道大学の武次徹也先生に御礼を申し上げたいと思います。

お茶の水女子大学名誉教授の細矢治夫先生には、さまざまなアドバイスをいただきました。そして東京女子大学教授山口則子先生、お茶の水女子大学名誉教授富田功先生には化学の考え方を教えていただきました。ありがとうございました。

東京大学名誉教授の坂井光夫先生には渡仏を決心して以来、いろいろと心強いアドバイスを頂戴し、学問ばかりでなく、フランスで文化を味わうことの大切さを教えていただきました。本当にありがとうございました。

永野肇先生には在仏中に励ましのお言葉をいただき、大変感謝しております。

博士論文審査委員になってくださったルイ・パスツール大学の中谷陽一先生、ルイ・パスツール大学のマーク・ベナル先生、東京大学の山下晃一先生、株式会社三菱化学科学技術計算研究センター所長の中村振一郎先生、お茶の水女子大学の福田豊先生、お茶の水女子大学の小林功佳先生に感謝いたします。

またルイ・パスツール大学では後藤真里さんをはじめ、多くの日本人研究者の方々に大変お世話になりました。本当にありがとうございました。

フロリダ大学の土屋敬史さんにはMOLCASの基底関数についていろいろ教わり、また実際に基底関数を作っただき、大変感謝しております。

東京大学の澁田靖さん、千足昇平さんにはカーボンナノチューブについてディスカッションしてくださり感謝しております。

2004-2005 年度フランス政府給費生として補助をしてくださったフランス政府に、またお茶の水女子大学そして東京女子大学から奨学金を頂戴したことに感謝いたします。

大型計算機の利用を許可してくださった大学共同利用機関法人自然科学研究機構分子科学研究所、ルイ・パスツール大学量子化学研究所、そしてベルリン自由大学の方々に感謝いたします。

お茶の水女子大学物理化学研究室、ルイ・パスツール大学量子化学研究所の皆さんには、いろいろとお世話になり、充実した研究生活が送れましたことを心より深く感謝いたします。

特別、朱振霞小姐、在校期間、为你的好心感谢你。你的烹调法非常真好!!

最後に家族と、そして日本とヨーロッパ、アメリカで出会った全ての人々に心より感謝いたします。

2006年3月  
渥美裕子

# List of Publications

## Journals

1. H. Hosoya, S. Iwata, M. Murokoshi, M. Atsumi Graph-theoretical analysis of tunnelling electron transfer in large aromatic hydrocarbon networks *J. Chem. Inf. Comput. Sci.* 2001, 41, 512-516.
2. M. Atsumi, L. González, C. Daniel A DFT and TD-DFT theoretical study of Ru(II) polypyridyl complexes used as intercalators in DNA *in preparation*.
3. M. Atsumi, C. Daniel, L. González Can ab initio and DFT methods describe the ground and excited states of silver dihalides ? Benchmark calculations on the neutral and anion AgClBr *in preparation*.

## International Conference

1. M. Atsumi, C. Daniel, L. González A DFT study on the electronic structure and photophysics of the DNA intercalator  $[\text{Ru}(\text{TAP})_2\text{dppz}]^{2+}$  PACIFICHEM2005, Hawaii, USA, 2005
2. M. Atsumi, C. Daniel, L. González A DFT study on the electronic structure and photophysics of the DNA intercalator  $[\text{Ru}(\text{TAP})_2\text{dppz}]^{2+}$  European Summer school in Quantum Chemistry (ESQC-05)2005, Palermo, Italy, 2005
3. M. Atsumi, C. Daniel, L. González A DFT study on the electronic structure and photophysics of the DNA intercalator  $[\text{Ru}(\text{TAP})_2\text{dppz}]^{2+}$  5ème Rencontre des Chimistes Théoriciens du Grand Est, Reims, France, 2005



4. C. Daniel, M. Atsumi, L. González A DFT study on the electronic structure and photophysics of the DNA intercalator  $[\text{Ru}(\text{TAP})_2\text{dppz}]^{2+}$  16th International Symposium on the Photochemistry and Photophysics of Coordination Compounds, California, USA, 2005
5. M. Atsumi, C. Daniel, L. González A DFT study on the electronic structure and photophysics of the DNA intercalator  $[\text{Ru}(\text{TAP})_2\text{dppz}]^{2+}$  Computational Tools for Molecules, Clusters and Nanostructures (An International Conference in Honor of Reinhart Ahlrichs), Karlsruhe, Germany, 2005
6. M. Atsumi, K. Takano, S. Tajima, and H. Hosoya Analysis of Tunneling Electron Transfer in Large Polycyclic Aromatic Hydrocarbon Networks Japan-Korea Women's College Science Educational Joint Forum, Tokyo, Japan, 2003

#### **National Conference**

1. M. Atsumi, K. Takano, S. Tajima, and H. Hosoya Analysis of Tunneling Electron Transfer in Large Polycyclic Aromatic Hydrocarbon Networks Johokagaku Touronkai, Tokyo, Japan, 2003
2. M. Atsumi, K. Takano, S. Tajima, and H. Hosoya Analysis of Tunneling Electron Transfer in Large Polycyclic Aromatic Hydrocarbon Networks Bunshikozo Touronkai, Tokyo, Japan, 2000

## ABSTRACT

### **Part I. Semi-empirical calculations on polycyclic aromatic hydrocarbon networks**

The aim of the work performed at Ochanomizu University (Tokyo) was the study and analysis of electron transfer processes in polycyclic aromatic hydrocarbons (PAH). Our research was oriented more specifically to the case of 'abnormal' electron transfer or '*Tunnelling Electron Transfer*' (TET) which corresponds to the transport of a large amount of  $\pi$  electrons from a remote site of the network to an electronegative nitrogen atom. In a first step this phenomena has been analysed by means of diagrams representation based on Kekule structures representative of the elementary units of the network. The limits of the '*organic electron*' model in the understanding of the transfer properties in conjugated hydrocarbons have been put in evidence by means of molecular orbitals calculations (Hückel theory). In particular, this simple model was unable to explain the observed changes at the level of the  $\pi$  electrons transfer when replacing a carbon atom by a nitrogen atom. The electronic structure of different classes of PAH networks (parallelograms, perylene, coronene) has been investigated by means of semi-empirical methods PM3 (*Parametric Model 3*), AM1 (*Austin Model 1*) et MNDO (*Modified Neglect of Differential Overlap*). The trends related to the amount, type and routes of electrons transfer in the network in term of groups of atoms pairs have been deduced from these calculations.

On the basis of this approach it has been possible to extend our investigations to the graphite and carbon nanotube. The aim of this work is to understand the role of the metal catalyst in the growth mechanism of the nanotube.

### **Part II. Theoretical study of the spectroscopic and photophysical properties of ruthenium (II) complexes used as luminescent probes by intercalation in DNA.**

The goal of this research project is the determination of the electronic and structural properties of the  $[\text{Ru}(\text{bpy})_2\text{dppz}]^{2+}$  (bpy = 2,2'-bipyridine; dppz = dipyrido[3,2 :a-2',3' :c]-phenazine) complexes used as molecular switches by specific intercalation in active sites of DNA double helix. The access to spectroscopic and photophysical properties of the isolated metal complex and in its biological environment will help at analysing the mechanism of control of the luminescent probe.

The experiments reported in this field of research in the early 90's have shown that the yield of luminescence, null in aqueous solution, is function of DNA conformation at the intercalation site at the level of the dppz bases pair interaction. Recent experiments of flash photolysis reported for  $[\text{Ru}(\text{bpy})_2\text{dppz}]^{2+}$  (bpy = 2,2'-bipyridine; dppz =

dipyrido[3,2-a:2',3'-c]-phenazine) in aqueous solution and in different nucleotides point to a mechanism implying a coupled electron / proton transfer process.

The structures of the  $[\text{Ru}(\text{TAP})_2\text{dppz}]^{2+}$ ,  $[\text{Ru}(\text{phen})_2\text{dppz}]^{2+}$  and  $[\text{Ru}(\text{TAP})_3]^{2+}$  (dppz = dipyrido [3,2-*a*:2',3'-*c*]-phenazine; TAP = 1,4,5,8-tetraazaphenanthrene; phen = 1,10-phenanthroline) complexes have been optimized in the vacuum by means of DFT (B3LYP). The results have been validated by the theoretical and experimental structures of  $[\text{Ru}(\text{TAP})_3]^{2+}$ . The theoretical absorption spectra of  $[\text{Ru}(\text{TAP})_2\text{dppz}]^{2+}$  and  $[\text{Ru}(\text{phen})_2\text{dppz}]^{2+}$  have been analysed on the basis of TD-DFT calculations. The theoretical spectra are very different for the two complexes. In the presence of the phen ligand the spectrum is characterized by a series of MLCT states between 423 nm and 378 nm corresponding mainly to excitations from the ruthenium to the phen ligands with a MLCT state ( $\text{Ru} \rightarrow \pi^*_{\text{dppz}}$ ) calculated at 410 nm with an oscillator strength of 0.1747. This state has been put in evidence experimentally. The first Ligand-to-Ligand-Charge-Transfer (LLCT) state with a significant oscillator strength is calculated at 303 nm and corresponds to a  $\pi_{\text{dppz}} \rightarrow \pi^*_{\text{dppz}}$  excitation. This spectrum is very different from the one calculated for the complex with TAP ligands characterised by the presence of Intra-Ligand (IL) and LLCT states between 429 nm and 372 nm. The first MLCT ( $\text{Ru} \rightarrow \pi^*_{\text{dppz}}$ ) states with significant oscillator strengths are calculated between 323 nm and 304 nm. Moreover calculations have been performed in order to take into account the solvent effects (Polarized Continuum Model) as well as the biological environment within the QM/MM approach.

### **Part III. Electronic structure and spectroscopy of XAgY (X=Y=F; X=Cl, Y=Br).**

The electronic structure of the ground state and low-lying spectroscopic states of neutral and ionized AgClBr have been investigated by means of *ab initio* methods (HF, CASSCF/CASPT2, CCSD) and Density Functional Theory (DFT, TD-DFT). A detailed study of the basis sets (all-electrons or valence) and pseudopotentials (ECP: Effective Core Potentials or AIMP: Ab Initio Model Potentials) influence has been performed in order to determine the best computational strategy. We have shown that the HF or DFT methods were not able to describe correctly the doublet electronic ground state of the neutral species, five open shell states being nearly degenerate. This wrong description of the bonding has been correlated to an erroneous charge distribution on the three centres (Ag, Cl, Br). This effect is even more dramatic in the case of the use of AIMP. In order to describe correctly these molecules we have shown that it is necessary to introduce electronic correlation at the CASSCF/CASPT2 level. A comparative study of the AgClBr and AgF<sub>2</sub> molecules has been performed.

## RÉSUMÉ

### **Partie I. Calculs semi-empiriques sur des hydrocarbures polycycliques aromatiques**

Les travaux réalisés à l'université de Ochanomizu (Tokyo) avaient pour but l'étude et l'analyse de processus de transfert d'électrons dans un réseau d'hydrocarbures polycycliques aromatiques (PAH). Nous nous sommes intéressés, en particulier, au cas du transfert d'électron dit 'anormal' ou 'Tunnelling Electron Transfer' (TET) qui se traduit par le transport d'une grande quantité d'électrons  $\pi$  des régions les plus éloignées du réseau vers un atome d'azote électronégatif. Ce phénomène a été analysé dans un premier temps à l'aide de diagrammes sur la base de structures de Kekulé représentant des modules du réseau. Les limites du modèle de *l'électron organique*, proposé pour expliquer les propriétés de transfert dans les hydrocarbures conjugués avant l'avènement de la chimie quantique, ont été mises en évidence par des calculs d'orbitales moléculaires (théorie de Hückel). En particulier ce modèle très simple n'a pu expliquer les modifications observées au niveau du mode de transfert des électrons  $\pi$  lorsqu'un atome de carbone était substitué par un atome d'azote. La structure électronique de différents types de réseaux PAH (parallélogramme, pérylène, coronène) a été étudiée par les méthodes semi-empiriques PM3 (*Parametric Model 3*), AM1 (*Austin Model 1*) et MNDO (*Modified Neglect of Differential Overlap*). Ces calculs ont permis d'estimer et de donner des tendances concernant l'importance, la nature et le parcours des transferts d'électrons dans le réseau en terme de groupes de paires d'atomes.

Cette approche nous a permis d'étendre nos investigations à l'étude du graphite et enfin au nanotube de carbone. L'objectif de ce travail est de comprendre le rôle du catalyseur métallique dans le mécanisme de croissance d'un nanotube.

### **Partie II. Etude théorique des propriétés spectroscopiques et photo physiques de complexes du ruthénium (II) utilisés comme sonde luminescente par intercalation dans les hélices d'ADN**

L'objectif de ce projet de recherche est la détermination des caractéristiques électroniques et structurales des complexes de type  $[\text{Ru}(\text{bpy})_2\text{dppz}]^{2+}$  (bpy = 2,2'-bipyridine; dppz = dipyrido[3,2 :a-2',3' :c]-phenazine) utilisés comme interrupteurs moléculaires par intercalation spécifique dans les sites actifs des hélices d'ADN. L'accès aux propriétés spectroscopiques et photophysiques du complexe métallique isolé et dans son environnement biologique permet d'analyser le mécanisme qui contrôle le fonctionnement de la sonde luminescente. Les expériences menées dans

ce domaine de recherche à partir des années 90 ont montré que le rendement de luminescence du complexe, nul en solution aqueuse, est fonction de la conformation de l'ADN au site d'intercalation, c'est-à-dire au niveau de l'interaction entre le ligand dppz et la paire de bases. De récentes expériences de photolyse éclair reportées pour le complexe  $[\text{Ru}(\text{TAP})_2\text{dppz}]^{2+}$  (TAP = 1,4,5,8-tetraazaphenanthrene) en solution aqueuse et dans différents nucléotides ont mis en évidence un mécanisme impliquant un processus de transfert d'électron / proton couplé.

Les structures des complexes  $[\text{Ru}(\text{TAP})_2\text{dppz}]^{2+}$ ,  $[\text{Ru}(\text{phen})_2\text{dppz}]^{2+}$  et  $[\text{Ru}(\text{TAP})_3]^{2+}$  (dppz = dipyrido [3,2-*a*:2',3'-*c*]-phenazine ; TAP = 1,4,5,8-tetraazaphenanthrene ; phen = 1,10-phenanthroline) ont été optimisées dans le vide au niveau DFT (B3LYP). Les résultats ont été validés à partir des structures théoriques et expérimentales de  $[\text{Ru}(\text{TAP})_3]^{2+}$ . Les spectres d'absorption théoriques ont été analysés sur la base de calculs TD-DFT pour  $[\text{Ru}(\text{TAP})_2\text{dppz}]^{2+}$  et  $[\text{Ru}(\text{phen})_2\text{dppz}]^{2+}$ . Les spectres théoriques sont très différents dans les deux complexes. En présence du ligand phen le spectre est caractérisé par une série d'états MLCT entre 423 nm et 378 nm correspondant principalement à des excitations du ruthénium vers les ligands phen avec un état MLCT ( $\text{Ru} \rightarrow \pi^*_{\text{dppz}}$ ) calculé à 410 nm avec une force d'oscillateur de 0.1747. Cet état a été mis en évidence expérimentalement. Le premier état Ligand-to-Ligand-Charge-Transfer (LLCT) avec une force d'oscillateur significative apparaît à 303 nm et correspond à une excitation  $\pi_{\text{dppz}} \rightarrow \pi^*_{\text{dppz}}$ . Ce spectre est très différent de celui calculé pour le complexe avec les ligands TAP caractérisé par la présence d'états Intra-Ligand (IL) et LLCT entre 429 nm et 372 nm. Les premiers états MLCT ( $\text{Ru} \rightarrow \pi^*_{\text{dppz}}$ ) avec des forces d'oscillateur significatives sont calculés entre 323 nm et 304 nm.

La poursuite de ce projet passe par la prise en compte des effets de solvant et de l'environnement biologique. Des calculs sont en cours en ce qui concerne les optimisations de géométrie des complexes et dans le modèle de solvant PCM (Polarized Continuum Model) pour l'acétonitrile et l'eau. Parallèlement des calculs QM/MM ont été entrepris pour prendre en compte l'environnement biologique.

### **Partie III. Etude de la structure électronique et de la spectroscopie de composés $\text{XAgY}$ ( $\text{X}=\text{Y}=\text{F}$ ; $\text{X}=\text{Cl}$ , $\text{Y}=\text{Br}$ )**

La structure électronique de l'état fondamental et des états spectroscopiques de basse énergie des espèces neutre et ionisée de  $\text{AgClBr}$  a été étudiée par les méthodes *ab initio* (HF, CASSCF/CASPT2, CCSD) et de la fonctionnelle de la densité (DFT, TD-DFT). Une étude détaillée portant sur le choix des fonctions de base (tous-électrons ou de valence) et des pseudopotentiels de type Effective Core Potentials (ECP) ou Ab Initio Model Potentials (AIMP) a été réalisée afin de déterminer la meilleure stratégie

de calcul. Il a été montré que les méthodes de type HF ou DFT ne pouvaient décrire correctement l'état fondamental doublet de l'espèce neutre, cinq états à couche ouverte étant très proches en énergie. Cette mauvaise description des liaisons a pu être corrélée à une distribution de charge erronée, en particulier dans le cas de l'utilisation des AIMP et bases associées. Afin de décrire correctement cette molécule il a été nécessaire d'introduire la corrélation électronique au niveau CASSCF / CASPT2. Une étude comparative des molécules AgClBr et AgF<sub>2</sub> est en cours.



## 論文要旨

### Part I. 大型不飽和共役系ネットワーク

お茶の水女子大学における仕事は、Coulson と Longuet-Higgins らの摂動理論にグラフ理論的手法を組み合わせることにより、簡便な有機電子論の図式的方法の数学的基礎付けを示した細矢らの研究にはじまり、ポリアセチレンやポリアセンなどについて Coulson と Longuet-Higgins の分極率や福井の *superdelocalizability* が系の大きさを無限に大きくした時に発散することを見出したことともに、これらの理論的説明も得ている。

これらの理論的研究の中で、有機電子論や MO 理論でも説明できない  $\pi$  電子の異常な流れを示すものが多数発見された。HMO 法により、周辺構造が平行四辺形の大きなベンゼノイド系の鋭角先端部のベンゼン環の中の 1 つの炭素原子を窒素のようなヘテロ原子で置換すると、置換の位置によって、その電子移動効果がグローバルに出る場合 (Global) とローカルに出る場合 (Local) があることが見出されたのはその一例である。Global における電子移動はヘテロ原子置換した  $\pi$  電子系の最遠方よりやや近い位置の炭素原子上に最も大きく現れた。我々はこれをトンネル電子移動効果 (TET 効果、TET: Tunneling Electron Transfer) と名づけて、そのグラフ理論的な解釈を行った。

本研究では、ヘテロ原子置換を行うとその影響が分子全体に見られる Global と局所的である Local について total の電荷分布による解析を行った。電荷の値は同型の炭化水素からの差の電荷 (Mulliken charge) として求めた。すると HMO 法、半経験的方法、非経験的方法の 3 つの方法でほぼ平行関係にあることがわかった。HMO 法では  $\pi$  電子のみを扱ったが、本研究では、 $\pi$  電子と  $\sigma$  電子の電荷の流れを分けて確認を行った。全体として Global に見られる  $\pi$  電子系の大きな電子移動は  $\sigma$  電子系によって打ち消されるために、total として残った結果の数値は幾分小さくなるが、 $\pi$  電子系だけで得られた結果と同じ傾向を示すことがわかった。分子内の電子の流れは  $\pi$  電子系ではヘテロ原子置換を行った場所から対岸の中心より左に、 $\sigma$  電子系では対岸の中心付近に大きく打ち消しあう傾向がみられた。

さらにその研究を展開し、2次元共役  $\pi$  電子系の周辺構造依存性の検討を経て、その 3次元系への拡張を行う予定であるが、ナノスケール共役分子系を対象とし、 $\pi$  電子移動という観点で系統的な解析を行うところに本研究の特色がある。



## Part II. DNA へのルテニウム錯体の挿入

$[\text{Ru}(\text{TAP})_2(\text{dppz})]^{2+}$  についての光化学的性質について解析している。 $[\text{Ru}(\text{bpy})_2(\text{dppz})]^{2+}$  が 1985 年に合成されて以来、ルテニウム錯体への注目が集まっている。ルテニウム錯体は DNA の light-switch として知られ、水中において強く発光する現象が DNA やポリヌクレオチドとの相互作用と共に研究されている。DNA における light-switch の効果は、DNA 塩基対間へ挿入される dppz リガンドと金属間の charge transfer は MLCT による光化学反応に起因していると考えられている。

そして  $[\text{Ru}(\text{TAP})_2\text{dppz}]^{2+}$  を DNA に挿入する箇所は限定されることは理解できるが、これらの charge transfer をもとにした光化学的性質についての詳細は解明されていない。そこで密度汎関数法を用いて  $[\text{Ru}(\text{TAP})_2\text{dppz}]^{2+}$  の構造最適化計算を行った。 $[\text{Ru}(\text{TAP})_2\text{dppz}]^{2+}$  に関する詳細な実験構造データがないため、X 線構造解析がなされている  $[\text{Ru}(\text{TAP})_2]^{2+}$  と比較を行ったところ、よい一致が得られた。このとき、基底関数は Pseudo Potetial (MWB) をルテニウムに、D95, LanL2DZ, 6-31G\* を炭素原子と、窒素原子に使い、DFT 法による構造最適化計算を行い、基底状態での安定構造を求めた。その後それらを比較検討し、 $[\text{Ru}(\text{TAP})_2\text{dppz}]^{2+}$  について基底関数は Pseudo Potetial (MWB) をルテニウムに、6-31G\* を炭素原子と、窒素原子に使い構造最適化計算を行った。

その結果、さらに、TDDFT 法を使用し、遷移エネルギーと振動子強度を計算し、実験結果と比較を行った。これらの励起状態数の検討の後、一重項と三重項の計算結果から、光ルミネセンスの charge transfer に起因すると考えられる金属-リガンド間でのピークの帰属を行い、実験結果と比較検討した。該当分子が非常に大きいので、TDDFT 法における long-range charge transfer problem が起こり、計算結果に対して慎重な解析を行った。また、異なる計算法 (CIS) を用いて、同様に遷移エネルギーと振動子強度を計算した。

しかしいずれの場合も、塩基対からの影響、また、溶媒効果も考慮に入れていない。そこでその後、溶媒効果 (PCM ; Polarized Continuum Model) を入れた  $[\text{Ru}(\text{TAP})_2\text{dppz}]^{2+}$  の構造最適化、また ONIOM 法を用いて、 $[\text{Ru}(\text{TAP})_2\text{dppz}]^{2+}$  と 6 塩基対とをドッキングさせて系全体の charge transfer を解析し、光ルミネセンスにおけるエネルギー吸収と光放出がどの遷移に帰属されるかを詳細に検討する。

### Part III. 銀ハロゲン化物に関する量子化学計算

銀ハロゲン化物の基底状態の電子構造を *ab initio* 法 (HF, CASSCF/CASPT2, CCSD) と密度汎関数法 (DFT, TD-DFT)により、分光学的に解析し、基底関数 (all-electrons または valence) の詳細な研究、pseudopotential (ECP: Effective Core Potentials または AIMP: Ab Initio Model Potentials) の影響が最もよく表れる方法を決定する。

本研究では HF 法と DFT 法が 5 つの開殻系でほぼ縮退する neutral の電子基底状態の二重項について正確に記述することができないことを明らかにする。この結合に関する間違っただ記述は Ag, Cl, Br の誤った電荷分布に関連づけられる。そして AIMP を使うとその影響が顕著に現れる。これらの分子をより正確に記述するために CASSCF/CASPT2 レベルでの電子相関を考える必要がある。さらに本研究では AgClBr と AgF<sub>2</sub> の比較も行う。



# Contents

<i>Introduction</i> .....	1
<i>Computational Methods</i> .....	5

## Chapter 1

<b>Large aromatic hydrocarbon networks</b> .....	<b>18</b>
<b>1.1 Graphene</b> .....	<b>24</b>
1.1.1 <i>Computational Details</i> .....	25
1.1.2 <i>Electron Charge Transfer</i> .....	26
1.1.3 <i>MP2/AM1 and DFT</i> .....	29
<b>1.2 Carbon Nanotubes</b> .....	<b>30</b>
1.2.1 <i>Computational Details</i> .....	31
1.2.2 <i>Heat of formation</i> .....	33
1.2.3 <i>Molecular orbitals and energies</i> .....	34
<b>1.3 Conclusion</b> .....	<b>38</b>

## Chapter 2

<b>Density Functional Theory on Ru(II) used as intercalators in DNA</b> ....	<b>40</b>
<b>2.1 Computational Details</b> .....	<b>48</b>
2.1.1 <i>Geometry Optimization</i> .....	48
2.1.2 <i>Spectroscopy</i> .....	48
2.1.3 <i>Intercalating to DNA</i> .....	49

2.2 $[Ru(TAP)_2dppz]^{2+}$ , $[Ru(TAP)_3]^{2+}$ and $[Ru(Phen)_2dppz]^{2+}$ .....	51
2.2.1 Structure of the metal complexes .....	51
2.2.2 Spectroscopy .....	56
2.3 $[Ru(TAP)_2dppz]^{2+}$ intercalates to DNA .....	78
2.3.1 Structure of $[Ru(TAP)_2dppz]^{2+}$ and 6CG .....	78
2.4 Conclusion .....	81

## Chapter 3

Highly correlated methods on Ag(I) halides .....	82
3.1 Computational Details .....	87
3.1.1 Geometry Optimization .....	87
3.1.2 Single configuration calculations .....	87
3.1.3 Multiconfigurational calculations .....	89
3.2 AgClBr .....	91
3.2.1 Structures of the metal complexes .....	91
3.2.2. Electronic ground state .....	93
3.2.3. Spectroscopy .....	95
3.3 AgF <sub>2</sub> .....	104
3.3.1 Structures of the metal complexes .....	104
3.3.2. Electronic ground state .....	105
3.4 Conclusion .....	109
<b>Conclusion</b> .....	<b>112</b>
<b>Bibliography</b> .....	<b>116</b>

# Acronym

AIMP	Ab initio model potential
AM1	Austin Model 1
ANO	Atomic natural Orbital
ANO-DK3	Atomic natural orbital third-order Douglas–Kroll
ANO-RCC	Atomic natural orbital relativistic correlation consistent
B3LYP	Becke 3-term functional; Lee, Yang, Parr exchange
CASPT2	Complete active space second order perturbation theory
CASSCF	Complete active space self-consistent field
CCSD	Coupled cluster with singles and double excitation theory
CCSD(T)	Coupled-cluster singles doubles and non-iterative triples correction with singles and double excitation theory
CG-AIMP	Cowan-Griffin relativistic core ab initio model potential
CI	Configuration Interaction
CIS	CI-Singles theory
DFT	Density functional theory
DNA	Deoxyribonucleic acid
ECP	Effective core potential
HF	Hartree-Fock theory
HW	Hay and Wadt
KS	Kohn-Sham
LANL2DZ	Los Alamos National Laboratories double zeta
LLCT	Ligand to ligand charge transfer
MC	Metal centered
MCSCF	Multiconfigurational self-consistent field
MLCT	Metal to ligand charge transfer

MM	Molecular mechanics
MNDO	Modified neglect of differential overlap
MP2	Møller-Plesset perturbation theory of second order
MS-CASPT2	Multistate complete active space second order perturbation theory
MWB	Multielectron fit to Wood–Boring orbital energies
NP-AIMP	Relativistic no-pair second-order Douglas-Kroll core ab initio model potential
NR-AIMP	Non-relativistic core ab initio model potential
NRECP	Non-relativistic effective core potentials
ONIOM	Our own N-layered integrated molecular orbital + molecular mechanics
PAH	Polycyclic aromatic hydrocarbon
PCM	Polarizable continuum model
PM3	Parametric method number 3
QM	Quantum mechanics
RAS	Restricted active space
RECP	Relativistic effective core potentials
SS-CASPT2	Singlestate complete active space second order perturbation theory
SWNT	Single-walled carbon nanotube
TD-DFT	Time dependent density functional theory
UFF	Universal force field
UV	Ultraviolet





## *Introduction*

Quantum chemistry has emerged as an important tool for investigating a wide range of problems in chemistry. Recently, due to the development of computational methods and more powerful computers, it has become possible to solve chemical problems that only a few years ago seemed for ever beyond the reach of a rigorous quantum-mechanical treatment. Today quantum mechanical methods are routinely applied to problems related to molecular structure and reactivity, and spectroscopic parameters calculated quantum-mechanically are often useful in the interpretation of spectroscopic measurements. It is, in principle, possible to use one very accurate method and apply it to the molecules. However such methods are well-known and available in many programs, the computational cost of their use grows factorially with the number of electrons. Therefore, a great number of approximate methods strive to achieve the best trade-off between accuracy and computational cost.

It brings to calculate large molecules such as carbon nanotubes and biomolecules even the small molecule high precisely.

The discovery of single-walled carbon nanotube has promised a new field of science and technology with their elongated fullerene structure and good mechanical properties and unique structural, electronic, thermal, and optical characteristics. It has attracted intense interest in recent years due to their suitability for a wide range of applications though there is no large-scale and the effect of the edge which corresponds to catalyst have been developed [1]. In this study proposes a model containing graphene to account for the growth of carbon nanotubes considering the effect of the periphery structure.

The integration of chemistry and physics was almost complete, with chemical properties explained as the result of the electronic structure of the atom. However, though some principles deduced from quantum mechanics were able to predict qualitatively some chemical features for biologically relevant molecules, they were more a collection of rules and recipes than rigorous *ab initio* quantitative methods. This kind of approach culminated in the physical modelling of the DNA molecule.

Therefore photobiology is the study of the effects of light on the field which encompasses many biological phenomena, including photosynthesis, visual processing, circadian rhythms, and ultraviolet radiation effects. It makes that the metal complex such as a Ru(II) complexes intercalating DNA pay much attention to the photobiological field [2]. Interestingly enough the DNA structure which the metal complexes intercalated depends on the ligands.

The transition metal dihalides  $MX_2$  pose fascinating structural problems which are at the limit of present day experimental and theoretical techniques. Experimental data were obtained for several of these molecules almost 50 years ago and confidently interpreted in terms of a ligand field model, which was very much in vogue at the time. However, the quality of the data was poor and it is not surprising to discover, with the benefit of hindsight, that many aspects of these early interpretations are erroneous. Furthermore  $MX_2$  form high temperature molecules which are generated in the gas phase well above 1000 K. Under these conditions, many vibrational and rotational levels are populated. They result in extremely complex electronic and vibration – rotation spectra, which are difficult to solve and to interpret.

In addition the calculation by *ab initio* methods of the ligand field splitting in transition-metal complexes continues to be a challenge for quantum chemistry.  $AgX_2$  is considered as an example of  $MX_2$  [3].

The purpose of this thesis is to exploit the theoretical methods from semi empirical to highly correlated approaches for elucidating the structure, spectroscopy, synthesis of electronic structure of ground and excited states and of triatomic silver compounds with complex electronic configurations.

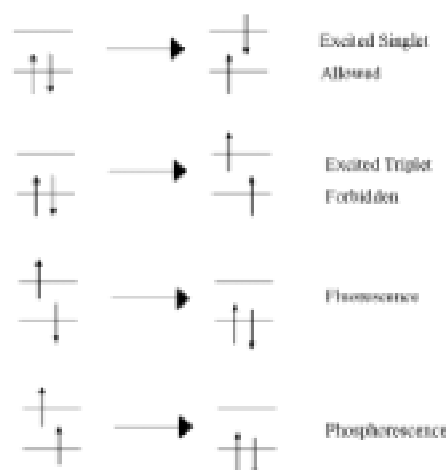
We aimed at reaching the limit of the correlated strategies available nowadays able to overcome difficulties such as the size of single determinant, description of excited states at long range in biological environment, and near degeneracy effects.

In this manuscript the major work dedicated to the analysis of excitedstates properties appears in Chapter 2 and Chapter 3.

The purpose of this thesis is to apply the quantum chemistry from semi empirical approaches to highly correlated methods for elucidating structures, spectroscopy, and physico-chemical properties in various chemical systems. Within this context we have to handle a variety of theoretical difficulties such as near-degeneracy effects ( $AgX_2$ ),

excited states calculations (Ru(II) complexes), physico-chemical properties in large systems (nanostructures) and biological environment

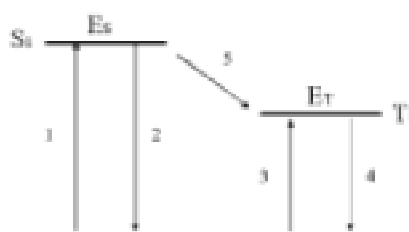
The absorption of a photon in the visible/UV domain of energy leads to the excitation of an electron from lower electronic energy level to higher one. The excitation of a single electron from its spin-paired singlet ground state to an empty orbital results in the formation of an excited state having electrons in two orbitals, each of which now contains a single unpaired electron. The excitation process may involve an allowed transition whereby the electron being transferred from the lower energy to the higher energy orbital does so without undergoing spin flip. Such an excitation pathway results in the formation of an excited singlet where the spins of the electron are in opposite directions in the two singly occupied orbitals. Alternatively, excitation process may involve a forbidden transition whereby the electron being transferred to the higher energy orbital does so by a pathway that involves a spin flip. Such an excitation pathway leads to the formation of an excited state triplet where the spins are now in the same direction in the two orbitals. The reverse deexcitation processes from these excited states back to the ground state can be understood on the basis of the Pauli principle. The deexcitation from singlet excited state is an allowed process with the resulting ground state having the electron spins paired in a single orbital. As a consequence, the lifetimes of singlet excited states are short.



By contrast, the deexcitation of a triplet excited state is a forbidden process because direct electron transfer from higher level orbital will result in a ground state having two electrons in the lower level orbital that have parallel spins, violation of the Pauli principle. As a result the lifetimes of triplet excited states are long.

A state energy diagram shows the relative energy levels of ground state  $S_0$ , the excited

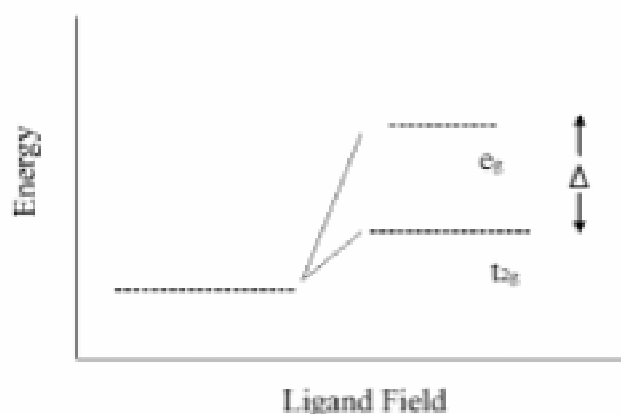
singlet states  $S_1$ , and the excited triplet states  $T_1$  of the molecule. The metal compounds measurement of the absorption and emission spectra either at low temperatures or under the influence of a magnetic field may be necessary to make these assignments. Allowed transitions are restricted to singlet-singlet or triplet-triplet excitations within the limit of a non-relativistic description which does not include spin-orbit effects.



Transitions between ground and excited states: 1. singlet-singlet absorption; 2. fluorescence; 3. singlet-triplet absorption; 4. phosphorescence; 5. intersystem crossing.

Allowed transitions are identified by large extinction coefficient, and forbidden transitions by small extinction coefficient values.

Considering the spectrochemical series and group theory, the energy level of the d orbitals in a hexacoordinate octahedral transition metal complex such as Ruthenium(II) and Ag(I) depend on both the individual metal and the ligands. In the free atom in the gas phase the five d orbitals  $d_{xy}$ ,  $d_{xz}$ ,  $d_{yz}$ ,  $d_{x^2-y^2}$ , and  $d_{z^2}$  are degenerate in energy. In an octahedral ligand field these orbitals split in the degenerate  $t_{2g}$  ( $d_{xy}$ ,  $d_{xz}$ ,  $d_{yz}$ ) and  $e_g$  ( $d_{x^2-y^2}$ ,  $d_{z^2}$ ) sets of orbitals. The energy gap between these sets of degenerate orbitals is the ligand field splitting  $\Delta$ . The value of  $\Delta$  increases by approximately 40% as one moves from the first (3d) to the second (4d) to the third row transition metal ions. A molecular orbital diagram for an octahedral complex incorporates the energy levels of both the metal ion and ligand orbitals [2].



## ***Computational Methods***

Quantum mechanics provides the possibility for the complete description of the electronic properties of molecular systems, their structure, reactivities, and so on. Therefore semi-empirical method and *ab initio* molecular quantum mechanics have developed into separate and distinct areas of investigation. The first  $\pi$  electron systems is the famous Hückel method. The overlap between orbitals on different centers is neglected. After the Hückel method the various semiempirical methods were soon followed by a series of more sophisticated all-valence-electron methods which include electronic repulsion explicitly in addition to a specification of the core attraction integrals.

Meanwhile for application of *ab initio* and DFT methods, modeling techniques that are used in studying photochemical mechanisms are initiated by light rather than thermal energy and limited to those that can describe excited states correctly. Understanding photochemical mechanisms requires the knowledge of the molecular geometry on both the excited and ground states. From the point of view of computational chemistry, this force field is usually expressed in terms of the excited and ground state potential energy surfaces. The goal of a computational approach to the photochemical mechanisms is the complete description of what happens at the molecular level from the absorptive act to the product. The goal presents a considerable challenge for computational chemistry and has been implemented in widely distributed programs such as Gaussian [4] [5] and MOLCAS [6].

## I. Variational methods

**Hartree-Fock Theory.** *The Hartree-Fock wave function* is the cornerstone of *ab initio* electronic structure theory. It is obtained by minimizing the expectation value of the electronic energy with respect to the orbitals occupying a single Slater determinant or more generally a single CSE, containing several such determinants in a fixed linear combination. The Hartree-Fock wave function yields total electronic energies that are in a error by less than 1% and wide range of important molecular properties such as dipole moments, electronic polarizabilities, electronic excitation energies, magnetizabilities, force constants and nuclear magnetic shieldings which are usually reproduced to within 5-10% accuracy. Molecular geometries are particularly well reproduced and are mostly within a few picometers of the equilibrium structure.

The Hartree-Fock wave function is often used in qualitative studies of molecular systems, particularly larger systems. Indeed, the Hartree-Fock wave function is still the only wave function that can be applied routinely to large systems, and systems containing several hundred atoms have been studied at this level of approximation. For accurate, quantitative studies of molecular systems, the Hartree-Fock wave function is by itself not useful but it constitutes the starting point for more accurate treatments. The nonvariational Møller-Plesset and coupled-cluster approaches, for example, are both based on the premise that the Hartree-Fock function represents a good zero-order approximation to the true wave function and may in fact be viewed as yielding corrections to the Hartree-Fock state.

The Slater determinant appears to be a reasonable approximation for the many-electron wave function. However, the orbitals that define this wave function still have to be determined. We therefore apply the variation principle to the energy expression obtained with such a wave function, with the tacit assumption that the orbitals leading to the lowest energy are the best in a general sense. As usual when extremum values are sought, we may suspect that differential calculations will lead to the desired goal, and we therefore change the orbitals by a small (infinitesimal) amount,  $\varphi_i \rightarrow \varphi_i + \delta\varphi_i$ . This leads to a change in the total wave function  $\Psi \rightarrow \Psi + \delta\Psi$ , as well as in the energy expression [8 – 10,12,13].

**CASSCF.** We consider here the generalization of the Hartree-Fock wave function to systems dominated by more than one electronic configuration: the *multiconfigurational self-consistent field* (MCSCF) wave function. This flexible model may be useful for describing the electronic structure of bounded molecular systems, in particular for excited states. Perhaps more important, however, is its ability

to describe bond breaking and molecular dissociation processes. In MCSCF theory, the wave function is written as a linear combination of determinants or CSFs, whose expansion coefficients are optimized simultaneously with the MOs according to the variation principle. The MCSCF wave function is well suited to studies of systems involving degenerate or nearly degenerate configurations, where static correlation is important. Such situations are usually encountered in the description of reaction processes where chemical bonds are being broken, but sometimes also ground-state molecular systems at the equilibrium geometry. MCSCF wave functions are therefore indispensable in many situations, although there are often considerable difficulties associated with their optimization. Moreover, it has proved difficult to generalize MCSCF theory in such a way that dynamical correlation effects can be calculated accurately for multiconfigurational electronic systems, although the application of second-order perturbation theory to MCSCF wave function has been quite successful. Usually, the greatest difficulty faced in setting up an MCSCF calculation is the selection of configuration space. The bonding and antibonding configurations are the only ones contribute appreciably to the wave function in the course of the dissociation. For more complicated molecules, however, the selection of a suitable configuration space can be very difficult – indeed, even for rather small systems, it is often impossible to generate an MCSCF configuration space sufficiently flexible to describe the physical process and yet sufficiently small to be computationally tractable. The selection of MCSCF configurations is usually not carried out by inspection of the individual configurations. Instead, whole classes of configurations are simultaneously selected according to subspaces containing the inactive, active and secondary (virtual) orbitals. Whereas the inactive orbitals are doubly occupied and the virtual orbitals unoccupied in all configurations, the active orbitals have variable occupancies of 0, 1, or 2. The MCSCF expansion is then obtained by disturbing the active electrons in all possible ways among the active orbitals. In the final optimized state, the active orbitals therefore have nonintegral occupancies between 0 and 2. This method is known as *Complete Active Space SCF (CASSCF)* method. Note that a CAS wave function may be regarded as FCI wave function in a limited but variationally optimized active orbital space: when the active space is empty, the CAS wave function reduces to the Hartree-Fock wave function. As for any full CI expansion, the CASSCF becomes too large even for quite small active spaces. A variation of the CASSCF procedure is *Restricted Active Space Self-Consistent Field (RASSCF)* method. Here the active MOs are further divided into three sections, RAS1, RAS2, and RAS3, each having restrictions on the occupation numbers (excitations) allowed. The RAS1 space consists of MOs which are doubly occupied in the Hartree-Fock reference determinant, the RAS2 has both occupied and unoccupied orbitals, while the RAS3 space consist of

MOs which are empty in the Hartree-Fock determinant. Configurations in the RAS2 space are generated by a full CI, analogous to CASSCF approach, and additional configurations are generated by allowing for example a maximum of two electrons to be excited from the RAS1 and maximum of two electrons to be excited to the RAS3 space. In essence, atypical RASSCF procedure thus generate configurations by a combination of a full CI in a small number of MOs (RAS2) and a CISD in a somewhat larger MO space (RAS1 and RAS3). The full CI expansion within the active space severely restricts the number of orbitals and electrons that can be treated by CASSCF method. In a CASSCF type wave function the CI coefficients do not have the same significance as for a single reference CI based on Hartree-Fock orbitals [11-14].

**CIS.** *CI-Singles theory* is an adequate zeroth-order treatment for many of the excited states of molecules. Treatments of large molecular systems can be benefitted by the avoidance of integral storage and transformation, and thus the CI-singles method has a wide range of applicability. A satisfactory exploration of potential energy surfaces and accurate electronic properties of excited states are possible by the use of analytic CI-singles gradients. We can further conclude that the success of the CI-singles method often depends critically on the chosen basis set. Diffuse (Rydberg like) excited states usually require the addition of one or two diffuse functions to split-valence basis set. Without these functions excitation energy may be much higher than experimental results. The effect of adding polarization functions often decreases the accuracy of adiabatic and vertical transition energies while increasing the accuracy of excited state potential energy surface. This can be traced to the fact that the presence of these functions causes the ground-state reference energies to be lowered to a greater extent than the excited state energies. Even though the energy difference between two states may not correlate well with experiment the resultant potential energy surface for one of these states may be increased in accuracy. Some of finer details of excited-state electronic structure can be resolved by a second-order perturbation correlation to the CI-single energy.

Caution needs to be exercised in applying this level of theory. It can be useful in calculating accurate excited-state energy differences at elucidating subtle features in the excited-state potential energy surface [12-15].



## II. Perturbational methods

**MP2.** Unlike the CI case, where for a long time there has been general agreement as to what treatment to use, until recently there were several different approaches to the use of perturbation theory. So far the theory has been completely general. In order to apply perturbation theory to the calculation of correlation energy, the unperturbed Hamiltonian operator must be selected. The most common choice is to take this as a sum over Fock operators, leading to *Møller-Plesset* perturbation theory. The sum of Fock operators counts the electron-electron repulsion twice. The operator associated with this difference is often referred to as the fluctuation potential. From a technical point of view, we note that the identification of the MP2 quadruples a disconnected products of doubles was not easy, requiring a fair amount of tedious algebra. Clearly, it would be convenient if the identification of connected and disconnected terms in the Møller-Plesset wave functions could be made directly, without having to go through extensive algebraic manipulations in each case [12 – 14, 16 - 20].

**CASPT2.** The method *Complete Active Space Second Order Perturbation Theory* (CASPT2) is based on perturbation theory, which has turned out to be accurate in a wide variety of applications, in particular in electronic spectroscopy. Its basic principles are simple. Starting from a CASSCF reference function the remaining correlation effects are estimated using second order perturbation theory. This is a well known and widely used approach in single configurational quantum chemistry and we have all reasons to believe that it should work even better when we extend the reference function to include the configurations with the largest coefficients. The CASPT2 method is size-extensive and the weight of the reference function will consequently depend on the number of electrons, which are correlated, ultimately approaching zero for an infinite number of correlated electrons. With the intruder states we shall mean states in the  $V_{SD}$  (SD: all singly and doubly excited CSF's with respect to the CAS reference) space that have a zeroth order energy, which is close to, or even below the reference energy. In ordinary MP2 such states rarely occur, since there is a large separation in energy between occupied and external molecular orbitals. However, in the CASPT2 method, this is not always the case. The diagonal elements of the Fock matrix are related to ionization energies (IP) for inactive orbitals and to electron affinities (EA) for external orbitals. For active orbitals one obtains an average between IP and EA. Weakly occupied orbitals may thus have energies close to those of external orbitals and strongly occupied orbitals close to inactive orbitals. Since active orbitals may both excited out from and

into, it may happen that the energy denominators become small. If this happens we say that there is an intruder state in the  $V_{SD}$  space. The corresponding first order coefficient may then become large and a treatment based on perturbation theory is no longer valid. There are now several different implementations of MP2 type expansions based on CASSCF reference, denoted CASPT2. Experience of its performance is still somewhat limited. The CASPT2 method can be applied to any problem in electron structure theory. The great advantage of the approach is its general validity. It can be applied to any type of ground or excited state, independently of the complexity of the electronic structure. For this reason, multiconfigurational perturbation theory has been particularly useful in studies of excited states and transition metal complexes, where open shells and near degeneracies are common. Especially *Multistate CASPT2* performs that read number of root states, and a list of which CI vector from the CASSCF calculation to use for each state. A level shift technique is suggested for removal of intruder states in CASPT2. The first-order wavefunction is first calculated with a level shift parameter large enough to remove the intruder states. The effect of the level shift on the second-order energy is removed by a back correction technique [12 – 14, 21 – 24].

### III. Cluster expansion methods

**CCSD.** The idea of *Coupled Cluster (CC)* methods is to include all corrections of a given type to infinite order. The first term of CC wave function generates the reference HF and the second all singly excited states. The first parenthesis generates all doubly excited states, which may be considered as connected or disconnected. The second parenthesis generates all triply excited states which again may be either true or product triples. The quadruply excited states can similarly be viewed as composed of five terms, a true quadruple and four product terms. The coupled-cluster method represents the most successful approach to accurate many-electron molecular wave functions. It can be applied to relatively large systems and is capable of recovering a large part of correlation energy. It is size-extensive and presents few if any problems with respect to optimization. It does, however, require the existence of reasonably accurate single-determinant wave function and cannot – at least in its more common formulation – be applied to systems with degenerate or nearly degenerate electronic configurations. In practice, therefore, the application of the coupled-cluster method is restricted to systems that are dominated by a single electronic configuration and the coupled-cluster wave function is best regarded as providing an accurate correction to the Hartree-Fock description [12-14, 25-28].

## IV. Density Functional Theory

**DFT.** The basis for *Density Functional Theory* is the proof by Hohenberg and Kohn that the ground-state electronic energy is determined completely by the electron density  $\rho$ . In other words, there exists a one to one correspondence between the electron density of a system and the energy. The significance of this is perhaps best illustrated by comparing to the wave function approach. A wave function for an  $N$ -electron system contains  $3N$  coordinates, three for each electron (four if spin is included). The electron density is the square of the wave function, integrated  $N-1$  electron coordinates, this only depends on three coordinates, independently of the number of electrons. While the complexity of a wave function increases with the number of electron, the electron density has the same number of variables, independently of the system size. The only problem is that although it has been proven that each different density yields a different ground-state energy, the functional connecting these two quantities is not known. The goal of DFT methods is design functionals connecting the electron density with the energy [12 - 14, 29 - 31].

**TD-DFT.** Since Kohn-Sham DFT yields the exact charge density, in the limit of the exact exchange-correlation functional, properties (such as polarizabilities) which depend only on the response of the charge density to a static, local, applied field are in principle obtained exactly in Kohn-Sham DFT. In practice, good results have been obtained in the local density approximation (LDA) for static dipole polarizabilities and hyperpolarizabilities of molecules using either the finite field method or the coupled Kohn-Sham (KS) method which has been implemented by Colwell, Murray, Handy, and Amos. However these approaches are limited to the treatment of static electric fields. The formalism of time-dependent DFT generalizes Kohn-Sham theory to include the case of a time-dependent, local external potential. A practical computational formulation of time-dependent DFT can be developed using time-dependent response theory. This approach has been used successfully both for atoms and for solids. However, the algorithms involved make essential use of the symmetries inherent to the type of system considered, and thus are not suitable for molecular applications [12 - 14, 32 - 34].

## IV. Semi empirical methods

The cost of performing Hartree-Fock calculation scales formally as the fourth power of

the number of basis functions. This arises from the number of two electron integrals necessary for constructing the Fock matrix. Semi empirical methods reduce the computational cost by reducing the number of these integrals. Although linear scaling methods can reduce the scaling of *ab initio* Hartree-Fock methods, this is only the limiting behavior in the large basis set limit, and *ab initio* methods will still require a significantly larger computational effort than semi empirical methods. The first step in reducing the computational problem is to consider only the valence electrons explicitly, the core electrons are accounted for by reducing the nuclear charge or introducing functions to model the combined repulsion due to the nuclei and core electrons. Furthermore, only a minimum basis set is used for the valence electrons. The large majority of semi empirical methods to date use only s- and p- functions, and the basis functions are taken to be Slater type orbitals, i.e. exponential functions. Within the framework of Hartree-Fock calculations, some pieces of information (such as two-electron integrals) are sometimes approximated or completely omitted. In order to correct for this loss, Semi empirical methods are parametrized, that is their results are fit by a set of parameters in such a way, as to produce results the best agree with experimental data. Semi empirical calculations are much faster than their *ab initio* counterparts. Their results, however, can be very wrong if the molecule being computed is not similar enough to the molecules in the database used to parametrize the method. Semi empirical calculations have been very successful in the description of organic chemistry, where only a few elements are used extensively and molecules are of moderate size. Semi empirical methods also exist for the calculation of electronically excited states of polyenes. These methods can provide good estimates of the electronic excited states, when parameterized well. In contrast to their Hartree-Fock-based semi-empirical counterparts (i.e: MOPAC [35]), the pi-electron theories have a very strong *ab initio* basis [12].

**MNDO.** The *Modified Neglect of Diatomic Overlap* (MNDO) has been parameterized for the elements: H, B, C, N, O, F, Al, Si, P, S, Cl, Zn, Ge, Br, Sn, I, Hg and Pb. Although MNDO has been succeeded by the AM1 and PM3 methods, it is still used for some types of calculation where MNDO is known to give better results.

Some known limitations of MNDO model are,

- Sterically crowded molecules, like neopentane, are too unstable.
- Four membered rings are too stable.
- Weak interactions are unreliable, for example it does not predict hydrogen bonds.
- Hypervalent molecules, like sulfoxides and sulfones, are too unstable.
- Activation energies for bond breaking/forming reactions are too high.
- Non-classical structures are predicted to be unstable relative to classical structures.

- Oxygenated substituents on aromatic rings out-of-plane.
- Peroxide bonds are too short.
- The C-X-C angle in ethers and sulfides is too large.

**AM1.** After some experience with MNDO, it became clear that there were certain systematic errors. For example the repulsion between two atoms which are 2-3 Å apart is too high. This has as a consequence that activation energies in general are too large. The source was traced to too repulsive interaction in the core-core potential. To remedy this, the core-core function was modified by adding Gaussian functions, and the whole model was reparameterized. The result was called *Austin Model 1* (AM1) in honour of Dewar's move to the University of Austin. AM1 was developed by Michael Dewar and co-workers, and published in 1985, as an attempt to improve the MNDO model by reducing the repulsion of atoms at close separation distances. AM1 has been parameterized for the elements: H, B, C, N, O, F, Al, Si, P, S, Cl, Zn, Ge, Br, I and Hg. Some known limitations of AM1 model are,

- AM1 does predict hydrogen bonds with strength approximately correct, but the geometry is often wrong.
- Activation energies are much improved over MNDO.
- Hypervalent molecules are improved over MNDO, but still have significantly larger errors than other types of compound.
- Alkyl groups are systematically too stable by ~ 2 kcal/mol per CH<sub>2</sub> group.
- Nitro compounds are systematically too short by ~ 0.17 Å.
- Phosphorus compounds have problems when atoms are ~ 3 Å apart, producing incorrect geometries.
- The *gauche* conformation in ethanol is predicted to be more stable than the *trans*.

**PM3.** The parameterization of MNDO and AM1 had been done essentially by hand. Since the optimization was done by hand, only relatively few reference compounds could be included. Stewart made the optimization process automatic, by deriving and implementing formulas for the derivative of suitable error function with respect to the parameters. All parameters could then be optimized simultaneously, including the two-electron terms, and significantly larger training set with several hundred data could be employed. In this reparameterization, the AM1 expression for the core-core repulsion was kept, except that only 2 Gaussians were assigned to each atom. These Gaussian parameters were included as an integral part of the model, and allowed to vary freely. The resulting method is *Modified Neglect of Diatomic Overlap*, quote-unquote *Parametric Method Number 3* (MNDO-PM3, PM3 for short), and is essentially AM1

with all the parameters fully optimized. In a sense it has the best set of the parameters for the given set of experimental data. The optimization process, however, still requires some human intervention, in selecting the experimental data and assigning appropriate weight factors to each set of data. PM3 has been parameterized for the elements: H, Li, C, N, O, F, Mg, Al, Si, P, S, Cl, Zn, Ga, As, Se, Br, Cd, In, Sn, Sb, Te, I, Hg, Tl, Pb, Bi, Po and At. Parameters for many of the transition metals are also developed under the name PM3, which includes d-orbitals.

Some known limitations of AM1 model are,

- Almost all  $sp^3$ - nitrogens are predicted to be pyramidal, contrary to experimental observation.
- Hydrogen bonds are too short by  $\sim 0.1 \text{ \AA}$ .
- The *gauche* conformation in ethanol is predicted to be more stable than *trans*.
- Bonds between Si and Cl, Br and I are underestimated, the Si-I bond in  $H_3SiI$ , for example, is too short by  $\sim 0.4 \text{ \AA}$ .
- $H_2NNH_2$  is predicted to have a  $C_{2h}$  structure, while the experimental is  $C_2$ , and  $ClF_3$  is predicted to have a  $D_{3h}$  structure, while the experimental is  $C_{2v}$ .
- The charges on nitrogen atoms is often “incorrect” sign and “unrealistic” magnitude.

Some common limitation to MNDO, AM1 and PM3 are :

- Rotational barriers for bonds which have partly double bond character are significantly too low. This is especially a problem for the rotation around the C-N bond in amides, where values 5 – 10 kcal/mol are obtained. A purely *ad hoc* fix has been made for amides by adding a force field rotational term to the C-N bond which raises the value 20-25 kcal/mol, brings it in line with experimental data. Similarly, the barrier for rotation around the central bond in butadiene is calculated to be only 0.5 -2.0 kcal/mol, in contrast to the experimental value of 5.9 kcal/mol.
- Weak interactions, such as in a van der Waals complexes or hydrogen bonds, are poorly predicted. Either the interaction is too weak, or the minimum energy geometry is wrong.
- The bond length to nitrosyl groups is underestimated, the N-N bond in  $N_2O_3$ , for example, is  $\sim 0.7 \text{ \AA}$  too short.
- Although MNDO, AM1, and PM3 have parameters for some metals, these are often based on only a few experimental data. Calculations involving metals should thus be treated with care. The PM3 set of parameters are determined exclusively from geometrical data (X-ray), since there are very few reliable energetic data available for transition metal compounds.

Semi-empirical methods are zero-dimensional, just as force field methods are. There

is no way of assessing the reliability of given result within the method. This is due to the selection of a fixed basis set. The only way of judging results is by comparing the accuracy of other calculations on similar systems with experimental data. Semi empirical models provide a method for a calculating electronic wave function, which may be used for predicting a variety of properties. There is nothing to hinder the calculation of say the polarizability of a molecule where the second derivative of the energy with respect to an external electric field, although it is known from *ab initio* calculations that good results require a large polarized basis set including diffuse functions, and inclusion of electron correlation. Semi empirical methods like AM1 or PM3 have only a minimum basis which is lacked polarization and diffuse functions, electron correlation is only included implicitly by the parameters, and no polarizability data have been used for deriving the parameters. Whether such calculations can produce reasonable results, as compared to experimental data, is questionable, and they certainly require careful calibration.

**Hückel.** The *Hückel* methods perform the parameterization on the Fock matrix elements. The Hückel methods are non-iterative, they only require a single diagonalization of the Fock (Hückel) matrix. The approximation of this model are taken to the limit. The Hückel method is essentially only used for educational purposes or for very qualitative orbital considerations. It has the ability to produce qualitatively correct MOs, involving a computational effort which is within reach of doing by hand.

**ONIOM.** The *Our Own N-Layered Integrated Molecular Orbital + Molecular Mechanics* (ONIOM) method have been proven to be powerful tools for the theoretical treatment of large molecular systems where different levels of theory are applied different parts of a molecule. The ONIOM method is a generalized hybrid scheme to treat different parts of a molecular systems at different level of theory. Its implementation in the *Gaussian03* program system allows the definition of up to three arbitrarily shaped layers with the free choice of the method. In the two-layered ONIOM method, the total energy of the system is obtained from three independent calculations:  $E_{\text{model}}^{\text{high}}$ ,  $E_{\text{real}}^{\text{low}}$  and  $-E_{\text{model}}^{\text{high}}$  make  $E^{\text{ONIOM2}}$ . Real denotes the full system, which is treated at the low level, while model denotes the part of the system of which the energy is calculated at both the high and low level. Although ONIOM can in principle be used for any number of layers, for which  $2N-1$  subcalculations are required. The definition of the model system is rather straightforward when there is no covalent bond between the layers. The ONIOM method can combine different levels of MO methods into a single integrated calculation of the energy or other electronic properties, a unique feature not available in other hybrid methods. The method elegantly takes into account both electronic and steric effects of the environment or substituents on the energy, geometry, and other properties of interest, and can be applied to excited states, as well as the ground state [36 - 42].

**PCM.** The *polarizable continuum model* (PCM) has been widely used since its appearance for the study of many chemical processes. The most recent versions of PCM allow the *ab initio* calculation of the energy and the energy properties of molecules dissolved in anisotropic and inhomogeneous solvents, the analytic optimization of solutes geometry and the calculation of static and frequency dependent polarizabilities and hyperpolarizabilities in solution. The choice of the solute cavity is the most delicate steps in defining a continuum solvation model. It has been recognized that the best results are obtained with realistic shapes, mimicking the actual solute molecule. In the majority of models such a cavity is built with interlocking spheres, usually centered on atoms or on atomic groups: this leaves the problem of choosing suitable atomic or group radii. Many possible choices for the atomic radii have been proposed: the most refined treatments link the dimensions of each portion of the cavity to the actual electronic charge inside, or found optimized radii, calibrated on the solvation energies of a representative set of solutes. The charge dependent radii can cause some problems when studying chemical reactions, and the optimized radii refer to a particular salvation method, and tend to obscure the actual differences with other approaches: moreover, there is always the risk that the optimization depends on



the basis set and the level of calculation [13, 43 - 46].

# Chapter 1

Large aromatic hydrocarbon networks



**E**ffect of a single nitrogen atom substitution to a number of large polycyclic aromatic hydrocarbon (PAH) molecules was calculated systematically, by Hückel molecular orbital theory, and abnormal electron transfer (called tunnelling electron transfer, TET) was observed especially in parallelogram-type PAH (see Fig.1.1) [69].

That is, fairly large amount of  $\pi$ -electron is withdrawn to an electronegative nitrogen atom from almost the farthest end of a conjugated aromatic hydrocarbon molecule, leaving almost no change in the interior of the molecule [48 - 51]. This change can be simulated by the Kekule structure counting for subgraphs of the parent molecule. To verify the TET semi-empirical, *ab initio*, and DFT calculations were carried out.

This 2-dimensional system of graphite sheet was extended to a 3-dimensional system of carbon nanotubes.

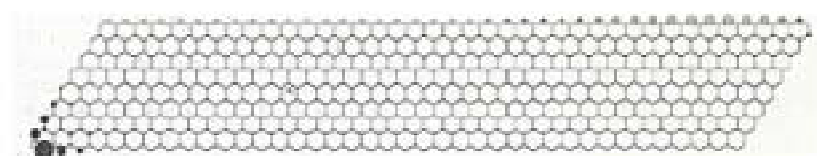


Fig.1.1 Tunnelling electron transfer is shown in parallelogram-type PAH. It was calculated by HMO method. The largest filled circle indicates the position of nitrogen atom substitution [69].

The nanotubes consist solely of carbon,  $sp^2$ -bonded as in graphene strips rolled to form closed cylinders. The structure of the nanotubes has been studied using high-resolution transmission electron microscopy. Iron group catalysts, such as Co, Fe, and Ni, produce single-layer nanotubes with diameters typically between 1 and 2 nm and lengths on the order of micrometers.

The catalyzed growth of nanotubes by chemical vapor deposition which proposes that their formation and growth is an extension of other known processes in which graphitic structures form over metal surfaces at moderate temperatures through the decomposition of organic precursors. Importantly, the model also states that the form of carbon produced depends on the physical dimensions of the catalyzed reactions.

The synthesis of molecular carbon structures which was reported Sumio Iijima the preparation of a new type of finite carbon structure consisting of needle like tubes [1]. To produce by an arc-discharge evaporation method similar to the fullerene synthesis, the needles grow at the negative end of the electrode used for the arc discharge. In addition to initially developed laser-furnace and arc-discharge techniques, catalytic chemical vapor deposition (CCVD) method [55 - 58] has been contrived for a scalable, large-scale production of SWNTs, with various carbon-source molecules tested such as carbon monoxide, methane, or ethanol. It was analyzed with Raman spectrometry, scanning electron microscopy (SEM) and transmission electron microscopy (TEM)(See Fig.1.2).

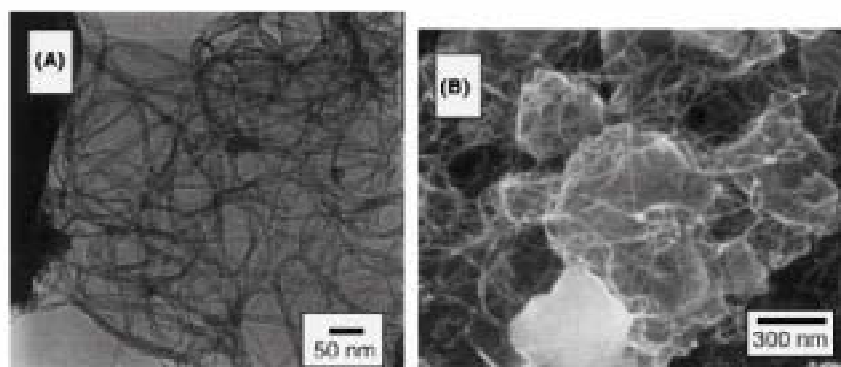


Fig. 1.2. Lower magnification TEM image (panel A) and SEM image (panel B) of 'as grown' SWNTs. By catalytic decomposition of ethanol is over a Fe/Co mixture embedded in zeolite at 800 °C. Dark parts in the left of panel A is zeolite surface. Both in panels A and B, web-like growth of bundles of SWNTs covering zeolite particles around 300 nm were observed, nothing else[62].

Carbon nanotubes are unique tubular structures of nanometer diameter and large length/diameter ratio which depends on the wrapping graphene. The various types of carbon family are shown in Fig.1.3.

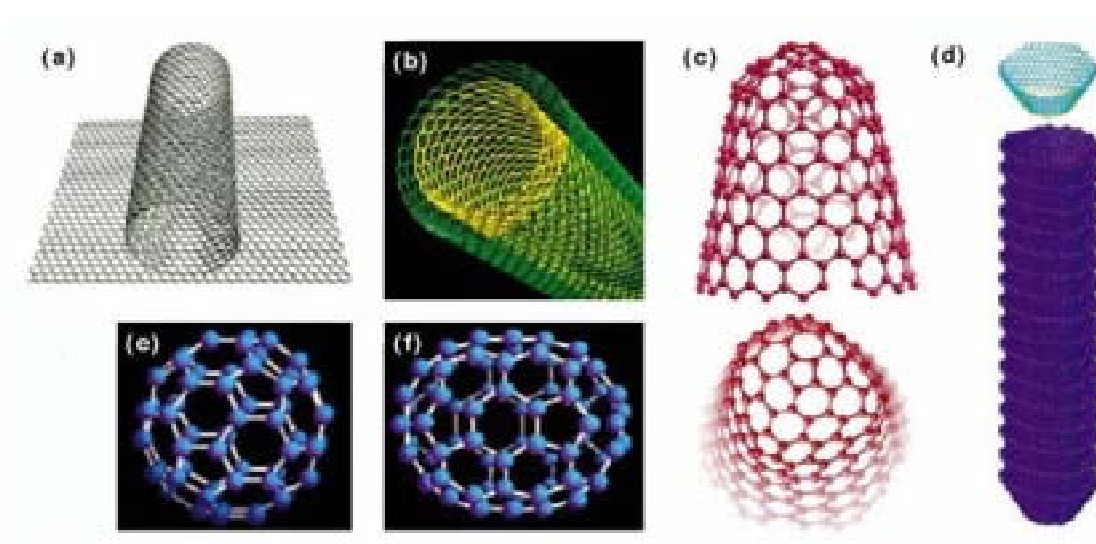


Fig. 1.3 The various types of carbon family.

(a) Single-walled carbon nanotubes (b) Multi-walled carbon nanotube (c) Carbon nanohorn  
(d) The cupstack type of carbon nanotube (e) Fullerene  $C_{60}$  (f) Fullerene  $C_{70}$

Experimentally, a catalytic metal atom sticking on an open edge of a growing SWNT was supposed to prevent the formation of a closure with pentagons by scooting around the edge[50, 51]. Yudasaka *et al.*[59] examined several catalytic metal species and their alloys in their laser-furnace experiments and discussed in detail the effect of the choice of catalyst based on their phase diagrams. They suggested a 'metal-particle model', in which droplets of carbon-containing catalytic metal were formed as a consequence of laser ablation and in the subsequent cooling stage the carbon atoms were separated out from the metal nuclei to form SWNTs. Furthermore, Kataura *et al.*[60] proposed 'fullerene-cap model', where fullerene-like carbon clusters formed during laser-ablation attach to metal particles that served as nuclei for SWNT growth; this model was based on the experimental observation that the growth conditions of fullerene and SWNT were similar and that the diameter distribution of SWNTs was correlated with that of fullerenes [64-68].

Chemical and physical routes under conditions of moderate temperatures and pressures are generally used to synthesize nanocrystals and nanostructures with metastable phases. The size effect of nanocrystals and nanostructures may be responsible for the formation of these metastable phases at the nanometer size. To date, there has not been a clear and detailed understanding of the effects causing the

formation of the metastable structures from the viewpoint of thermodynamics.

There is no a clear insight into which chemical and physical origins leading to the growth of the carbon nanotube.

## 1.1 Graphene

Much attention has been directed to electron transfer in large conjugated  $n$ -electron systems by quantum chemistry methods. The effect of a single nitrogen atom substitution to large polycyclic aromatic hydrocarbon (PAH) molecule was calculated. However the molecular mechanism is still not clear at the high level methods of quantum chemistry. Using the perturbation technique developed by Coulson and Longuet-Higgins which is simulated by the Kekulé structure counting for subgraphs of PAH, Hosoya et al. found anomalous but interesting behavior of the  $n$ -electron flow called tunneling electron transfer, TET, in parallelogram-type PAHs. This abnormal electron transfer cannot be predicted by the conventional organic electron theory. According to the HMO calculations by Hosoya *et al*, TET was observed in PAHs having a singly-substituted nitrogen atom [69].

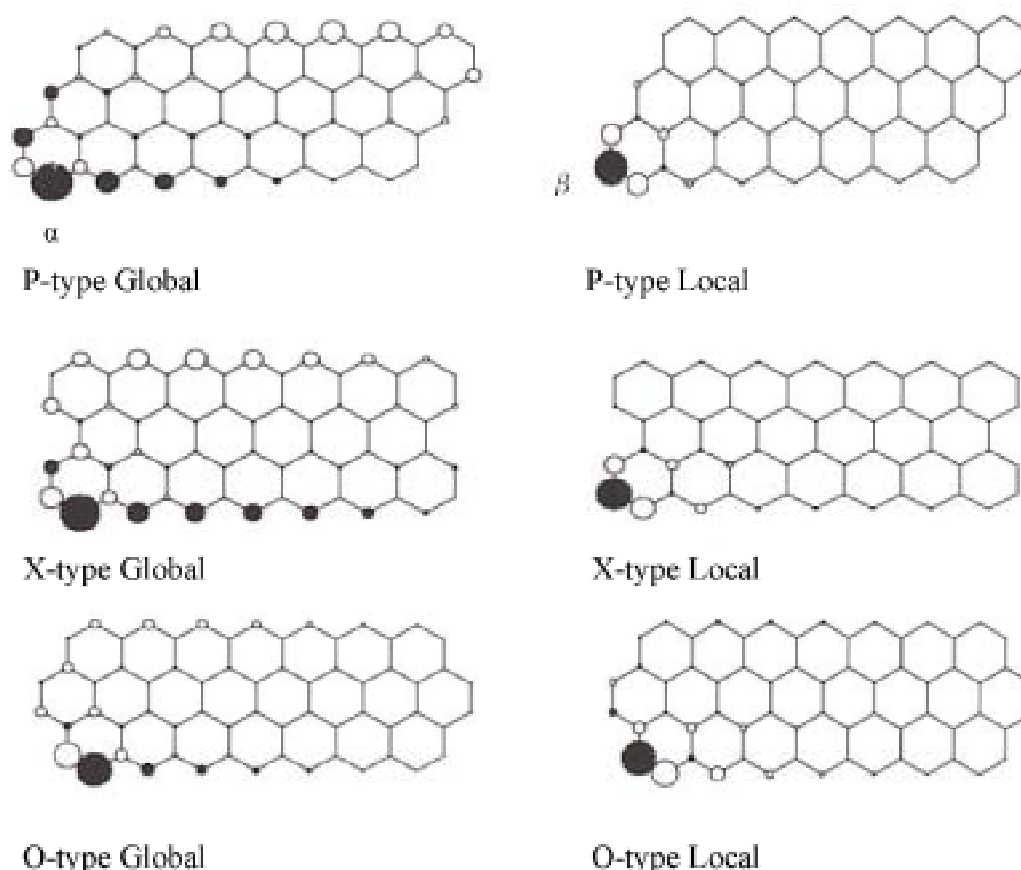


Fig.1.3 Global tunnelling electron transfer, TET, (see the left side), and local electron transfer (see the right side) obtained by Hückel molecular orbital theory. The largest filled circle indicates the position of nitrogen atom substitution [69].

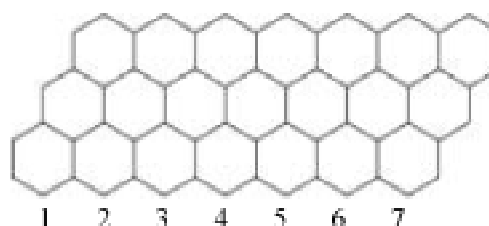


Let us call parallelogram-type PAHs as P-type, X-type, and O-type, respectively and name the mode of electron withdrawal from the peripheral carbon atoms by substituting an electronegative nitrogen atom at  $\alpha$ - and  $\beta$ -positions as Global and Local (see Fig. 1.3). The Global TET was observed; negatively charged peripheral atoms were situated on the left and lower edges and while the atoms on the right and upper edges are positively charged. The name of local corresponds to the local effect of the electron transfer (see the right side of Fig. 1.3).

Substitution of a single nitrogen atom at one of the edge carbons of this PAH network, the  $n$ -electrons are perturbed those on the peripheral carbon atoms. This substitution causes a big tide of electron wave comes from the opposite but not the farthest end of the network. We have analyzed in detail this electron transfer along the same shore at the epicenter indicating that a fairly large amount of excess  $n$ -electron is accumulated.

In this study we carried out more elaborated semi-empirical and ab initio molecular orbital (MO) and DFT calculations to elucidate whether its phenomena are observed at the higher level of theory.

Fig. 1.4 The numbering of carbon edges  
(Parent type)



### 1.1.1 Computational Details

Molecular orbital calculations were carried out for P-type, X-type, and O-type PAHs using AM1, PM3, and MNDO MO methods which are semi-empirical methods for the quantum calculation of molecular electronic structure. All C-C distances were set to 1.39 Å to compare the same PAH.

Geometry optimizations using a hybrid method, ONIOM(MP2/AM1), and DFT with a B3LYP functional for P-type PAHs were also performed to investigate the effect of the nitrogen substitution. The systems studied are benzene networks which are arranged 3 benzenes vertically and 7 benzenes horizontally to investigate the abnormal phenomena TET. This is the smallest one, in which TET was observed at the Hückel MO level.

### 1.1.2 Electron Charge Transfer

By applying of the semiempirical and *ab initio* MO methods to the TET phenomena, we observed the  $\delta+$  charges in the Global PAH at the more precise level of calculations than Hückel method. Using the semiempirical method there are a lot of charges in the Global PAH. In this level the large  $\delta+$  charges appear in the opposite shore from the substituted site, especially, on the left side from the center of the opposite shore. From the *ab initio* level calculations we found that the  $\delta+$  charges were shown up in the left side surface of this molecule and they spread out the opposite sites in the Global PAH. In comparison with Hückel method, the distribution of  $\delta+$  charges by *ab initio* MO calculations for the Global PAH are more similar than that by semiempirical method. Furthermore,  $\delta+$  charges based on semi empirical methods are relative to those of *ab initio* MO calculations. In consequence the TET phenomena are observed by Hückel, semiempirical MO, and *ab initio* MO methods.

When the substitution site from carbon to nitrogen are altered to the next left site, at the  $\beta$  site instead of the  $\alpha$  site, i.e., for Local PAH, the effect of its alteration is not so dramatic by Hückel, semiempirical MO, and *ab initio* MO methods. The different  $\delta+$  charges depend on the integration algorithm at the each level of the calculations.

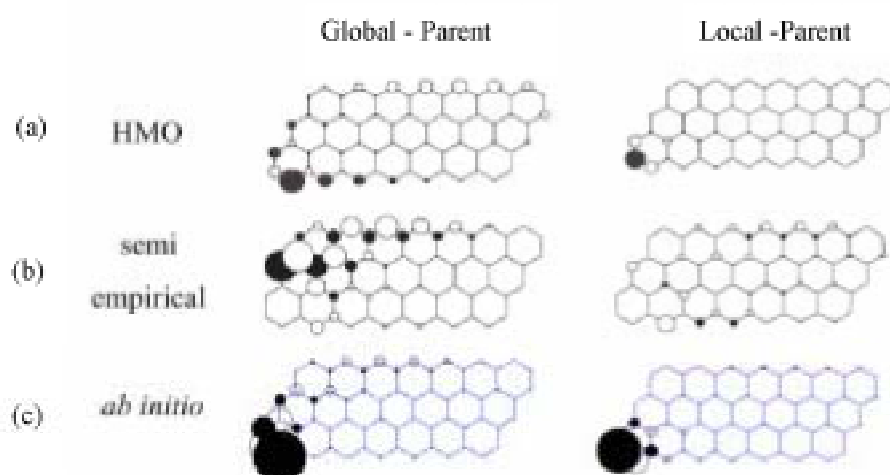


Fig. 1.5 The white and black circles show  $\delta+$  and  $\delta-$  charges, respectively. The scale of the circles is different in the level of calculations. The  $\delta+$  charges behavior was shown of Global and Local at Hückel method, semiempirical method, and *ab initio*. Lower left benzene value is omitted in semi-empirical method.

Taking into the consideration for the methodological difference we estimated the  $\pi$  and  $\sigma$  charges at semiempirical method, and *ab initio* for comparison with these methods and Hückel method. To distinguish the  $\pi$  from  $\sigma$  charges, we consider the difference between Global and Parent or Local and Parent as those charges.

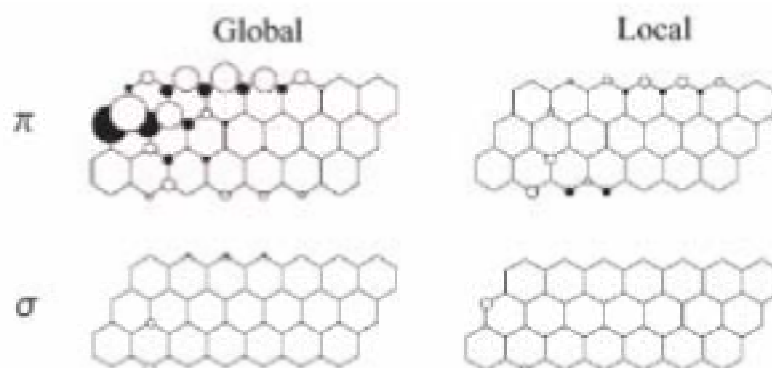


Fig. 1.6  $\pi$  and  $\sigma$  electron transfer distribution at semi empirical level.

The  $\pi$  and  $\sigma$  electron transfer have been shown in Fig. 1.6. The differences between Global and Local phenomena were also observed at the  $\pi$  and  $\sigma$ . Consequently  $\pi$  electron transfer distribution decides total electron transfer comparing with  $\pi$  and total electron transfer.

Figures 1.7(a), (b), and (c) show the difference of charge values between Global and Parent (See Fig.1.4.) and between Local and Parent for AM1, PM3, and MNDO calculations, respectively. By using AM1, PM3, and MNDO a big difference between Global and Parent of Mulliken charge value was observed in the opposite shore to the position of substituted nitrogen. It is interesting to note that every type also had a same tendency of TET phenomena. The Global TET is observed; negatively charged peripheral atoms were situated on the left and lower edges and while the atoms on the opposite edges are positively charged. It appears from the 3 and 7 carbon atoms put perpendicularly and horizontally, respectively. This substitution causes a big tide of electron wave comes from the opposite but not the farthest end of the network. We have analyzed in detail this electron transfer along the same shore at the epicenter indicating that a fairly large amount of excess  $n$ -electron is accumulated. The strength of TET behavior depends on the periphery structure. In this report the P, X, O-type have been shown that the molecules are arranged 3 benzens vertically and 7 benzenes horizontally in Fig. 1.7.

The TET phenomena in Global PAH appears on the left side from the center carbon sites at the external 7 carbon sites in view of the substitution carbon site by the AM1, PM3, and MNDO level calculations. Compared the Global and Local at each structure the electron transfer is not so remarkable for Local.

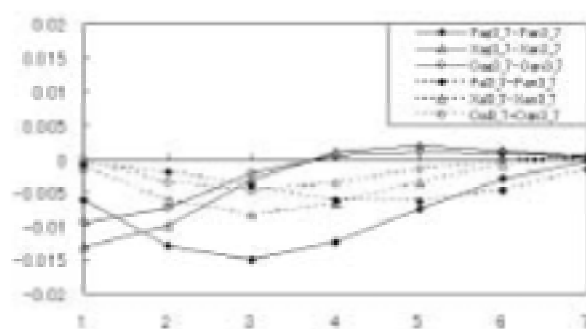


Fig. 1.7(a) Calculated by AM1.

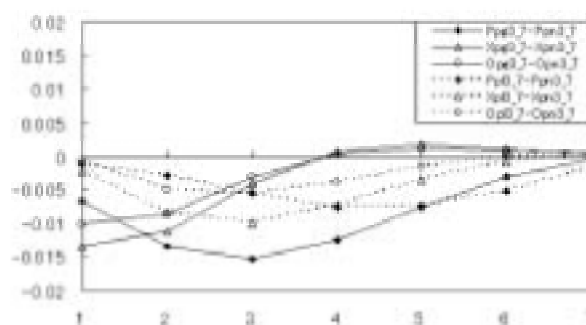


Fig. 1.7(b) Calculated by PM3.

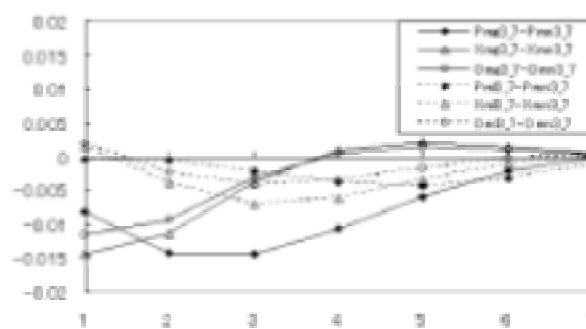


Fig. 1.7(c) Calculated by MNDO.

Fig. 1.6 The difference of Mulliken charges which were placed at the edge of carbons between Parent and others for the P-type, X-type, and O-type PAHs. See Fig. 1.4 for the numbering of carbon atoms at the edge.

### 1.1.3 MP2/AM1 and DFT

The Mulliken charges at MP2/AM1 level in Global PAH show on the left side from the center carbon sites at the external 7 carbon sites in view of the substitution. The TET at Global PAH was observed on the left side of the 7 carbon sites in Fig. 1.8.

On the other hand, the TET is also found at the DFT level. Mulliken charges which simply takes each two-center term of the density and wavefunction, divides by two and places 1/2 on each constituent atom. In this case the basis set made more complex since 6-31G\* was used for MP2/AM1 and DFT methods.

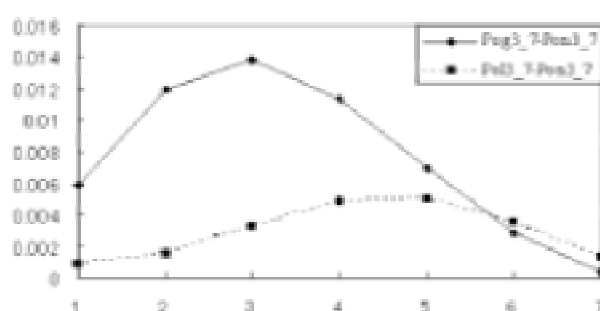


Fig. 1.8 (a) Mulliken charges at the edge of P-type by QM/QM (MP2/AM1). See Fig. 1.4 for the numbering of carbon atoms at the edge.

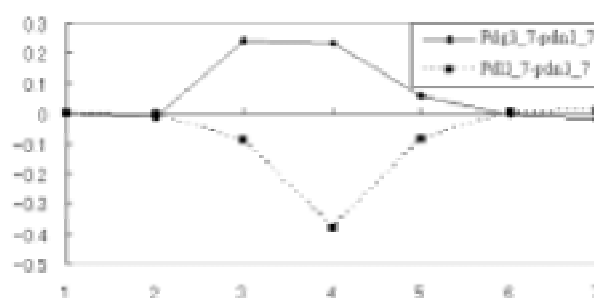


Fig. 1.8 (b) Mulliken charges at the edge of P-type by DFT. See Fig. 1.4 for the numbering of carbon atoms at the edge.

## 1.2 Carbon Nanotubes

Carbon nanotubes are composed entirely of  $sp^2$  carbon atoms, similar to graphite. The  $sp^2$  carbon atoms found in diamond, this carbon-carbon double bond strong structure provides them with their unique strength. Nanotubes naturally align themselves into "ropes" held together by van der Waals forces. Under high pressure, nanotubes can merge together, trading some  $sp^2$  carbon atoms for  $sp^3$  bonds, giving great possibility for producing strong, unlimited-length wires through high-pressure nanotube linking.

Most SWNTs have a diameter about 1nm, with a tube length that many thousands of times larger. The structure of a SWNT can be conceptualized by wrapping a one-atom-thick layer of graphite (called graphene) into a seamless cylinder. The way of the wrapping is represented by a pair of indices  $(n, m)$  called the chiral vector. The integers  $n$  and  $m$  denote the number of unit vectors along two directions in the honeycomb lattice of graphene. If  $m=0$ , the nanotubes are called "zigzag". If  $n=m$ , the nanotubes are called "armchair". Otherwise, they are called "chiral"(see Fig. 1.9).

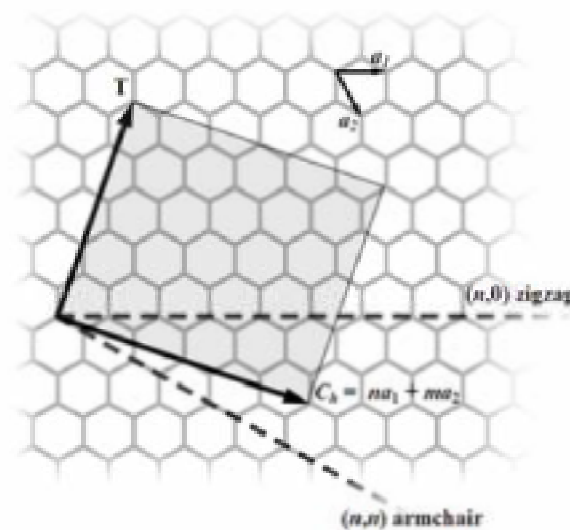


Fig. 1.9. The  $(n,m)$  nanotube naming scheme can be thought of as a vector ( $Ch$ ) in an infinite graphene sheet that describes how to 'roll up' to graphene sheet to make the nanotube.  $T$  denotes the tube axis, and  $a_1$  and  $a_2$  are the unit vectors of graphene in real space [70].

Carbon nanotubes display either metallic or semiconducting properties which depends on chiral. Due to the symmetry and unique electronic structure of graphene, the structure of a nanotube strongly affects its electrical properties. For a given (n,m) nanotube, if  $2n + m = 3q$  (where q is an integer), then the nanotube is metallic, otherwise the nanotube is a semiconductor. Thus all armchair ( $n=m$ ) nanotubes are metallic, and the other nanotubes are semiconducting. An alternative (equivalent) representation of this condition is if  $(n-m)/3 = \text{integer}$ , then the SWNT is metallic.

### 1.2.1 Computational Details

The structures of open-end carbon nanotubes have been optimized using the semi-empirical PM3 method. First we prepared a series of graphene sheets to make the SWNT having different chirality. When the graphene sheets are rolled up to make single layer carbon nanotubes, they have open-end structures, which are similar to pens, with valley-side and mountainside (see Fig. 1.11). The SWNT has 12 carbon atoms at the open-end, while the diameter depends on its chirality. Carbon atoms at the open-end were replaced with an electronegative nitrogen atom one by one. The substituted sites were denoted as a, b, c, d, e, f, g, h, i, j, k, and l as shown in Fig. 1.10.

In this case the length in a direction perpendicular to its diameter of the nanobube with any chirality will keep the property of carbon nanotubes according to the study by Araragi *et al.* [E. Araragi and K. Takano, private communication.].

MOPAC program package was used for the PM3 calculations in this cahpter.

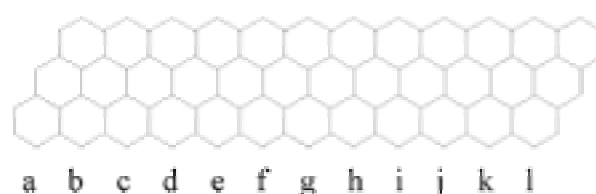


Fig. 1.10 The alphabetical sequence of the carbon site replaced with a nitrogen.

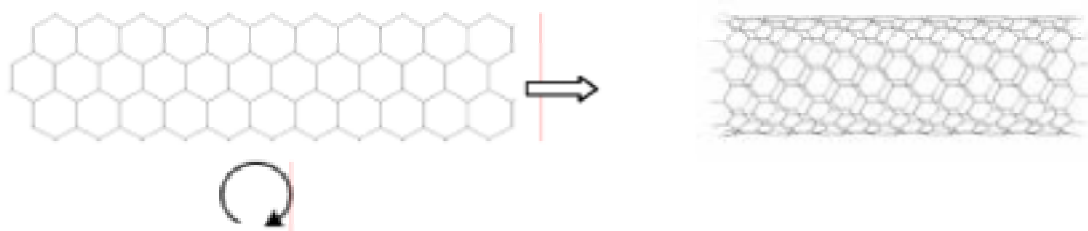


Fig. 1.10(a) (12,0) zigzag

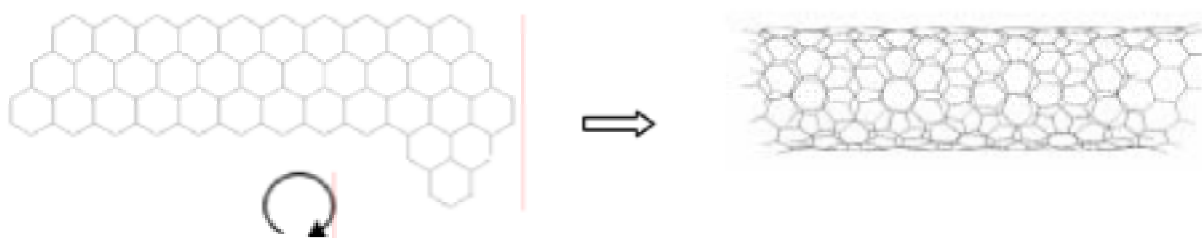


Fig. 1.10(b) (10, 2)

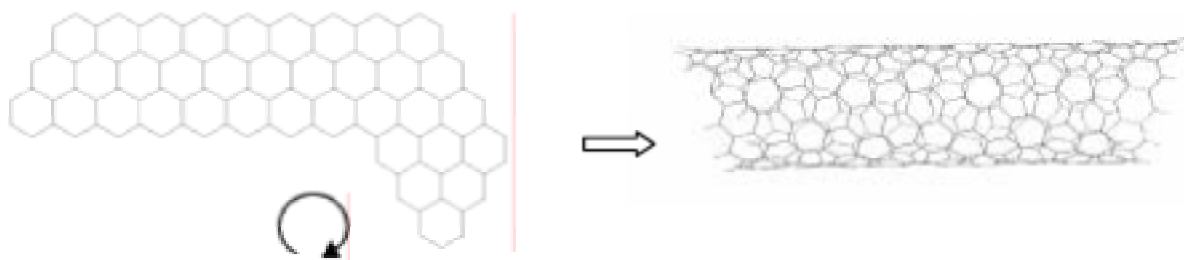


Fig. 1.10(c) (9, 3)

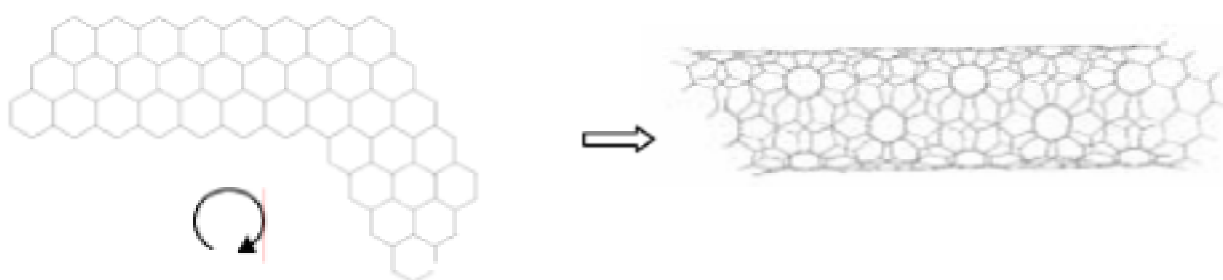


Fig. 1.10(d) (8, 4)

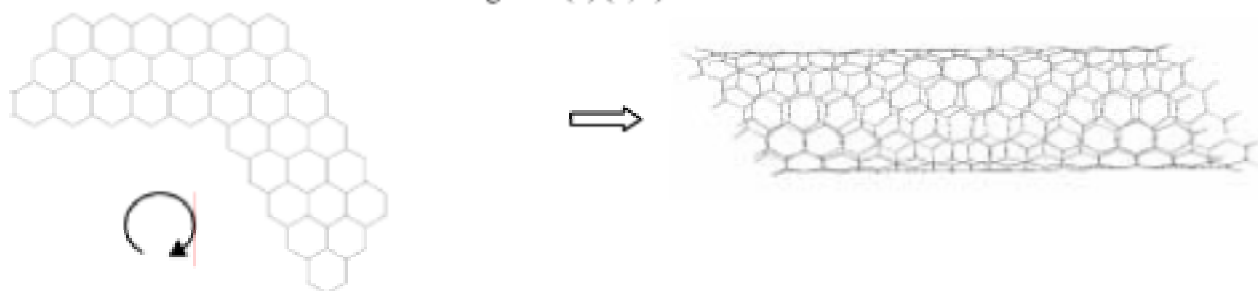


Fig. 1.10(e) (7, 5)

Fig. 1.11 The graphene sheet (left side) is rolled into SWNT (right side).



### 1.2.2 Heat of formation

The thermal properties play an important role in the growth of carbon nanotubes. Making carbon nanotubes involves the use of a carbon arc to heat graphite to about 5000 °C. They exhibit extraordinary strength and unique electrical properties, and are efficient conductors of heat. The syntheses for carbon nanotubes includes the high conductivity for interconnection and excellent thermal properties which are available for the function of temperature while carbon nanotubes are found to significantly enhance the thermal stability of polypropylene in nitrogen at high temperatures. Namely the modelling of the mechanical, thermal properties of nanotubes via numerical simulations forms the part of this section, concerned with the nano-scale mechanics and nano-scale thermodynamics of nanotubes.

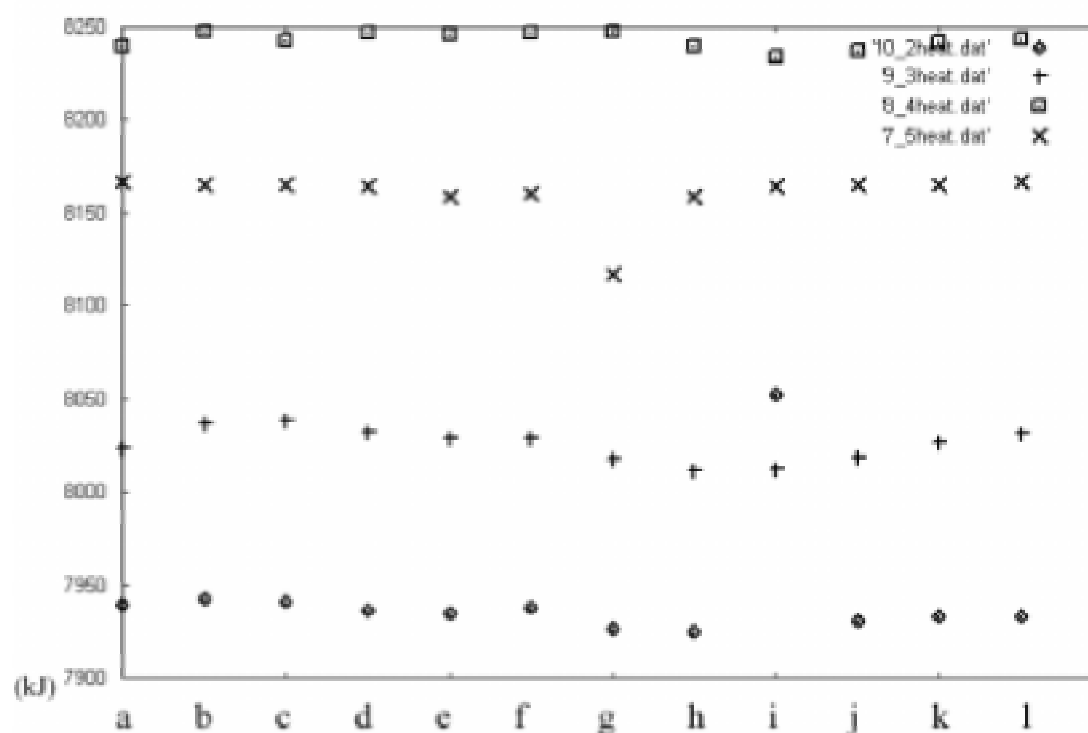


Fig. 1.11 Theoretical energy of heat formation. 'a' to 'l' have been shown the substitution sites from carbon to nitrogen at each nanotube.

Chemical formula of all the isomers of the substituted nanotubes studied in this work is  $C_{311}H_{23}N$ . The PM3 heat of formation of the substituted nanotubes is shown in Fig. 1.11. The chiral nanotube (10,2) was found to have the lowest heat of formation except for the case of the site "i" substitution. This suggests that the chiral nanotubes (10,2) are more stable than the other nanotubes with the other chirality if the synthesis controlled for the chirality is conducted.

### 1.2.3 Molecular orbitals and energies

A molecular orbital describes the behavior of one electron in the electric field generated by the nuclei and some average distribution of the other electrons. It shows the orbital interaction, bonding, and quantitative values for the molecular energy levels. The optimized geometry doesn't have kept the good symmetry of the open end nanotube but it is useful to be familiar with inorganic semiconductors to see the HOMO level. When the molecule forms a dimer or an aggregate, the proximity of the orbitals of the different molecules induce a splitting of the HOMO and LUMO energy levels. This splitting produces vibrational sublevels which each have their own energy, slightly different from one another. There are as many vibrational sublevels as there are molecules that interact together. It plays an important role to analyze the edge of the interaction between catalyst and vapor. It is helpful to search the possibility to extend the key of the carbon nanotube growth.

Table.1.2.1 Orbital energies of frontier orbitals and HOMO-LUMO gap values for the substituted nanotube  $C_{311}H_{23}N$  in eV.

	(7,5)a	(7,5)f	(9,3)a	(9,3)f	(9,3)d	(10,2)a	(10,2)f	(10,2)c	(12,0)a
LUMO	-4.6177	-4.5699	-4.2282	-4.2551	-4.2530	-4.2134	-4.2756	-4.2430	-4.1577
HOMO	-5.7149	-5.6872	-5.8305	-5.9042	-5.8423	-5.9344	-5.9470	-5.9718	-5.8423
HOMO-1	-6.5503	-6.7529	-6.4654	-6.4931	-6.4588	-6.1504	-6.1834	-6.0410	-6.4263
HOMO-LUMO gap	1.0972	1.1173	1.6023	1.6491	1.5893	1.7210	1.6714	1.7288	1.6840

Let us call the inside position of carbon atoms "Valley" denoted as site  $a$ , and the outside position "Mountain" denoted as site  $d$ , when the graphene sheet was wrapped. The  $f$  position is opposite to  $a$ .

As shown in Fig. 1.12, the HOMOs were delocalized one open side. This feature of the HOMOs indicates that nanotubes could grow easier on one side than the others, since the growth mechanism of carbon nanotube is described the interaction of attachment between basement and the seed of carbon nanotube. Namely, it seems that the interaction happens at one open-end effectively.

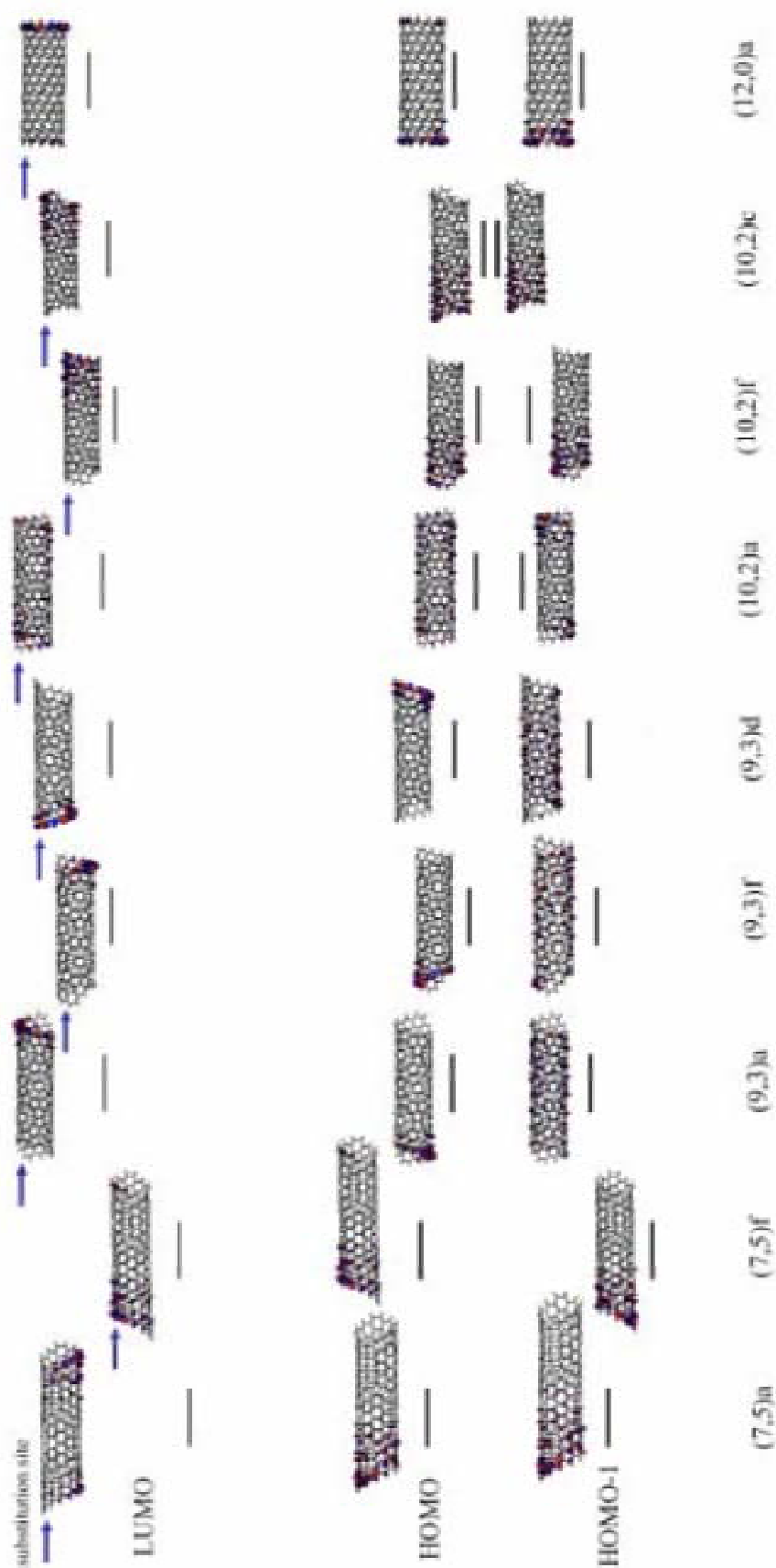


Fig. 1.12 The Eigen value and Molecular Orbitals on SWNTs.

### 1.2.4 Net Charges

Figure 1.13 shows the Mulliken net charges for the substituted nanotubes  $C_{311}H_{23}N$ . The charges spread out on the internal region for carbon nanotubes (9,3), while the chiral nanotubes (7,5) and (10,2), and zigzag nanotube (12,0) don't have such charge distribution. It is noteworthy that  $\delta^+$  charge appears on the opposite side against the substituted-nitrogen site for zigzag nanotube (12,0). This is similar to TET for the Global of the graphene sheet.

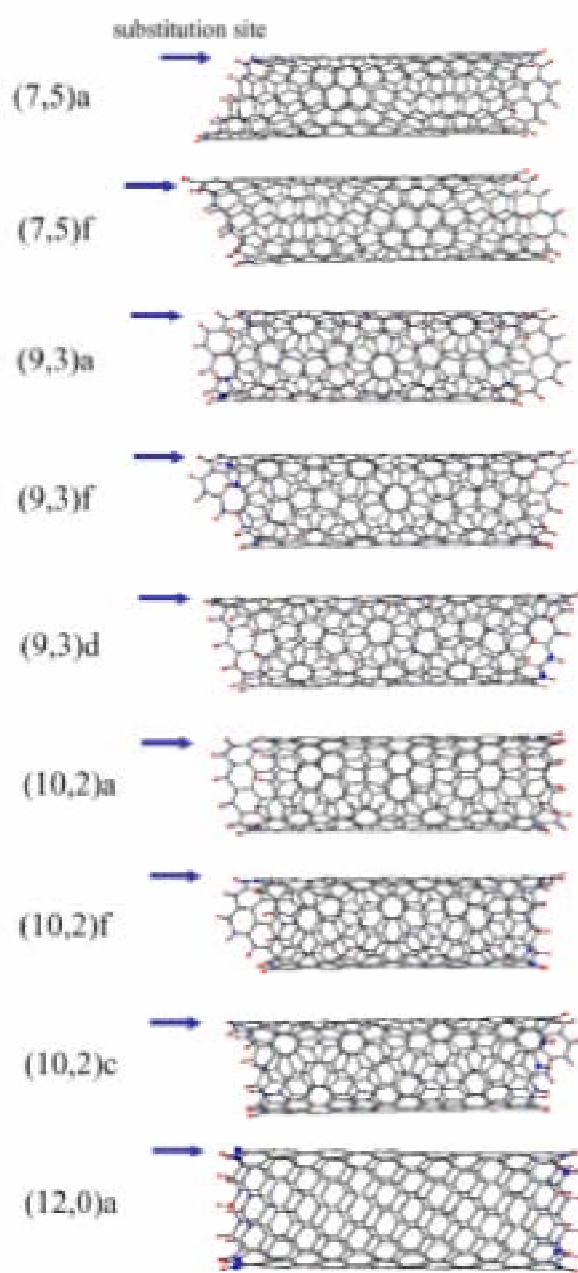


Fig. 1.13 The distribution of mulliken charges depend on the substitution site and its chirality.

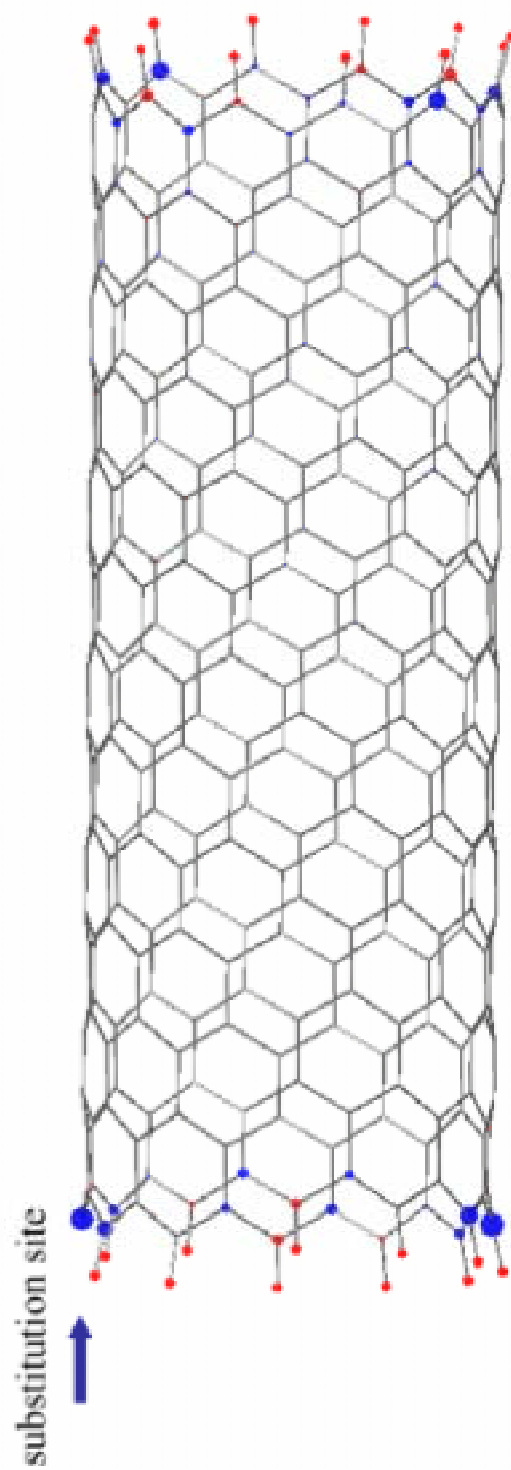


Fig. 1.14 The distribution of mulliken charges depend on the substitution site and its chirality.

### ***1.3 Conclusion***

The difference of Mulliken charges was observed in the opposite shore against the position of the substituted nitrogen atom between Global and Parent by semi-empirical MO methods, ONIOM(MP2:AM1), and DFT. This means that the computational methods of higher accuracy gave similar results of abnormal phenomena "TET," which had been observed by HMO method.

Moreover we observed the lowest heat of formation for the chiral nanotube (10,2). We also noted that the HOMOs were delocalized one open side. This feature of the HOMOs indicates that nanotubes could grow easier on one side than the others, since the growth mechanism of carbon nanotube is described the interaction of attachment between basement and the seed of carbon nanotube. Namely, it seems that the interaction happens at one open-end effectively.



## **Chapter 2**

Density Functional Theory on Ru(II) used as intercalators in  
DNA





There has been increasing interest in the last decade to the design of transition metal complexes spectroscopically active as probes of DNA structure and function. Since the first report on  $[\text{Ru}(\text{bpy})_2(\text{dppz})]^{2+}$  (bpy = 2,2'-bipyridine, dppz = dipyrido [3,2-a-2',3'-c] - phenazine) operating as a molecular "light switch" for DNA to be a prime candidate for application as a spectroscopic probe for nucleic acids owing to its shape and the sensitivity of its excited-state properties to environment [71]. Several Ru (II) complexes have been investigated:  $[\text{Ru}(\text{phen})_2\text{dppz}]^{2+}$  (phen = 1,10-phenanthroline) gives substantial increases in luminescence on DNA binding and may prove useful in the development of DNA-based diagnostics [72] [73]. In  $[\text{Ru}(\text{phen})_2\text{dppz}]^{2+}$  dppz is fully intercalated [74] [75]. Studies reported on  $[\text{Ru}(\text{phen})_3]^{2+}$  concluded that one phen ligand is facing the DNA base pairs and is nearly parallel to them as if intercalated. Moreover  $[\text{Ru}(\text{TAP})_2\text{dip}]^{2+}$  (TAP = 1,4,5,8-tetraazaphenanthrene, dip = 4,7-diphenylphenanthroline) tethered to a central nucleotide base have been prepared and characterized [76]. Additionally  $[\text{Ru}(\text{phen})_2\text{PHEHAT}]^{2+}$  and  $[\text{Ru}(\text{TAP})_2\text{PHEHAT}]^{2+}$  (PHEHAT = 1,10-phenanthrolino[5,6-b]-1,4,5,8,9,12-hexaazatriphenylene) were examined and compared containing either an extended planar ligand (dppz) or  $\pi$ -acceptor ligands [85]. Similarly spectroscopic changes similar to the reaction between  $[\text{Ru}(\text{TAP})_3]^{2+}$  and DNA are found with GMP in oxygen-free pH 5 solution. Likewise  $[\text{Ru}(\text{TAP})_2\text{dppz}]^{2+}$  is expected to intercalate into DNA in a fashion similar to that of  $[\text{Ru}(\text{phen})_2\text{dppz}]^{2+}$  [77] [78].

Some of these complexes are remarkable reporters of DNA structures by luminescing brightly on binding to DNA whereas no detectable photoluminescence is observed in aqueous solution. Appreciable luminescence has been detected in other solvents such as acetonitrile. The chemical properties of these coordinatively saturated molecules which

are water soluble and inert to substitution made them excellent compounds as new diagnostic and therapeutic agents [79]. The luminescent parameters are remarkably sensitive to the DNA structure and binding modes at intercalation: It is instructive to consider the metal complex as composed of one symmetric and one dissymmetric part, the ligand containing the one ligand for  $C_2$  axis and the two ligands "propeller blades". Only the latter, dissymmetric part can give rise to diastereomeric interaction. The orientation of the complex around the  $C_2$  axis (roll angle) will modulate this interaction. If the roll angle  $\alpha$ , had been exactly zero for the Ru(II) complexes, the angle between the polarized transition moments and the DNA axis should have been  $+35^\circ$ . The clockwise roll will correspond to directions of the polarized intensity at the angles  $(+35^\circ + \alpha)$  at the relative to the helix axis. Hence the angles around  $+10^\circ$  for dppz ligand is obtained (See Fig.2.6) [75].

Most of the experimental studies have been devoted to the structural aspects [73] [75] with a few investigations concerning the photophysical properties of the intercalated complex [80]. It appears that the key of the mechanism of photoluminescence is the presence of a low-lying emissive triplet MLCT (Metal-to-Ligand-Charge-Transfer) state, the lifetime of which being controlled by the environmental effects (site of intercalation, solvent) and the nature of the surrounding phen, TAP, bpy or dmp ligands. Experiments reported on various Ru (II) complexes have shown that their intercalation induces efficient cleavage of DNA upon photoexcitation at a wavelength of 400-450 nm [81, 82 83].

Recent developments have shown that Ru(II) complexes of the type  $[\text{Ru}(\text{TAP})_2\text{dppz}]^{2+}$  and  $[\text{Ru}(\text{phen})_2\text{dppz}]^{2+}$  are very efficient "molecular light switches" [84] and can block DNA transcription [81]. Therefore, they have received a considerable attention as DNA markers and potential anti-cancer drugs. Recent laser flash photolysis experiments have examined the photophysical/electrochemical properties of  $[\text{Ru}(\text{TAP})_2\text{dppz}]^{2+}$ ,  $[\text{Ru}(\text{phen})_2\text{dppz}]^{2+}$  and  $[\text{Ru}(\text{TAP})_2(\text{L})]^{2+}$  ( $\text{L}=\text{bpy}$ , phen, TAP) in water and with different polynucleotides [85]; it is suggested that a proton-coupled electron transfer mechanism is operative, but how this phenomenon takes place at the molecular level is not understood yet. It has been postulated that the initial electron transfer from the guanine to the metal complex in the case of  $[\text{Ru}(\text{TAP})_2\text{dppz}]^{2+}$  could increase the yield of strand cleavage and adduct formation.

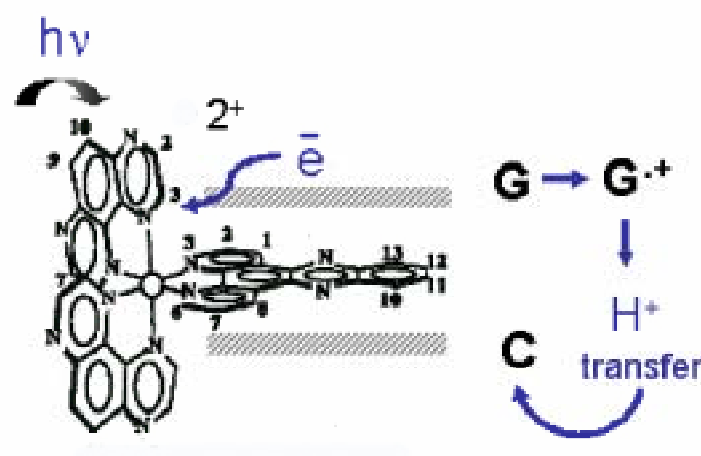


Fig. 2.1 The both back and forth reactions (( i ) ( ii )) proceed by proton coupled electron transfer, as this can explain the isotope effect. In the case of GMP, it is likely that the solvent acts as the proton acceptor whereas in the double standard DNA or polymucleotide the cytosine probably becomes protonated.

While direct evidence for electron transfer has been obtained with guanosine monophosphate, the process in DNA is too fast to be measured using nanosecond techniques and must occur on a picosecond time scale. A disadvantage of  $[\text{Ru}(\text{TAP})_2\text{phen}]^{2+}$  is that the mode of binding is uncertain this is why picosecond experiments were reported on  $[\text{Ru}(\text{TAP})_2\text{dppz}]^{2+}$ , which is expected to intercalate into DNA in a fashion similar to that of  $[\text{Ru}(\text{phen})_2\text{dppz}]^{2+}$  with comparable oxidizing properties of those of  $[\text{Ru}(\text{TAP})_2\text{phen}]^{2+}$ .

Nanosecond transient resonance Raman and picosecond transient absorption spectroscopic investigations of the two structurally analogous Ru-polypyridyl complexes,  $[\text{Ru}(\text{TAP})_2\text{dppz}]^{2+}$  and  $[\text{Ru}(\text{phen})_2\text{dppz}]^{2+}$ , have been reported. This study points to the different nature of the lowest excited states in the two complexes, and describes the role of these states within the very distinct photophysical behaviour of each, both in relation to solvent response and their interaction with DNA (facilitated in each case through the intercalating dppz ligand) [76, 86]. The active, solvent-sensitive, dppz-based  $^3\text{MLCT}$  states involved in the “light-switch” behaviour of  $[\text{Ru}(\text{phen})_2\text{dppz}]^{2+}$  are probed, alongside evidence of a progression through a precursor transient state when the complex is in non-aqueous environment. Evidence has been provided of a photophysical pathway for  $[\text{Ru}(\text{TAP})_2\text{dppz}]^{2+}$ , involving formation of a tap-based lowest  $^3\text{MLCT}$  state. When  $[\text{Ru}(\text{TAP})_2\text{dppz}]^{2+}$  is bound to DNA through the dppz ligand, a photo-driven electron transfer process ensues between the guanine base of DNA and the lowest  $^3\text{MLCT}$  state.

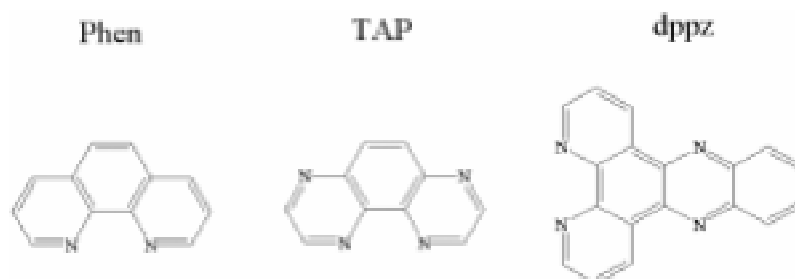


Fig. 2.2 The study of the ligands. Phen: 1,10-phenanthroline TAP: 1,4,5,8-tetraazaphenanthrene - dppz: dipyrido [3,2-a :2',3'-c]

The origin of the “light switch” effect has been believed to be removing of the water molecules surrounding the  $[\text{Ru}(\text{phen})_2\text{dppz}]^{2+}$  complex by intercalation of its large dppz ligand between DNA base pairs, although the direction of intercalation, i.e., whether the insertion of the large ligand occurs from the minor groove.

The structural property of DNA has two grooves of unequal character. The major groove is deep and wide, and the minor groove is narrow and shallow.

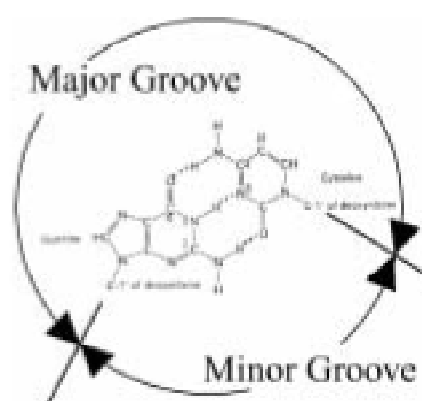


Fig. 2.3 Major groove and minor groove by Z-DNA.

As far as the binding modes of Ru (II) complexes to DNA is concerned, there are still divergences of opinion. For  $[\text{Ru}(\text{phen})_2\text{dppz}]^{2+}$  the classical intercalative mode is accepted by most scientists, but there are still intense controversies on binding to DNA with major or minor groove.

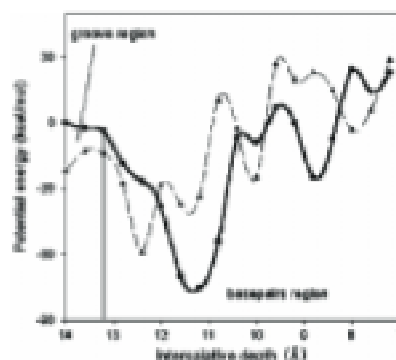


Fig 2.4 Potential curve for the  $[\text{Ru}(\text{phen})_2\text{dppz}]^{2+}$  binding B-DNA [87]. Heavily line presents minor groove intercalation; dashed line for major groove was carried out calculation with the Amber96.

Molecular modeling methods have been applied recently to study the structural characterization of the interaction of transition metal complexes containing ligands such as bpy, phen with the oligonucleotide  $\text{d}(\text{CGCAATTGCG})_2$  [87]. Fig. 2.4 shows the potential curve for  $[\text{Ru}(\text{phen})_2\text{dppz}]^{2+}$  binding B-DNA. In the groove bound region of the major groove, the global minimum occurs, which indicates that the complex might have bound hydrophobically against the major groove. In addition, a local minimum is also observed in the base-pairs region of the major groove.

Also, the potential of the minor groove is generally lower than that of the major groove in base-pairs region. If the structure corresponding to the global minimum point is considered as the optimum binding conformation between complexes and B-DNA, the  $[\text{Ru}(\text{phen})_2\text{dppz}]^{2+}$  binding should be a classical intercalation from minor groove with completely separated basepairs, viewed from Fig. 2.5.

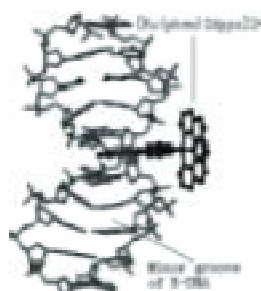


Fig. 2.5  $[\text{Ru}(\text{phen})_2\text{dppz}]^{2+}$  was intercalated to minor groove of B-DNA[87].

The dppz head is engaged in stacking interaction with the nucleobases, which is in good qualitative agreement with experiment description [87]. Although  $[\text{Ru}(\text{TAP})_2\text{dppz}]^{2+}$  and  $[\text{Ru}(\text{phen})_2\text{dppz}]^{2+}$  have different photophysical and photochemical behaviours, their affinity constants for polynucleotides are of the same order of magnitude,

presumably reflecting the efficient intercalation properties of the dppz ligand. The structure of the  $[\text{Ru}(\text{TAP})_2\text{dppz}]^{2+}$  intercalating DNA is adapted the same as  $[\text{Ru}(\text{phen})_2\text{dppz}]^{2+}$ .

The main objective of the present theoretical study based on quantum chemical calculations is to determine the geometrical structures of the  $[\text{Ru}(\text{L})_2(\text{L}')^{2+}]$  complexes with  $\text{L}=\text{L}'=\text{TAP}$ ;  $\text{L}=\text{phen}$ ,  $\text{L}'=\text{dppz}$ ;  $\text{L}=\text{TAP}$ ,  $\text{L}'=\text{dppz}$  in vacuum as well as in different solvents and in biological environment. The electronic absorption spectroscopy of  $[\text{Ru}(\text{L})_2\text{dppz}]^{2+}$  ( $\text{L}=\text{phen}$ ,  $\text{TAP}$ ) is also investigated in order to characterize the low-lying singlet and triplet excited states playing a role in the mechanism of photoluminescence observed in these compounds. The solvent effects on the absorption spectra are also considered. Hybrid QM/MM methods are used to optimize the structures in the biological environment.

The computational details are given in the next section, whereas the structures and spectroscopy are analysed in section 2 and the intercalated models are discussed in section 3.

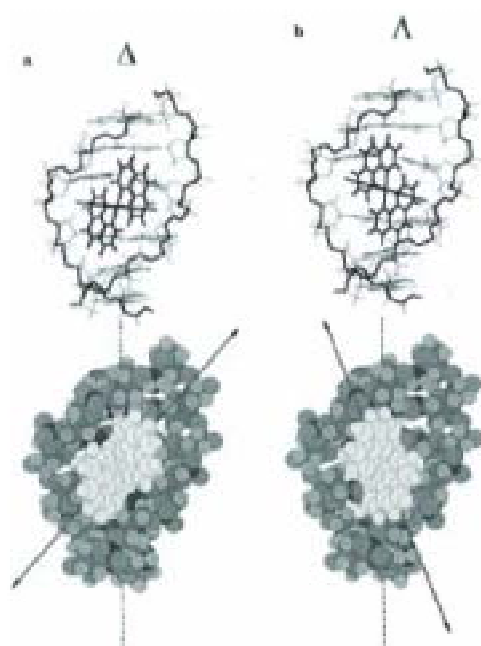


Fig.2.6 Models illustrating the diastereomeric binding geometries of the  $[\text{Ru}(\text{phen})_2\text{Ligand}]^{2+}$  complexes intercalated and oriented perpendicular to the DNA helix axis. For both enantiomeric forms the spectroscopic results show the complex to be tilted from the idealized intercalative geometry by a clockwise roll around its  $C_2$  axis with a roll angle of about  $10^\circ$  [75].

## 2.1 Computational Details

### 2.1.1 Geometry Optimization

The geometries of the molecules in their electronic ground state were optimized at the DFT(B3LYP) level of theory using a Becke's 3-parameter hybrid functional using the nonlocal correlation functional due to Lee, Yang, and Par [88]. MWB basis set which references to neutral atom and Wood-Boring quasi-relativistic pseudopotentials [89] and associated valence basis sets (8s, 7p, 6d) contracted to [6s, 5p, 3d] were used for the Ru (II) atom. Polarized split valence basis sets which can in turn be composed of a fixed linear combination of primitive Gaussian functions 6-31G\* [90,91] were used for a (4s) contracted to [2s] for H and a (10s, 4p, 1d) set contracted to [3s, 2p, 1d] for C and N atoms on the  $[\text{Ru}(\text{L})_2(\text{L}')^{2+}]$  complexes with L=L'=TAP; L=phen, L'=dppz; L=TAP, L'=dppz. Preliminary calculations were performed on  $[\text{Ru}(\text{TAP})_2(\text{L}'')^{2+}]$  with L''=TAP; L''=dppz, by means of D95 basis sets which are Dunning-Huzinaga full double zeta [92] (4s) contracted to [2s] for H and either (9s, 5d) set contracted to [4s, 2p] or (10s, 5p) contracted to [3s, 2p] for C and N combined to the LANL2DZ [92] Effective Core Potentials and associated valence basis set on Ru atom.

### 2.1.2 Spectroscopy

Time-dependent density functional theory (TD-DFT) which is a method for the calculation of excitation energies by systematic improvement upon the poles of the Kohn-Sham response function and configuration interaction singles approximation were used to calculate the transition energies to the electronic excited states in vacuum and solvents. The solvent effects were investigated by means of the polarizable continuum model (PCM) which allows to treat in a single approach dielectrics of different nature: standard isotropic liquids, intrinsically anisotropic media like liquid crystals and solid matrices, or ionic solutions and performs reaction field calculation using  $\text{CH}_3\text{CN}(\epsilon=36.64)$  and  $\text{H}_2\text{O}(\epsilon=78.39)$  environment in TD-DFT. A procedure based on the PCM has been applied to reproduce solvent effects on electronic spectra in connection with the TD-DFT. To account for solute-solvent interactions, a suitable operator has been defined, which depends on the solute electronic density and can be used to modify the TD-DFT equations for the calculation of molecular polarizabilities and electronic transition energies. The solute-solvent operator has been derived from a PCM



approach depending on solute electrostatic potential.

### 2.1.3 Intercalating to DNA

To analyze the poly [d(G-C)] the X-ray structural data from PDB[93] of 6CG are optimized by AM1 level. Here the hydrogen bonds were attached by winmostar [94]. For the intercalating to DNA, the structure by Facio [95] at docking area and translated from the pdb data to gaussian input files using Babel [96] was used. ONIOM is a hybrid method that enables different levels of theory to be applied to different parts of a molecule and system which are combined to produce a consistent energy expression. Energies were obtained via the ONIOM hybrid QM/MM method. The ONIOM energy for a two-layer system is calculated by

$$E(\text{Real: High}) = E(\text{Core: High}) + [E(\text{Real: Low}) - E(\text{Core: Low})]$$

where Real and Core indicate the molecular layers, and High and Low indicate the level of theory.  $[\text{Ru}(\text{TAP})_2\text{dppz}]^{2+}$  and 2CG was chosen as the ONIOM core, and high level of theory was the B3LYP xc-functional theory and D95 basis set for hydrogen, carbon and nitrogen, MWB basis set for Ru(II). The Low level method was UFF (Universal Force Field) which set of fundamental parameters is based only on the element, its hybridization, and connectivity. At the present stage it is difficult to calculate the Ru(II) complexes by QM/QM since there is no library of the Ru(II) on the semi-empirical methods. We performed the following methods about  $[\text{Ru}(\text{TAP})_2\text{dppz}]^{2+}$  intercalating DNA.

The simulation of the complexes bound to 6CG was carried out using docking methodology [97]. First, the complex was selected to insert into the  $\text{C}_3\text{G}_4/\text{G}_3\text{C}_4$  (C: Cytosine, G: Guanine). The dppz two-fold axis is perpendicular to both the base pair long axis and the helical axis.

Manually changing the intercalative depth of the complex by MM method, the structures along the designed pathway were constructed individually, and then independently minimized to obtain the potential value of the interaction system consisting of the complex and Z-DNA. To obtain the structure we choose the 3 schemes.

The  $[\text{Ru}(\text{TAP})_2\text{dppz}]^{2+} + 6\text{CG}$  geometry optimization was carried out by

- 1) the MM method for all the atoms. (Non-fixed)
- 2) QM/MM. (Non-fixed)

3) QM/MM. (MM part fixed and single-point calculation was performed.)

All the calculations reported in this study have been performed Gaussian03 program package.

## 2.2 $[Ru(TAP)_2dppz]^{2+}$ , $[Ru(TAP)_3]^{2+}$ and $[Ru(Phen)_2dppz]^{2+}$

### 2.2.1 Structure of the metal complexes

The optimized geometries of Ru complexes in vacuum are reported in Table 2.1. Since the X-ray data for the  $[Ru(TAP)_2dppz]^{2+}$  was not obtained we compared the X-ray data for  $[Ru(TAP)_3]^{2+}$ . Optimized structures obtained show pseudo-octahedral condition of  $RuN_6$  core, with N-Ru-N angles close to 80 degrees. These Ru complexes don't keep the octahedral symmetry correctly. The angle of N-Ru-N which is connected with the TAP, namely  $N_3-Ru-N_4$  and  $N_5-Ru-N_6$  have the same value. Note that the angle which is connected with dppz ligand becomes somewhat narrower than that of TAP. Comparison between  $[Ru(TAP)_2dppz]^{2+}$  and  $[Ru(phen)_2dppz]^{2+}$  indicates that all the angles which connect TAP/Ru/TAP have almost the same value. The agreement between experimental data and calculated values for the  $[Ru(TAP)_3]^{2+}$  complex is rather good. The calculated geometries are slightly affected by the basis sets effects as illustrated by the values reported in Table 2.1.

Table 2.1 DFT optimized geometries of Ru(II) complexes. X-ray data for  $[Ru(TAP)_3]^{2+}$ .

	$[Ru(TAP)_2dppz]^{2+}$		$[Ru(phen)_2dppz]^{2+}$	$[Ru(TAP)_3]^{2+}$			Exp.
	Optimization		Optimization	Optimization			
B3LYP	D95	6-31G*	6-31G*	D95	LanL2DZ	6-31G*	Exp.
Ru-N1	2.10	2.11	2.11	2.10	2.10	2.11	2.06
Ru-N2	2.10	2.11	2.11	2.10	2.10	2.11	2.08
Ru-N3	2.09	2.11	2.11	2.10	2.10	2.11	2.06
Ru-N4	2.10	2.12	2.11	2.10	2.10	2.12	2.05
Ru-N5	2.10	2.12	2.11	2.10	2.10	2.11	2.06
Ru-N6	2.09	2.11	2.11	2.10	2.10	2.11	2.08
N1-Ru-N2	79.4	78.7	78.6	80.1	80.1	79.3	79.4
N1-Ru-N4	173.0	172.9	173.2	173.2	173.2	173.0	175.1
N2-Ru-N5	173.0	172.9	173.2	173.2	173.4	173.0	169.8
N3-Ru-N4	80.2	79.4	78.8	80.1	80.1	79.3	80.4
N3-Ru-N6	174.1	173.8	173.2	173.4	173.4	173.0	172.3
N5-Ru-N6	80.2	79.4	78.8	80.1	80.1	79.4	80.6

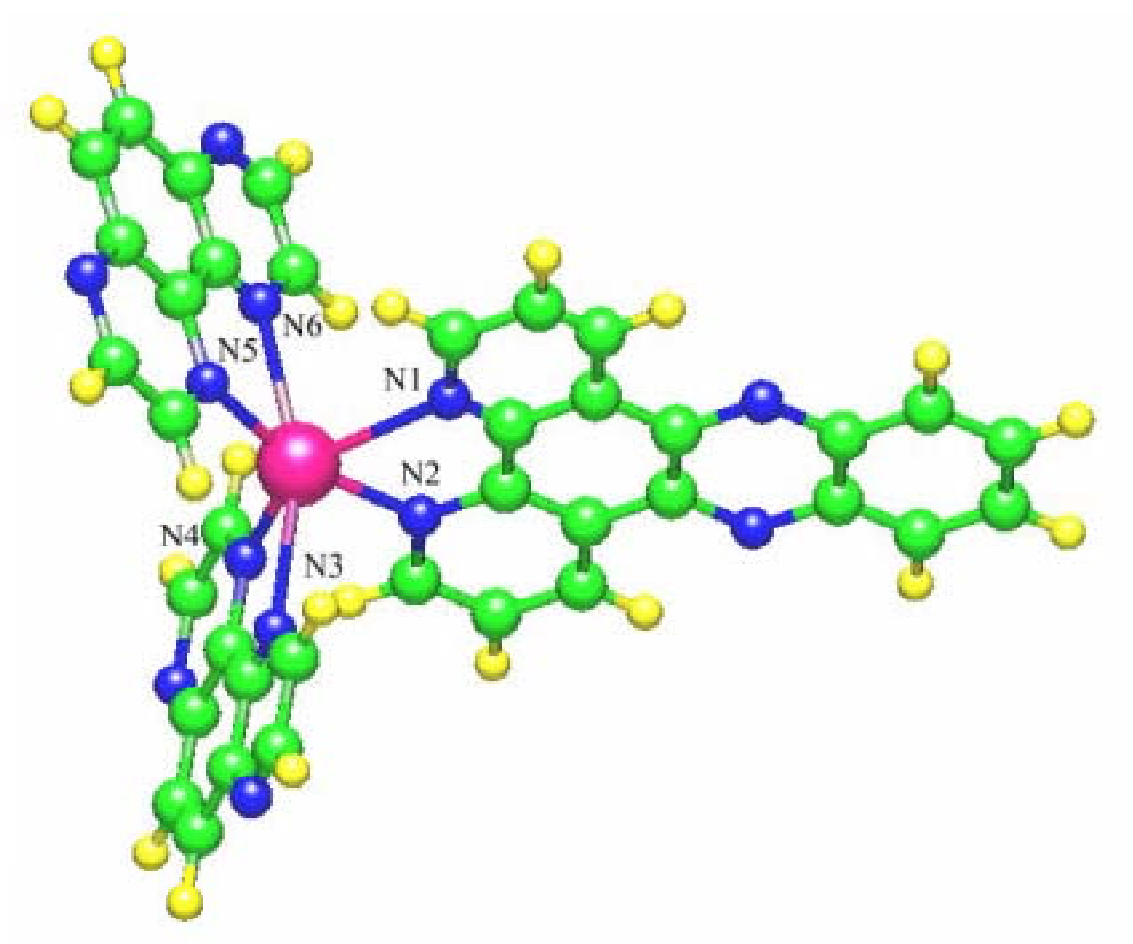


Fig. 2.7 The optimized structure of  $[\text{Ru}(\text{TAP})_2\text{dppz}]^{2+}$  complex and the numbering of the nitrogen.

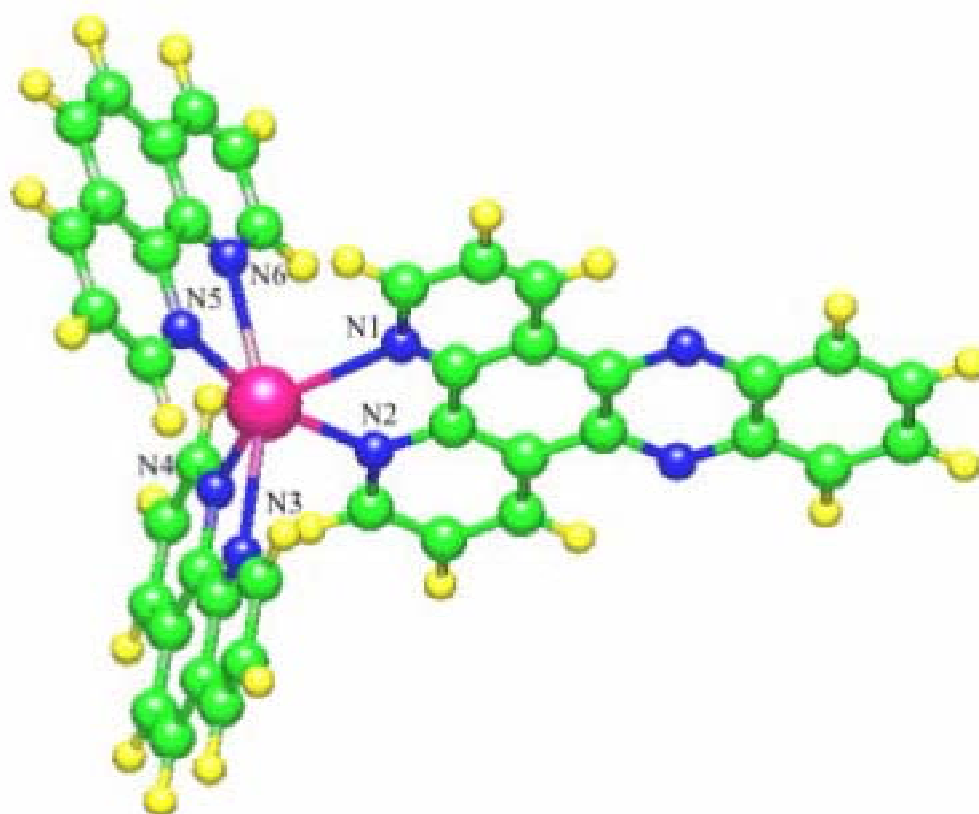


Fig. 2.8 Optimized structure of the  $[\text{Ru}(\text{phen})_2\text{dppz}]^{2+}$  complex.

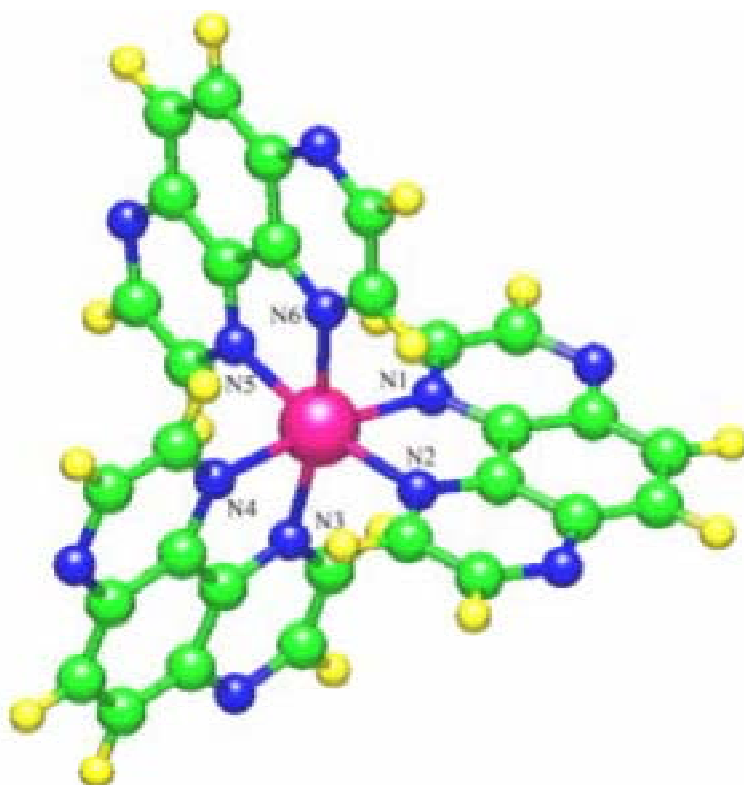


Fig. 2.9 Optimized structure of the  $[\text{Ru}(\text{TAP})_3]^{2+}$  complex.

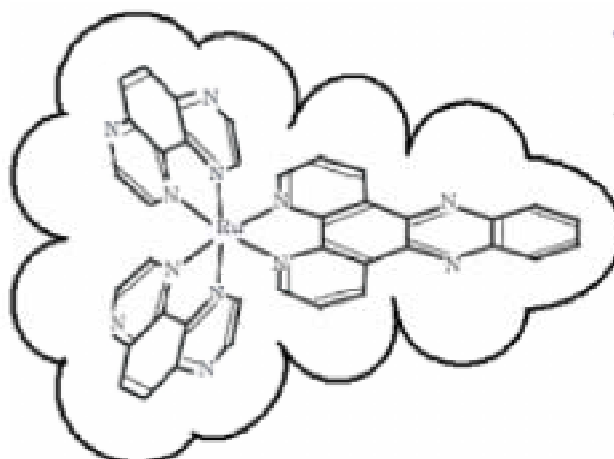


Fig. 2.10. Surface generated by overlapping van der Waals spheres modelling the cavity scheme around the  $[\text{Ru}(\text{TAP})_2\text{dppz}]^{2+}$  complex.

Tentative optimized geometries taking into account the solvent effects ( $\text{H}_2\text{O}$  or  $\text{CH}_3\text{CN}$ ) are reported in Tables 2.2 (a) and 2.2 (b) for  $[\text{Ru}(\text{TAP})_2\text{dppz}]^{2+}$ . A severe problem of convergence inherent to the PCM method occurs for both solvents as compared to the calculations in vacuum. It could be a consequence of the flexibility of this large molecular system which cannot be handled by this simple cavity model. At a first glance the bond Ru-N distances seem to be only slightly affected by the solvent effects. However further calculations should be performed in order to get more serious conclusion. Consequently the TD-DFT calculations including solvent effects and reported in the next section have been performed on the vacuum optimized geometry of both molecules in the electronic ground state.

Table 2.2 (a) The Ru-N bond lengths including  $\text{CH}_3\text{CN}$  solvent effect.

Ru-N1 (Å)	Ru-N2 (Å)	Ru-N3 (Å)	Ru-N4 (Å)	Ru-N5 (Å)	Ru-N6 (Å)	KS Energy (a.u.)
2.11	2.11	2.10	2.11	2.11	2.10	-2213.13930895
2.11	2.11	2.10	2.11	2.11	2.10	-2213.13963972
2.12	2.12	2.11	2.12	2.12	2.11	-2213.13970160
2.11	2.11	2.11	2.11	2.11	2.10	-2213.13909050
2.11	2.11	2.10	2.11	2.11	2.10	-2213.13950028
2.11	2.11	2.10	2.11	2.11	2.10	-2213.13958783

Table 2.2 (b) The Ru-N bond lengths including H<sub>2</sub>O solvent effect.

Ru-N1 (Å)	Ru-N2 (Å)	Ru-N3 (Å)	Ru-N4 (Å)	Ru-N5 (Å)	Ru-N6 (Å)	KS Energy (a.u.)
2.11	2.11	2.10	2.11	2.11	2.10	-2213.14789773
2.11	2.11	2.10	2.11	2.11	2.10	-2213.14796323
2.12	2.12	2.11	2.12	2.12	2.11	-2213.14796343
2.11	2.11	2.10	2.11	2.11	2.10	-2213.14777980
2.11	2.11	2.10	2.11	2.11	2.10	-2213.14749079

### 2.2.2 Spectroscopy

The experimental absorption /emission data for various Ru (II) complexes in H<sub>2</sub>O and CH<sub>3</sub>CN are reported in Tables 2.3. A comparative analysis of the UV-visible absorption data of [Ru(TAP)<sub>2</sub>L]<sup>2+</sup> (L= dppz, phen) and [Ru(phen)<sub>2</sub>dppz]<sup>2+</sup> points to a blue shift of the absorption energies when replacing the phen ligand by dppz with an absorption at 440 nm for [Ru(phen)<sub>2</sub>dppz]<sup>2+</sup> shifted at 410 nm ([Ru(TAP)<sub>2</sub>phen]<sup>2+</sup>) or 412 nm ([Ru(TAP)<sub>2</sub>dppz]<sup>2+</sup>). Both bands are solvent independent and correspond to MLCT (Metal-to-Ligand-Charge-Transfer) excited states. This band has been attributed to a charge transfer from Ru to dppz in [Ru(phen)<sub>2</sub>dppz]<sup>2+</sup> whereas the most bathochromic band observed around 370 nm is assigned to IL (Intra Ligand) transition corresponding to π π\* excitation localized on the dppz [98].

Table 2.3 (a) and (b) Experimental absorption data and Emission data for the Ru(II) complexes. At the emission data, the [Ru(phen)<sub>2</sub>dppz]<sup>2+</sup> doesn't emit in water [85].

Table 2.3 (a)

Complexes / Solvent	H <sub>2</sub> O	CH <sub>3</sub> CN
[Ru(TAP) <sub>2</sub> dppz] <sup>2+</sup>	204, 230, 278,366, 412, 454	278, 362, 412, 458
[Ru(TAP) <sub>2</sub> phen] <sup>2+</sup>	202, 230, 272, 410, 466	272, 412, 458
[Ru(phen) <sub>2</sub> dppz] <sup>2+</sup>	264, 278, 318, 358, 372, 440	264, 276, 316, 352, 360, 368, 440

Table 2.3 (b)

Complexes / Solvent	H <sub>2</sub> O	CH <sub>3</sub> CN
[Ru(TAP) <sub>2</sub> dppz] <sup>2+</sup>	636	621
[Ru(TAP) <sub>2</sub> phen] <sup>2+</sup>	645	626
[Ru(phen) <sub>2</sub> dppz] <sup>2+</sup>	-	630

From time-resolved absorption and emission spectroscopy experiments reported for [Ru(phen)<sub>2</sub>dppz]<sup>2+</sup> it has been postulated that the prompt emission (within ps time scale) occurs from a low-lying <sup>3</sup>MLCT state accessible either from the initial <sup>1</sup>MLCT absorbing state or after internal conversion to a low-lying <sup>1</sup>MLCT state. The proposed mechanism is solvent dependent [98]. An active solvent sensitive dppz-based <sup>3</sup>MLCT state has been probed by means of nanosecond transient resonance Raman and picosecond transient absorption spectroscopy of [Ru(phen)<sub>2</sub>dppz]<sup>2+</sup> and [Ru(TAP)<sub>2</sub>dppz]<sup>2+</sup> [77].



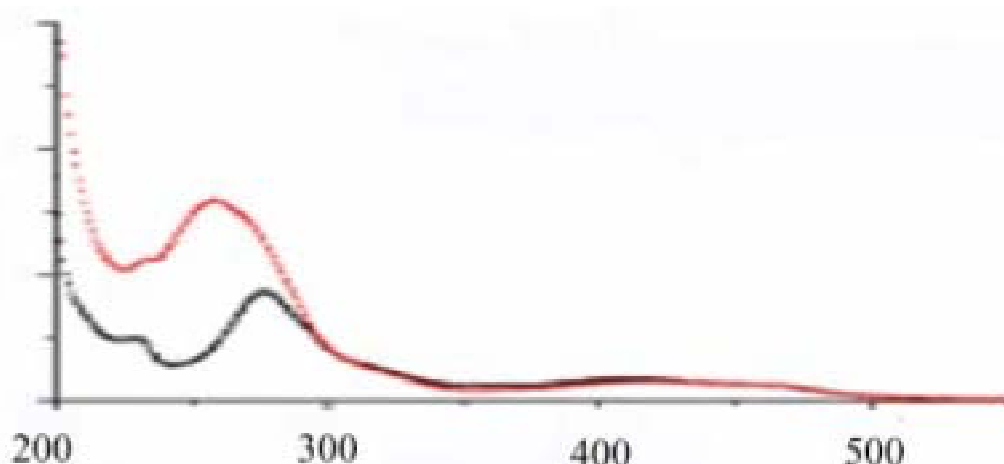


Fig. 2.10 UV/visible absorption spectra of  $[\text{Ru}(\text{TAP})_2\text{dppz}]^{2+}$  ( $8 \times 10^{-6}$  M) in (black line) 10 mM phosphate buffer and (red line) with the addition of  $[\text{poly}(\text{dG-dC})]^{2+}$  ( $1.6 \times 10^{-4}$  M nucleotide) [78].

The UV/visible absorption spectra of  $[\text{Ru}(\text{TAP})_2\text{dppz}]^{2+}$ , free molecule or in the biological environment is depicted on Figure 2.10 [78]. It is characterized by a shoulder between 410 and 460 nm and a strong absorption at about 278 nm shifted to the blue in the biological surrounding.

In order to get a qualitative picture of the absorption spectrum of  $[\text{Ru}(\text{TAP})_2\text{dppz}]^{2+}$  preliminary tentative CIS calculations have been performed. The transition energies are reported in Table 2.4. The first intense band is found at 272 nm and corresponds to a dppz-based IL transition, the next one are calculated above 230 nm with two intense bands assigned to MLCT states from Ru to TAP. There is no evidence of absorption between 400 and 500 nm and around 300 nm in contrast to the experimental spectrum. These results which systematically overestimate the transition energies illustrate the limit of this simple method based on single excitations. In order to improve the theoretical results we have performed further calculations based on TD-DFT method.

The calculated TD-DFT (with and without solvent) transition energies to the singlet and triplet excited states of  $[\text{Ru}(\text{TAP})_2\text{dppz}]^{2+}$  and  $[\text{Ru}(\text{phen})_2\text{dppz}]^{2+}$  and associated oscillator strengths are reported in Tables 2.5 to 2.8 the corresponding graphic presentations are depicted in Fig. 2.11 – 2.15. The theoretical absorption spectra of these molecules are characterized by a high density of states between 500 and 300 nm. Whereas the lowest part (between 500 and 400 nm) of  $[\text{Ru}(\text{phen})_2\text{dppz}]^{2+}$  spectrum is described essentially by MLCT states corresponding to charge transfer from Ru to the low-lying  $\pi^*$  orbitals localized on the phen or ddpz ligands the spectrum of the TAP substituted complex is depicted by a variety of different excited states such as MLCT ( $d_{\text{Ru}} \rightarrow \pi^*_{\text{TAP}}$ ), LLCT ( $\text{dppz} \rightarrow \text{TAP}$ ) and IL ( $\text{dppz} \rightarrow \text{dppz}$ ). The calculated spectrum of

$[\text{Ru}(\text{TAP})_2\text{dppz}]^{2+}$  reproduces the main experimental features with a moderate absorption at 429/427 nm assigned to  ${}^1\text{IL}(\text{dppz} \rightarrow \text{dppz}) / {}^1\text{MLCT}(\text{Ru} \rightarrow \text{TAP})$  absorbing states and a strong absorption starting at 305 nm and corresponding to a Ru to dppz  ${}^1\text{MLCT}$  state. The theoretical spectrum of  $[\text{Ru}(\text{phen})_2\text{dppz}]^{2+}$  differs from the one of  $[\text{Ru}(\text{TAP})_2\text{dppz}]^{2+}$  by the presence of an absorption at 411 nm attributed to a singlet MLCT state corresponding to a  $d_{\text{Ru}} \rightarrow \pi^*_{\text{dppz}}$  excitation which is rejected to the upper part of the spectrum in the tap substituted molecule (at about 300 nm). Finally the spectrum of  $[\text{Ru}(\text{phen})_2\text{dppz}]^{2+}$  shows an intense  ${}^1\text{IL}(\pi_{\text{dppz}} \rightarrow \pi^*_{\text{dppz}})$  state calculated at 304 nm with an oscillator strength of 0.8771 which can be attributed to the band observed at 318 nm ( $\text{H}_2\text{O}$ ) and 316 nm ( $\text{CH}_3\text{CN}$ ) (cf Fig2.11). This very intense band does not exist in the spectrum of  $[\text{Ru}(\text{TAP})_2\text{dppz}]^{2+}$  in agreement with the experiments [78].

The TD-DFT calculations including solvent correction for the  $[\text{Ru}(\text{TAP})_2\text{dppz}]^{2+}$  complex are reported in Tables 2.7 and 2.8 for  $\text{CH}_3\text{CN}$  and  $\text{H}_2\text{O}$ , respectively.

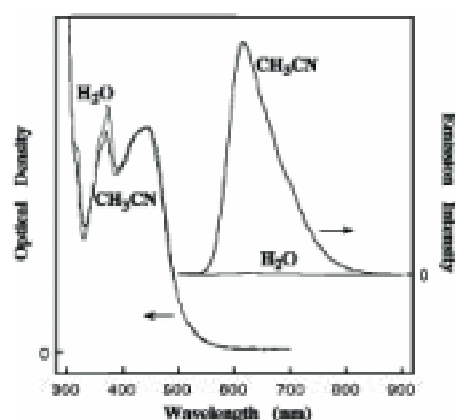


Fig. 2.11 Absorption and emission spectra for  $[\text{Ru}(\text{phen})_2\text{dppz}]^{2+}$  in  $\text{CH}_3\text{CN}$  and  $\text{H}_2\text{O}$  [98].

As far as the solvent effects are concerned we may extract a few significant results concerning some of the excited states of interest. The strongly absorbing state calculated at 305 nm in vacuum and assigned to the  ${}^1\text{MLCT}(d_{\text{Ru}} \rightarrow \pi^*_{\text{dppz}})$  observed at about 278 nm in  $\text{H}_2\text{O}$  or  $\text{CH}_3\text{CN}$  (Table 2.3, Fig. 2.10) is shifted to 296 nm ( $\text{CH}_3\text{CN}$  model) and 293 nm ( $\text{H}_2\text{O}$  model) with increasing oscillator strengths. The  ${}^1\text{IL}$  band calculated at 382 nm in vacuum and corresponding to a charge transfer from the  $\pi_{\text{dppz}}$  orbital localized far away from the metal center to a vacant  $\pi^*_{\text{dppz}}$  orbital localized nearby the metal center (see figure 2.16) is shifted to 388 nm ( $\text{CH}_3\text{CN}$ ) and 390 nm ( $\text{H}_2\text{O}$ ). The largest oscillator strengths are obtained in acetonitrile for both transitions. This transition

entirely localized on the dppz ligand corresponds probably to the band observed at 366 nm ( $\text{H}_2\text{O}$ ) and 362 nm ( $\text{CH}_3\text{CN}$ ) which does not exist in the spectrum of  $[\text{Ru}(\text{TAP})_2\text{phen}]^{2+}$ . Finally the lowest  $^1\text{MLCT}$  ( $d_{\text{Ru}} \rightarrow \pi^*_{\text{TAP}}$ ) state calculated at 427 nm in vacuum originates from an excitation of an orbital which is a mixing between  $d_{\text{Ru}}$  and  $\pi_{\text{dppz}}$  (orbital 170 in Figure 2.16) more localized on the metal. When solvent corrections are taken into account this state becomes  $^1\text{LLCT}$  calculated at 404 nm ( $\text{H}_2\text{O}$ ) and 402 nm ( $\text{CH}_3\text{CN}$ ) and corresponds to an excitation from an orbital which is again a mixing between  $d_{\text{Ru}}$  and  $\pi_{\text{dppz}}$  (orbital 173 in Figure 2.16) but more localized on dppz.

Steady state luminescence and absorption measurements performed on  $[\text{Ru}(\text{phen})_2\text{dppz}]^{2+}$  in acetonitrile and water strongly suggested that the electronic character and energies of the Frank-Condon singlet excited MLCT ( $\lambda_{\text{max}} \approx 440$  nm) and  $\pi\pi^*$   $^1\text{IL}$  ( $\lambda_{\text{max}} \approx 380$  nm) are not significantly solvent dependent [98].

Table 2.4  $[\text{Ru}(\text{TAP})_2\text{dppz}]^{2+}$  excited states in vacuum by CIS.

nm	Singlets		<i>f</i>	Triplets		eV
475				<sup>3</sup> MLCT	(Ru→2TAP)	2.61
474				<sup>3</sup> MLCT	(Ru→2TAP)	2.61
366				<sup>3</sup> MLCT	(Ru→2TAP)	3.39
365				<sup>3</sup> MLCT	(Ru→2TAP)	3.39
363				<sup>3</sup> MLCT	(Ru→2TAP)	3.41
316				<sup>3</sup> IL	(dppz→dppz)	3.92
314				<sup>3</sup> MLCT	(Ru→2TAP)	3.95
291	<sup>1</sup> IL	(dppz→dppz)	0.0324			4.26
287				<sup>3</sup> MLCT	(Ru→2TAP)	4.32
287				<sup>3</sup> MLCT	(Ru→2TAP)	4.32
284				<sup>3</sup> MLCT	(Ru→dppz)	4.36
284				<sup>3</sup> MLCT	(Ru→dppz)	4.37
277				<sup>3</sup> IL	(dppz→dppz)	4.47
272	<sup>1</sup> IL	(dppz→dppz)	0.4920			4.56
256	<sup>1</sup> MLCT	(Ru→2TAP)	0.0206			4.85
256	<sup>1</sup> MLCT	(Ru→2TAP)	0.0527			4.85
252	<sup>1</sup> MLCT	(Ru→2TAP)	0.0024			4.93
248	<sup>1</sup> IL	(dppz→dppz)	0.0842			5.00
245				<sup>3</sup> LLCT	(dppz→2TAP)	5.06
245				<sup>3</sup> MLCT	(Ru→2TAP)	5.06
243	<sup>1</sup> LLCT	(dppz→2TAP)	0.0101			5.10
243	<sup>1</sup> LLCT	(dppz→2TAP)	0.0096			5.11
242	<sup>1</sup> LLCT	(2TAP→2TAP)	0.0019			5.12
242	<sup>1</sup> LLCT	(dppz→2TAP)	0.0001			5.12
241				<sup>3</sup> IL	(dppz→dppz)	5.15
237	<sup>1</sup> IL	(dppz→dppz)	0.0580			5.23
234				<sup>3</sup> IL	(dppz→dppz)	5.31
229	<sup>1</sup> MLCT	(Ru <sub>172</sub> →2TAP <sub>177</sub> )	0.4582			<b>5.41</b>
226	<sup>1</sup> MLCT	(Ru <sub>176</sub> →2TAP <sub>177</sub> )	0.7162			<b>5.50</b>
220	<sup>1</sup> IL	(dppz→dppz)	0.5053			5.63
219				<sup>3</sup> LLCT	(dppz→TAP)	5.65
217	<sup>1</sup> IL	(dppz <sub>174</sub> →dppz <sub>181</sub> )	2.2453			<b>5.72</b>
217				<sup>3</sup> LLCT	(TAP→dppz)	5.72
215				<sup>3</sup> MLCT	(Ru→2TAP)	5.77
214				<sup>3</sup> MLCT	(Ru→2TAP)	5.78
205	<sup>1</sup> LLCT	(dppz→2TAP)	0.6894			6.05
203				<sup>3</sup> LLCT	(TAP→2TAP)	6.10
201	<sup>1</sup> LLCT	(TAP→2TAP)	0.0199			6.16
201				<sup>3</sup> LLCT	(dppz→2TAP)	6.16
201	<sup>1</sup> IL	(2TAP→2TAP)	0.2505			6.18
200				<sup>3</sup> LLCT	(dppz→2TAP)	6.21
199	<sup>1</sup> IL	(dppz→dppz)	0.4492			6.22
198				<sup>3</sup> MLCT	(Ru→2TAP)	6.28
196				<sup>3</sup> MLCT	(Ru→2TAP)	6.31
196	<sup>1</sup> LLCT	(TAP→2TAP)	0.0044			6.33

196				<sup>3</sup> MLCT	(Ru→2TAP)	6.33
194	<sup>1</sup> IL	(dppz→dppz)	0.2596			6.39
193				<sup>3</sup> MLCT	(Ru→2TAP)	6.41
193	<sup>1</sup> LLCT	(dppz→2TAP)	0.0029			6.41
193				<sup>3</sup> LLCT	(dppz→2TAP)	6.42
193	<sup>1</sup> IL	(dppz→dppz)	0.0198			6.43
192	<sup>1</sup> LLCT	(TAP→2TAP)	0.0074			6.45
186				<sup>3</sup> LLCT	(dppz→2TAP)	6.66
185				<sup>3</sup> LLCT	(dppz→2TAP)	6.70
184	<sup>1</sup> LLCT	(dppz→2TAP)	0.1052			6.73
184				<sup>3</sup> LLCT	(dppz→2TAP)	6.76
183	<sup>1</sup> LLCT	(dppz→2TAP)	0.0159			6.77
183	<sup>1</sup> LLCT	(dppz→2TAP)	0.0033			6.79
182				<sup>3</sup> LLCT	(dppz→2TAP)	6.81
182	<sup>1</sup> LLCT	(TAP→dppz)	0.5076			6.82
181				<sup>3</sup> LLCT	(dppz→2TAP)	6.85
180	<sup>1</sup> LLCT	(TAP→dppz)	0.1043			6.89
178				<sup>3</sup> IL	(dppz→dppz)	6.96
178				<sup>3</sup> LLCT	(dppz→2TAP)	6.96
178				<sup>3</sup> LLCT	(dppz→2TAP)	6.96
178	<sup>1</sup> LLCT	(TAP→2TAP)	0.1936			6.97
178				<sup>3</sup> LLCT	(TAP→dppz)	6.99
176	<sup>1</sup> LLCT	(TAP→2TAP)	0.3345			7.04
176	<sup>1</sup> LLCT	(TAP→2TAP)	0.0745			7.05
175				<sup>3</sup> MLCT	(Ru→2TAP)	7.09
174	<sup>1</sup> IL	(dppz→dppz)	0.2161			7.13
170	<sup>1</sup> MLCT	(Ru→2TAP)	0.1685			7.28
170	<sup>1</sup> MLCT	(Ru→2TAP)	0.1994			7.29
169	<sup>1</sup> MLCT	(Ru→2TAP)	0.1327			7.34
167	<sup>1</sup> MLCT	(Ru→2TAP)	0.1037			7.45

Table 2.5  $[\text{Ru}(\text{TAP})_2\text{dppz}]^{2+}$  excited states in vacuum by TD-DFT (cf. Fig.2.12 ). Numbering refers to Fig.2.16.

Nm	Singlets	$f$	Triplets	eV
522			<sup>3</sup> MLCT (Ru → 2TAP)	2.38
518			<sup>3</sup> MLCT (Ru → 2TAP)	2.40
503			<sup>3</sup> MLCT (Ru → 2TAP)	2.47
487			<sup>3</sup> MLCT (Ru → 2TAP)	2.55
480	<sup>1</sup> MLCT (Ru → 2TAP)	0.0008		2.58
477	<sup>1</sup> MLCT (Ru → 2TAP)	0.0002		2.60
476			<sup>3</sup> MLCT (Ru → 2TAP)	2.60
470			<sup>3</sup> LLCT (dppz → 2TAP)	2.64
466			<sup>3</sup> MLCT (Ru → 2TAP)	2.66
<b>455</b>	<sup>1</sup> LLCT (dppz <sub>173</sub> → TAP <sub>175</sub> )	0.0043		<b>2.73</b>
439			<sup>3</sup> LLCT (dppz → 2TAP)	2.82
438			<sup>3</sup> IL (dppz → dppz)	2.83
433			<sup>3</sup> MLCT (Ru → 2TAP)	2.86
430			<sup>3</sup> MLCT (Ru → dppz)	2.88
429	<sup>1</sup> IL (dppz <sub>174</sub> → dppz <sub>175</sub> )	0.0118		<b>2.89</b>
427	<sup>1</sup> MLCT (Ru <sub>170</sub> → 2TAP <sub>175</sub> )	0.0387		<b>2.90</b>
427			<sup>3</sup> IL (dppz → dppz)	2.90
424	<sup>1</sup> MLCT (Ru <sub>172</sub> → 2TAP <sub>177</sub> )	0.0028		<b>2.93</b>
423			<sup>3</sup> MLCT (Ru → 2TAP)	2.93
413			<sup>3</sup> MLCT (Ru → 2TAP)	3.00
411	<sup>1</sup> LLCT (dppz <sub>172</sub> → 2TAP <sub>178</sub> )	0.0154		<b>3.01</b>
410			<sup>3</sup> MLCT (Ru → 2TAP)	3.02
406			<sup>3</sup> LLCT (TAP → 2TAP)	3.06
406	<sup>1</sup> LLCT (dppz <sub>173</sub> → 2TAP <sub>178</sub> )	0.0211		<b>3.06</b>
401	<sup>1</sup> LLCT (dppz <sub>173</sub> → 2TAP <sub>177</sub> )	0.0978		<b>3.09</b>
400			<sup>3</sup> MLCT (Ru → 2TAP)	3.10
400	<sup>1</sup> MLCT (Ru <sub>169</sub> → 2TAP <sub>175</sub> )	0.0074		<b>3.10</b>
396			<sup>3</sup> MC (Ru → Ru)	<b>3.13</b>
394	<sup>1</sup> MLCT (Ru → dppz)	0.0027		3.15
393			<sup>3</sup> MC (Ru → Ru)	3.15
392			<sup>3</sup> MLCT (Ru → 2TAP)	3.17
391	<sup>1</sup> MLCT (Ru → dppz)	0.0005		3.17
390	<sup>1</sup> MLCT (Ru → dppz)	0.0047		3.18
389		0.0003		3.19
386	<sup>1</sup> MLCT (Ru <sub>169</sub> → 2TAP <sub>176</sub> )	0.0268		<b>3.21</b>
384			<sup>3</sup> IL (TAP → 2TAP)	3.23
383	<sup>1</sup> LLCT (dppz <sub>170</sub> → 2TAP <sub>178</sub> )	0.0237		<b>3.24</b>
382	<sup>1</sup> IL (dppz <sub>173</sub> → dppz <sub>175</sub> )	0.1779		<b>3.24</b>
381			<sup>3</sup> IL (TAP → 2TAP)	3.25
380			<sup>3</sup> MLCT (Ru → dppz)	3.27
372	<sup>1</sup> IL (dppz <sub>170</sub> → dppz <sub>176</sub> )	0.0632		<b>3.33</b>
370			<sup>3</sup> MLCT (Ru → dppz)	3.36

368			<sup>3</sup> MC	(Ru → Ru)	3.37
367			<sup>3</sup> MLCT	(Ru → dppz)	3.38
366	<sup>1</sup> MLCT	(Ru → dppz)	0.0016		3.38
366			<sup>3</sup> MLCT	(Ru → 2TAP)	3.39
364	<sup>1</sup> MLCT	(Ru <sub>169</sub> → 2TAP <sub>177</sub> )	0.0121		3.41
364			<sup>3</sup> MLCT	(Ru → 2TAP)	3.41
362	<sup>1</sup> MLCT	(Ru <sub>169</sub> → 2TAP <sub>178</sub> )	0.0457		3.43
360					3.44
358			<sup>3</sup> LLCT	(dppz → 2TAP)	3.46
358	<sup>1</sup> LLCT	(dppz → 2TAP)	0.0007		3.46
358			<sup>3</sup> MC	(Ru → Ru)	3.47
356			<sup>3</sup> MC	(Ru → Ru)	3.48
347			<sup>3</sup> MC	(Ru → Ru)	3.57
342	<sup>1</sup> MLCT	(Ru → dppz)	0.0004		3.63
335			<sup>3</sup> MLCT	(Ru → dppz)	3.70
334			<sup>3</sup> MLCT	(Ru → dppz)	3.71
332	<sup>1</sup> MLCT	(Ru → dppz)	0.0006		3.74
331	<sup>1</sup> MLCT	(Ru → 2TAP)	0.0007		3.75
325			<sup>3</sup> MLCT	(Ru → dppz)	3.81
324			<sup>3</sup> LLCT	(dppz → 2TAP)	3.82
324	<sup>1</sup> IL	(dppz → dppz)	0.1892		3.83
321	<sup>1</sup> LLCT	(dppz → 2TAP)	0.0066		3.86
319			<sup>3</sup> LLCT	(dppz → 2TAP)	3.89
318	<sup>1</sup> IL	(dppz <sub>173</sub> → dppz <sub>181</sub> )	0.0173		3.90
316	<sup>1</sup> LLCT	(dppz → 2TAP)	0.0126		3.92
316			<sup>3</sup> MLCT	(Ru → dppz)	3.92
316	<sup>1</sup> LLCT	(dppz <sub>168</sub> → 2TAP <sub>176</sub> )	0.0176		3.93
314	<sup>1</sup> MLCT	(Ru → dppz)	0.0007		3.95
313			<sup>3</sup> IL	(TAP → 2TAP)	3.97
311	<sup>1</sup> IL	(TAP <sub>166</sub> → 2TAP <sub>176</sub> )	0.0255		3.99
310			<sup>3</sup> MLCT	(Ru → dppz)	4.01
309			<sup>3</sup> MLCT	(Ru → dppz)	4.01
306	<sup>1</sup> MLCT	(Ru <sub>170</sub> → dppz <sub>181</sub> )	0.0760		4.06
305	<sup>1</sup> MLCT	(Ru <sub>169</sub> → dppz <sub>180</sub> )	0.5373		4.07

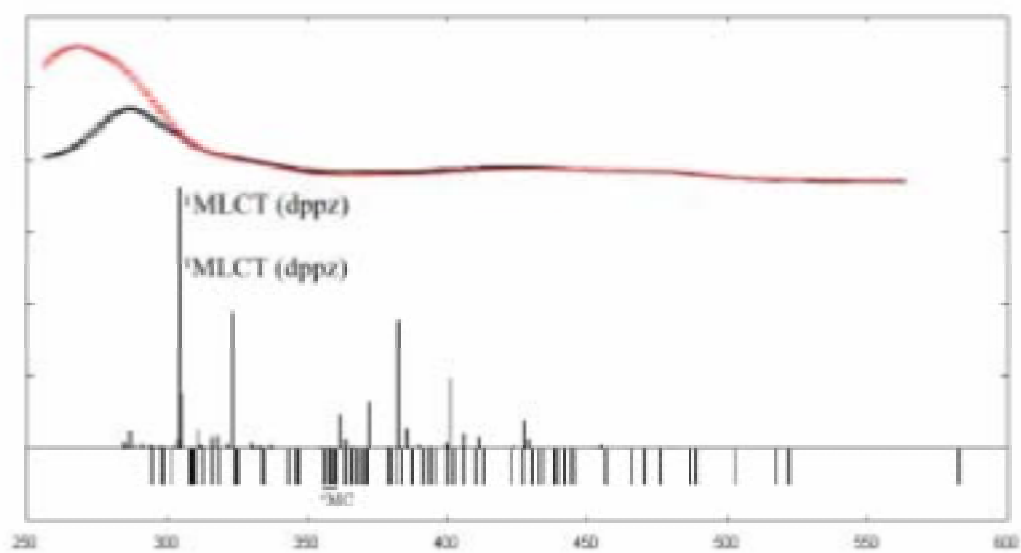


Fig. 2.12 [Ru(TAP)<sub>2</sub>dppz]<sup>2+</sup> theoretical spectra in vacuum by TD-DFT.



Table 2.6 [Ru(phen)<sub>2</sub>dppz]<sup>2+</sup> excited states in vacuum by TD-DFT (cf. Fig.2.13).

nm	Singlets		<i>f</i>	Triplets		eV
508				<sup>3</sup> MLCT	(Ru → 2phen)	2.44
503				<sup>3</sup> MLCT	(Ru → 2phen)	2.47
492				<sup>3</sup> MLCT	(Ru → 2phen)	2.52
478				<sup>3</sup> MLCT	(Ru → 2phen)	2.59
474				<sup>3</sup> MLCT	(Ru → dppz)	2.62
464				<sup>3</sup> MLCT	(Ru → dppz)	2.67
462	<sup>1</sup> MLCT	(Ru → 2phen)	0.0006			2.68
461	<sup>1</sup> MLCT	(Ru → 2phen)	0.0001			2.69
455				<sup>3</sup> MLCT	(Ru → 2phen)	2.72
454				<sup>3</sup> IL	(dppz → dppz)	2.73
451				<sup>3</sup> MLCT	(Ru → 2phen)	2.75
446	<sup>1</sup> MLCT	(Ru → dppz)	0.0001			2.78
436	<sup>1</sup> MLCT	(Ru → 2phen)	0.0014			2.84
436				<sup>3</sup> MLCT	(Ru → 2phen)	2.85
436				<sup>3</sup> MLCT	(Ru → 2phen)	2.85
435	<sup>1</sup> MLCT	(Ru → 2phen)	0.0104			2.85
432				<sup>3</sup> MLCT	(Ru → dppz)	2.87
427				<sup>3</sup> IL	(dppz → dppz)	2.90
425				<sup>3</sup> MLCT	(Ru → 2phen)	2.92
423	<sup>1</sup> MLCT	(Ru → 2phen)	0.0386			2.93
419	<sup>1</sup> MLCT	(Ru → 2phen)	0.0174			2.96
417				<sup>3</sup> IL	(dppz → dppz)	2.98
416	<sup>1</sup> MLCT	(Ru → dppz)	0.0316			2.98
414				<sup>3</sup> MLCT	(Ru → 2phen)	2.99
411	<sup>1</sup> MLCT	(Ru → dppz)	0.1747			<b>3.02</b>
411	<sup>1</sup> IL	(dppz → dppz)	0.0132			3.02
402	<sup>1</sup> MLCT	(Ru → 2phen)	0.0397			3.09
399				<sup>3</sup> MLCT	(Ru → 2phen)	3.11
398				<sup>3</sup> MC	(Ru → Ru)	3.12
398				<sup>3</sup> MC	(Ru → Ru)	3.12
394				<sup>3</sup> MLCT	(Ru → 2phen)	3.15
393	<sup>1</sup> LLCT	(dppz → 2phen)	0.0006			3.16
392	<sup>1</sup> MLCT	(Ru → 2phen)	0.0726			3.17
391	<sup>1</sup> MLCT	(Ru → 2phen)	0.0192			3.17
385	<sup>1</sup> MLCT	(Ru → 2phen)	0.0063			3.22
380				<sup>3</sup> MLCT	(Ru → dppz)	3.26
380	<sup>1</sup> MLCT	(Ru → 2phen)	0.0184			3.26
378	<sup>1</sup> MLCT	(Ru → 2phen)	0.0460			3.28
374				<sup>3</sup> MC	(Ru → Ru)	3.32
371				<sup>3</sup> MC	(Ru → Ru)	3.34
365				<sup>3</sup> MLCT	(Ru → dppz)	3.40
365				<sup>3</sup> MLCT	(Ru → 2phen)	3.40
364	<sup>1</sup> MLCT	(Ru → 2phen)	0.0167			3.40
363	<sup>1</sup> MLCT	(Ru → dppz)	0.0005			3.42
363				<sup>3</sup> LLCT	(dppz → 2phen)	3.42

362	<sup>1</sup> LLCT	(dppz → 2phen)	0		3.42
361				<sup>3</sup> MC (Ru → Ru)	3.44
360				<sup>3</sup> MC (Ru → Ru)	3.44
353				<sup>3</sup> MC (Ru → Ru)	3.51
350	<sup>1</sup> MLCT	(Ru → 2phen)	0.0002		3.54
348				<sup>3</sup> MLCT (Ru → 2phen)	3.56
347				<sup>3</sup> IL (dppz → dppz)	3.58
346				<sup>3</sup> IL (dppz → dppz)	3.59
344				<sup>3</sup> IL (2phen → 2phen)	3.61
343	<sup>1</sup> IL	(dppz → dppz)	0		3.61
343				<sup>3</sup> IL (2phen → 2phen)	3.62
342	<sup>1</sup> LLCT	(dppz → 2phen)	0.0037		3.62
342	<sup>1</sup> MLCT	(Ru → 2phen)	0.0217		3.62
340	<sup>1</sup> MLCT	(Ru → 2phen)	0.0355		3.65
337				<sup>3</sup> LLCT (dppz → 2phen)	3.68
336				<sup>3</sup> LLCT (dppz → 2phen)	3.69
332	<sup>1</sup> LLCT	(dppz → 2phen)	0.0025		3.74
322				<sup>3</sup> LLCT (dppz → 2phen)	3.85
320	<sup>1</sup> LLCT	(dppz → 2phen)	0.0020		3.88
319				<sup>3</sup> LLCT (dppz → 2phen)	3.88
316	<sup>1</sup> LLCT	(dppz → 2phen)	0.0197		3.93
316				<sup>3</sup> IL (dppz → dppz)	3.93
315				<sup>3</sup> LLCT (dppz → 2phen)	3.93
312				<sup>3</sup> LLCT (dppz → 2phen)	3.98
311	<sup>1</sup> LLCT	(dppz → 2phen)	0.0016		3.98
308				<sup>3</sup> LLCT (dppz → 2phen)	4.03
304	<sup>1</sup> LLCT	(dppz → 2phen)	0.0102		4.08
<b>304</b>	<b><sup>1</sup>IL</b>	<b>(dppz → dppz)</b>	<b>0.8771</b>		<b>4.08</b>
302				<sup>3</sup> LLCT (dppz → 2phen)	4.10
301				<sup>3</sup> MLCT (Ru → 2phen)	4.12
296				<sup>3</sup> IL (2phen → 2phen)	4.19
295				<sup>3</sup> MLCT (Ru → 2phen)	4.20
290				<sup>3</sup> MLCT (Ru → 2phen)	4.27
290				<sup>3</sup> IL (dppz → dppz)	4.27
290	<sup>1</sup> MLCT	(Ru → 2phen)	0.0004		4.28
288	<sup>1</sup> MLCT	(Ru → 2phen)	0.0007		4.31
287	<sup>1</sup> MLCT	(Ru → 2phen)	0.0156		4.32
286	<sup>1</sup> MLCT	(Ru → 2phen)	0.0092		4.34
285				<sup>3</sup> MLCT (Ru → 2phen)	4.34
284				<sup>3</sup> MLCT (Ru → 2phen)	4.37
283	<sup>1</sup> MLCT	(Ru → 2phen)	0.0002		4.37
281				<sup>3</sup> MLCT (Ru → 2phen)	4.42
280				<sup>3</sup> MLCT (Ru → 2phen)	4.43
276	<sup>1</sup> MLCT	(Ru → 2phen)	0.0047		4.49
270	<sup>1</sup> MLCT	(Ru → 2phen)	0.0045		4.59

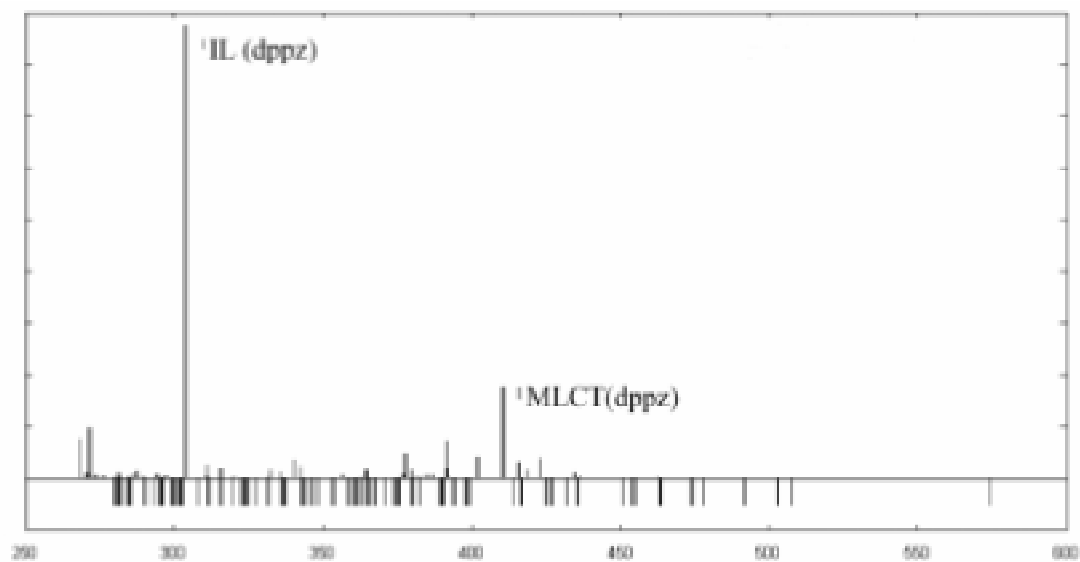


Fig. 2.13  $[\text{Ru}(\text{phen})_2\text{dppz}]^{2+}$  theoretical spectra in vacuum by TD-DFT.

Table 2.7  $[\text{Ru}(\text{TAP})_2\text{dppz}]^{2+}$  excited states by TD-DFT with solvent PCM correction ( $\text{CH}_3\text{CN}$ ). (cf. Fig. 2.14).

Nm	Singlets	$f$	Triplets	eV
550			<sup>3</sup> MLCT (Ru→dppz)	2.25
442			<sup>3</sup> MLCT (Ru→dppz)	2.80
439			<sup>3</sup> LLCT (dppz→2TAP)	2.83
438			<sup>3</sup> IL (dppz→dppz)	2.83
431	<sup>1</sup> LLCT (dppz <sub>171</sub> →2TAP <sub>175</sub> )	0.0438		2.88
429			<sup>3</sup> LLCT (dppz→2TAP)	2.89
425			<sup>3</sup> MLCT (Ru→dppz)	2.92
421			<sup>3</sup> IL (dppz→dppz)	2.95
416	<sup>1</sup> LLCT (dppz <sub>174</sub> →2TAP <sub>178</sub> )	0.0710		2.98
413			<sup>3</sup> LLCT (dppz→2TAP)	3.01
408	<sup>1</sup> LLCT (dppz→2TAP)	0.0375		3.04
407			<sup>3</sup> LLCT (dppz→2TAP)	3.04
403	<sup>1</sup> IL (dppz <sub>174</sub> →dppz <sub>179</sub> )	0.0522		3.07
402	<sup>1</sup> LLCT (dppz→2TAP)	0.0866		3.08
390			<sup>3</sup> MLCT (Ru→2TAP)	3.18
<b>388</b>	<b><sup>1</sup>IL (dppz<sub>173</sub>→dppz<sub>179</sub>)</b>	<b>0.3077</b>		<b>3.19</b>
388	<sup>1</sup> MLCT (Ru <sub>172</sub> →2TAP <sub>175</sub> )	0.0008		3.20
378	<sup>1</sup> MLCT (Ru <sub>169</sub> →dppz <sub>179</sub> )	0.0023		3.28
377	<sup>1</sup> MLCT (Ru <sub>172</sub> →2TAP <sub>176</sub> )	0.0008		3.29
376			<sup>3</sup> MLCT (Ru→2TAP)	3.29
376	<sup>1</sup> MLCT (Ru <sub>172</sub> →dppz <sub>179</sub> )	0.0195		3.30
375			<sup>3</sup> MLCT (Ru→dppz)	3.31
368			<sup>3</sup> MLCT (Ru→dppz)	3.37
361			<sup>3</sup> MLCT (Ru→2TAP)	3.44
361	<sup>1</sup> MLCT (Ru→dppz)	0.0008		3.44
360			<sup>3</sup> MLCT (Ru→2TAP)	3.45
359	<sup>1</sup> MLCT (Ru→dppz)	0.0006		3.45
350			<sup>3</sup> MLCT (Ru→dppz)	3.54
347			<sup>3</sup> MLCT (Ru→2TAP)	3.57
344	<sup>1</sup> MLCT (Ru→2TAP)	0.0239		3.60
341	<sup>1</sup> MLCT (Ru→dppz)	0.0079		3.63
339			<sup>3</sup> MLCT (Ru→2TAP)	3.66
338	<sup>1</sup> MLCT (Ru→2TAP)	0.0048		3.67
336	<sup>1</sup> MLCT (Ru→dppz)	0.0267		3.69
334			(2TAP→dppz)	3.71
333			<sup>3</sup> MLCT (Ru→dppz)	3.73
331			<sup>3</sup> MLCT (Ru→2TAP)	3.75
331	<sup>1</sup> MLCT (Ru→2TAP)	0.0001		3.75
328	<sup>1</sup> LLCT (dppz→dppz)	0.0503		3.77
324			<sup>3</sup> MLCT (Ru→2TAP)	3.83
324	<sup>1</sup> MLCT (Ru→2TAP)	0.0044		3.83
323			<sup>3</sup> MLCT (Ru→2TAP)	3.84
322			<sup>3</sup> MLCT (Ru→2TAP)	3.85
322	<sup>1</sup> MLCT (Ru→2TAP)	0.0089		3.85

321	<sup>1</sup> LLCT	(dppz→dppz)	0.0206			3.86
321				<sup>3</sup> MLCT	(Ru→2TAP)	3.87
318				<sup>3</sup> IL	(dppz→dppz)	3.90
316	<sup>1</sup> IL	(dppz→dppz)	0.0272			3.92
315				<sup>3</sup> MLCT	(Ru→dppz)	3.94
314				<sup>3</sup> MLCT	(Ru→dppz)	3.95
311				<sup>3</sup> MLCT	(Ru→dppz)	3.98
310				<sup>3</sup> MLCT	(Ru→2TAP)	4.00
310				<sup>3</sup> MLCT	(Ru→2TAP)	4.00
309	<sup>1</sup> MLCT	(Ru→dppz)	0.0002			4.01
309	<sup>1</sup> MLCT	(Ru→dppz)	0.0138			4.01
296	<sup>1</sup> MLCT	(Ru <sub>172</sub> →dppz <sub>181</sub> )	1.1346			<b>4.19</b>
282	<sup>1</sup> MLCT	(Ru→dppz)	0.0338			4.39

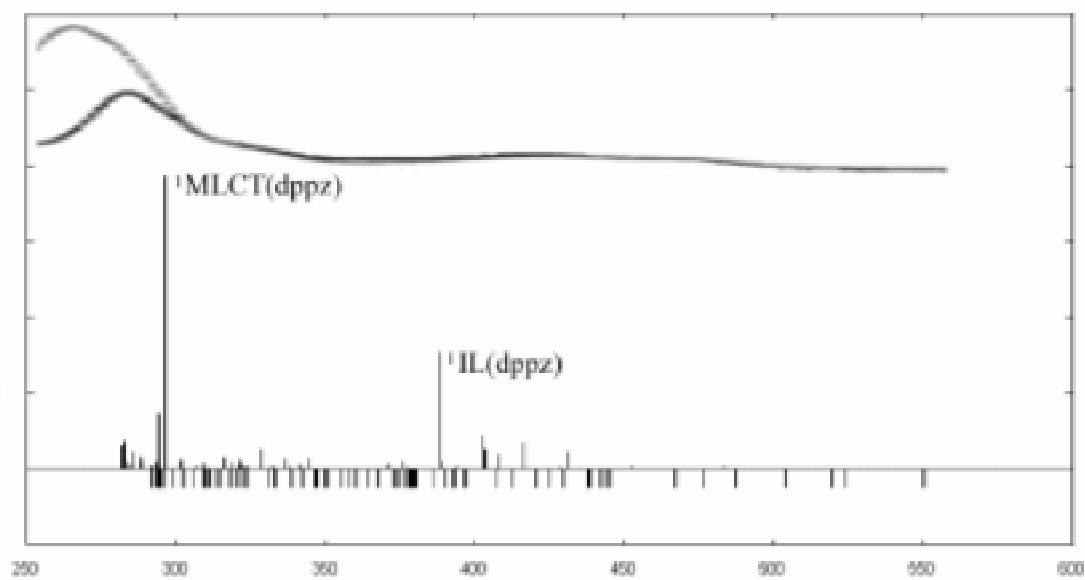


Fig. 2.14 [Ru(TAP)<sub>2</sub>dppz]<sup>2+</sup> theoretical spectra by TD-DFT using the solvent effect of CH<sub>3</sub>CN.

Table 2.8  $[\text{Ru}(\text{TAP})_2\text{dppz}]^{2+}$  excited states by TD-DFT with solvent PCM correction ( $\text{H}_2\text{O}$ ) (cf. Fig. 2.15).

nm	Singlets		$f$	Triplets	eV
548				<sup>3</sup> MLCT (Ru→dppz)	2.26
505				<sup>3</sup> LLCT (dppz→2TAP)	2.45
489				<sup>3</sup> LLCT (dppz→2TAP)	2.54
468				<sup>3</sup> LLCT (dppz→2TAP)	2.65
453	<sup>1</sup> LLCT	(dppz→2TAP)	0.0048		2.73
441				<sup>3</sup> MLCT (Ru→dppz)	2.81
433	<sup>1</sup> LLCT	(dppz <sub>171</sub> →2TAP <sub>175</sub> )	0.0377		2.86
426				<sup>3</sup> MLCT (Ru→dppz)	2.91
421				<sup>3</sup> IL (dppz→dppz)	2.95
418	<sup>1</sup> LLCT	(dppz <sub>174</sub> →2TAP <sub>177</sub> )	0.0750		2.96
414				<sup>3</sup> LLCT (dppz→2TAP)	2.99
409	<sup>1</sup> LLCT	(dppz <sub>173</sub> →2TAP <sub>177</sub> )	0.0364		3.03
409				<sup>3</sup> LLCT (dppz→2TAP)	3.03
406	<sup>1</sup> IL	(dppz <sub>174</sub> →dppz <sub>179</sub> )	0.0124		3.05
<b>404</b>	<b><sup>1</sup>LLCT</b>	<b>(dppz<sub>173</sub>→2TAP<sub>178</sub>)</b>	<b>0.1282</b>		<b>3.07</b>
394				<sup>3</sup> LLCT (dppz→2TAP)	3.15
393				<sup>3</sup> IL (dppz→dppz)	3.16
391	<sup>1</sup> LLCT	(dppz→2TAP)	0.0193		3.17
<b>390</b>	<b><sup>1</sup>IL</b>	<b>(dppz<sub>173</sub>→dppz<sub>179</sub>)</b>	<b>0.2859</b>		<b>3.18</b>
390				<sup>3</sup> IL (dppz→dppz)	3.18
385				<sup>3</sup> MLCT (Ru→2TAP)	3.22
381				<sup>3</sup> MLCT (Ru→2TAP)	3.25
381	<sup>1</sup> MLCT	(Ru→2TAP)	0.0009		3.26
377	<sup>1</sup> IL	(dppz→dppz)	0.0055		3.28
373	<sup>1</sup> MLCT	(Ru→dppz)	0.0138		3.33
372				<sup>3</sup> MLCT (Ru→dppz)	3.33
372	<sup>1</sup> MLCT	(Ru→dppz)	0.0086		3.33
371				<sup>3</sup> MLCT (Ru→dppz)	3.34
370	<sup>1</sup> MLCT	(Ru→2TAP)	0.0024		3.35
370				<sup>3</sup> MLCT (Ru→2TAP)	3.35
355				<sup>3</sup> MLCT (Ru→2TAP)	3.49
355	<sup>1</sup> MLCT	(Ru→2TAP)	0.0005		3.49
354	<sup>1</sup> MLCT	(Ru→2TAP)	0.0004		3.51
354				<sup>3</sup> MLCT (Ru→2TAP)	3.51
349	<sup>1</sup> IL	(dppz→dppz)	0.0059		3.55
348				<sup>3</sup> MLCT (Ru→dppz)	3.56
344				<sup>3</sup> IL (dppz→dppz)	3.60
343				<sup>3</sup> MLCT (Ru→2TAP)	3.62
342	<sup>1</sup> MLCT	(Ru→2TAP)	0.0133		3.63
337	<sup>1</sup> MLCT	(Ru→dppz)	0.0053		3.67
336	<sup>1</sup> MLCT	(Ru <sub>170</sub> →dppz <sub>170</sub> )	0.0439		3.69
334				<sup>3</sup> MLCT (Ru→2TAP)	3.71
334	<sup>1</sup> MLCT	(Ru→2TAP)	0.0025		3.71
331				<sup>3</sup> MLCT (Ru→dppz)	3.75

330	<sup>1</sup> IL	(dppz <sub>174</sub> →dppz <sub>181</sub> )	0.0453		3.76
326	<sup>1</sup> MLCT	(Ru→2TAP)	0.0014		3.81
325				<sup>3</sup> MLCT (Ru→2TAP)	3.81
325	<sup>1</sup> MLCT	(Ru→2TAP)	0.0014		3.82
321				<sup>3</sup> MLCT (Ru→2TAP)	3.86
321	<sup>1</sup> MLCT	(Ru→2TAP)	0.0018		3.87
320	<sup>1</sup> MLCT	(Ru→2TAP)	0.0209		3.88
320				<sup>3</sup> MLCT (Ru→2TAP)	3.88
318	<sup>1</sup> IL	(2TAP→2TAP)	0.0023		3.90
318				<sup>3</sup> MLCT (Ru→dppz)	3.90
317	<sup>1</sup> IL	(dppz→dppz)	0.0073		3.91
317				<sup>3</sup> MLCT (Ru→dppz)	3.91
317	<sup>1</sup> MLCT	(Ru→2TAP)	0.0009		3.92
312				<sup>3</sup> MLCT (Ru→2TAP)	3.97
309				<sup>3</sup> LLCT (dppz→2TAP)	4.01
308				<sup>3</sup> IL (2TAP→2TAP)	4.03
308	<sup>1</sup> LLCT	(dppz→2TAP)	0.0011		4.03
308	<sup>1</sup> IL	(2TAP→2TAP)	0.0018		4.03
306				<sup>3</sup> MLCT (Ru→dppz)	4.05
306	<sup>1</sup> MLCT	(Ru→dppz)	0.0047		4.05
306				<sup>3</sup> MLCT (Ru→2TAP)	4.06
305	<sup>1</sup> IL	(2TAP→2TAP)	0.0011		4.06
305				<sup>3</sup> MLCT (Ru→2TAP)	4.06
305	<sup>1</sup> MLCT	(Ru→2TAP)	0.0006		4.06
300				<sup>3</sup> IL (2TAP→2TAP)	4.13
300	<sup>1</sup> IL	(2TAP→2TAP)	0.0189		4.14
298	<sup>1</sup> MLCT	(Ru→dppz)	0.0002		4.17
295				<sup>3</sup> IL (2TAP→2TAP)	4.21
294	<sup>1</sup> MLCT	(Ru <sub>172</sub> →dppz <sub>181</sub> )	0.5807		<b>4.21</b>
293	<sup>1</sup> MLCT	(Ru <sub>172</sub> →dppz <sub>181</sub> )	0.7330		<b>4.23</b>
292				<sup>3</sup> IL (2TAP→2TAP)	4.24
292	<sup>1</sup> IL	(2TAP→2TAP)	0.0031		4.25
292				<sup>3</sup> IL (2TAP→2TAP)	4.25
292	<sup>1</sup> IL	(2TAP→2TAP)	0.0065		4.25
289	<sup>1</sup> LLCT	(dppz→2TAP)	0.0260		4.29
282	<sup>1</sup> MLCT	(Ru→dppz)	0.0464		4.40



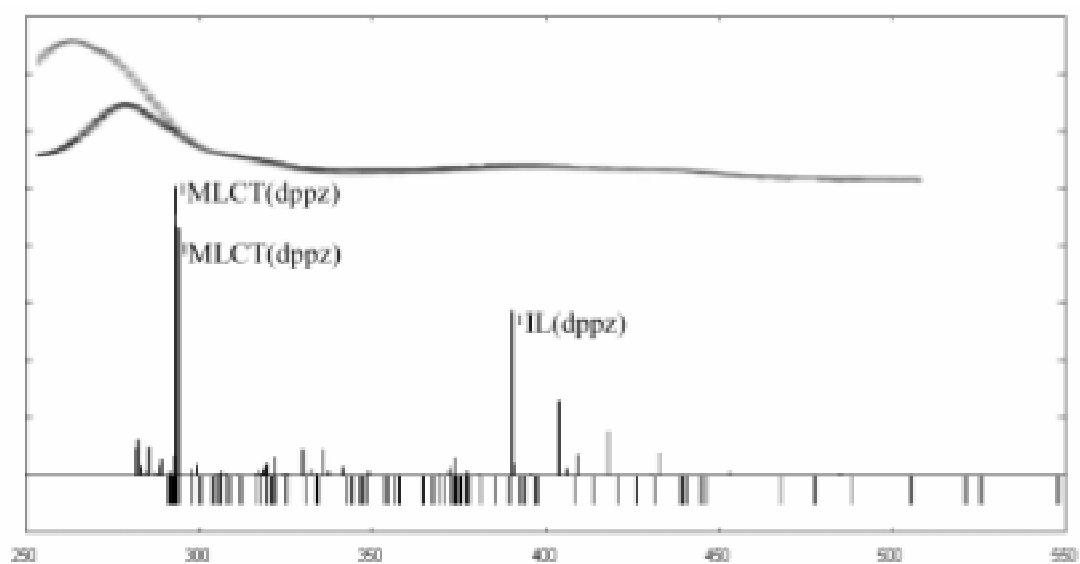


Fig. 2.15 [Ru(TAP)<sub>2</sub>dppz]<sup>2+</sup> theoretical spectra by TD-DFT using the solvent effect of H<sub>2</sub>O.

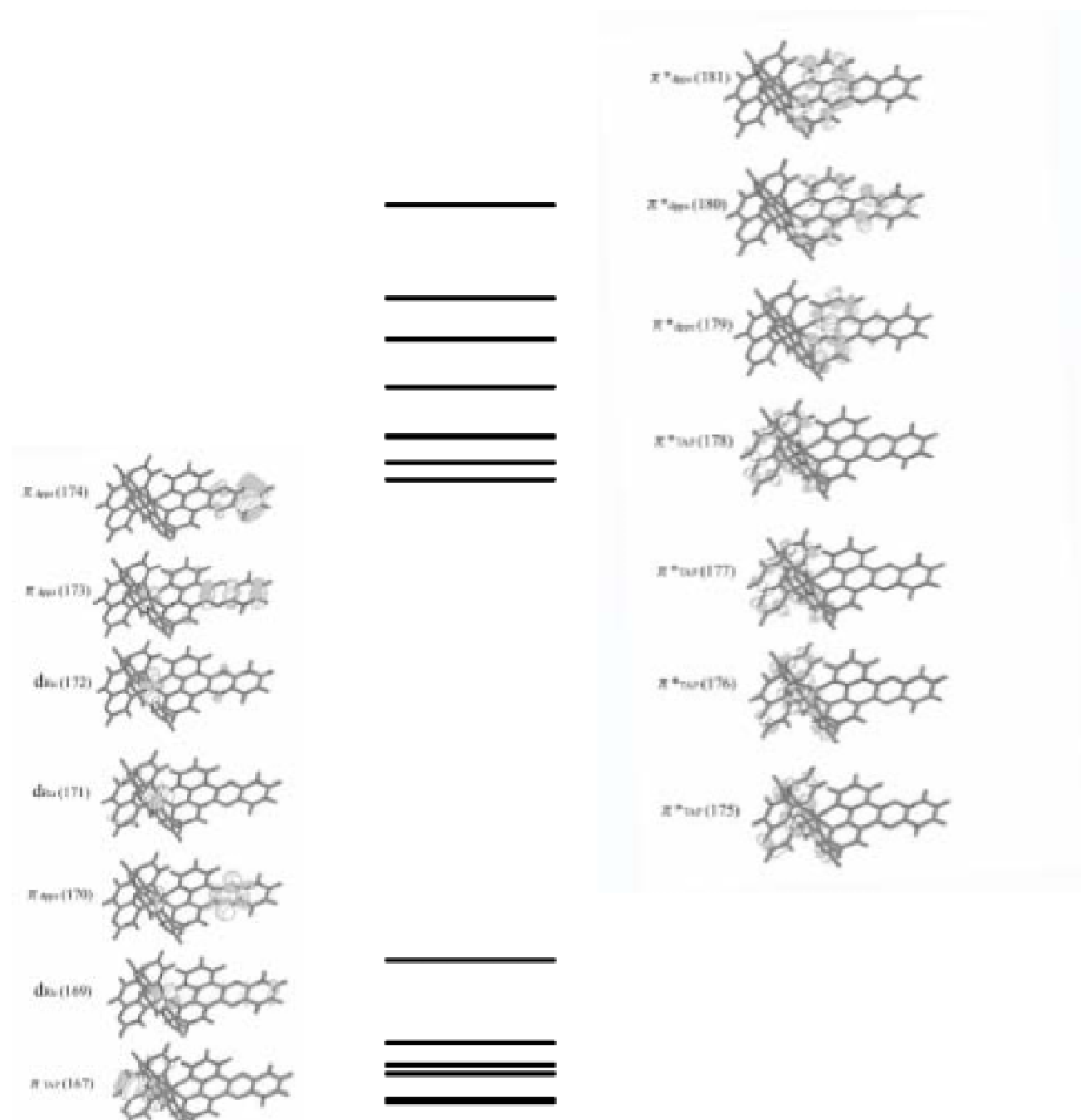


Fig. 2.16 Stereographs of the HOMOs and the LUMOs of  $[\text{Ru}(\text{TAP})_2\text{dppz}]^{2+}$ .

For theoretical spectroscopy, although TD-DFT is a formally exact method, one introduces errors by using approximated xc-functionals. Charge transfer excitations between spatially separated entities will be underestimated by standard xc-correlation potentials inappropriate for long range interactions. That is to say hypersensitivity of the TD-DFT to the xc-correlation potential at long range will have dramatic effects on the determination of charge transfer excited states. In Kohn-Sham theory, the effective potential is unique and decreases too rapidly as a function of  $1/R$ . It doesn't equal at the asymptote to the electrostatic potential of a simple positive charge that an electron should feel at long range [99, 100]. In the results reported above it could have some effect on the LLCT states corresponding to long-range excitations, namely from the tap or phen ligands to the dpppz. For instance in the case of  $[\text{Ru}(\text{TAP})_2\text{phen}]^{2+}$  the transition energies to the low-lying LLCT states calculated between 455 nm and 401 nm could be underestimated. But according to the rather good agreement between the experimental features and theoretical results we don't think that this defect of TD-DFT would affect the present analysis.

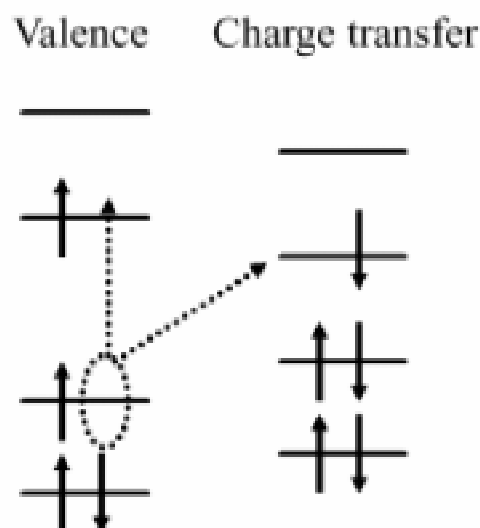
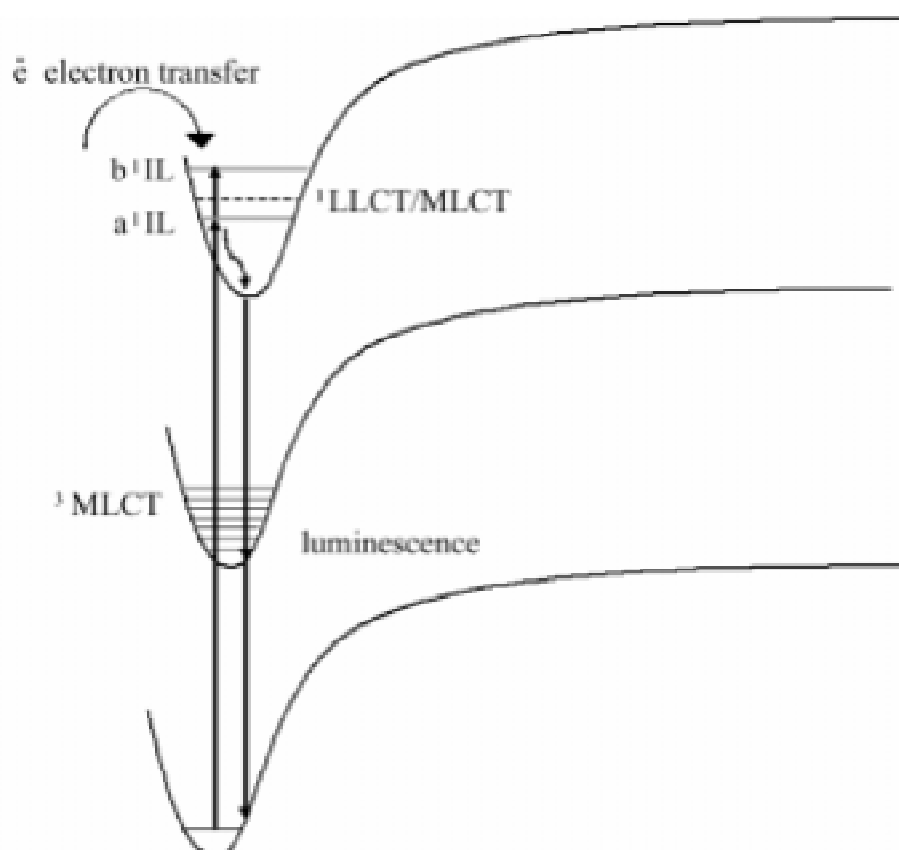


Fig 2.16 This is the schematic sketch of a typical valence-excited state, in which the transition occurs on one of the individual molecules. They located on the same molecule as compared to a charge transfer excited state. An electron transferred from orbital left to right. When right and left molecules are spatially separated from each other.

### 2.2.3 Light switch mechanism

From the analysis of the theoretical spectra reported in the previous section and from experimental data we can propose the following mechanism describing the photophysics of the complexes under investigation:

**[Ru(TAP)<sub>2</sub>dppz]<sup>2+</sup>**: after absorption at 400 nm the two low-lying <sup>1</sup>IL ( $\pi_{\text{dppz}} \rightarrow \pi^*_{\text{dppz}}$ ) states calculated at 406 nm/390 nm (H<sub>2</sub>O) and 403 nm /388 nm (CH<sub>3</sub>CN) are populated. These states which delocalize electron density from the external side of the dppz ligand to its ruthenium side are available for two deactivation processes: i) intersystem crossing to the low-lying triplet excited states until the lowest one corresponding to  $d_{\text{Ru}} \rightarrow \pi^*_{\text{dppz}}$  calculated at 548 nm (H<sub>2</sub>O) and 550 nm (CH<sub>3</sub>CN); ii) electron transfer from surrounding entity to the external site of dppz deficient in electron (Scheme 1).



Scheme 1

From the low lying  $^3\text{MLCT}$  luminescence, typical process for this class of compound. However in the presence of biological environment the second process may be favoured due to the presence of guanine. This is consistent with the formation of  $[\text{Ru}(\text{TAP})_2\text{dppz}]^+$  postulated by recent experiments [76, 81] obtained via electron transfer from the guanine to the dppz ligand.

**$[\text{Ru}(\text{phen})_2\text{dppz}]^{2+}$** : after absorption at 400 nm the only available absorbing states are the MLCT states corresponding mainly to charge transfer from Ru to phen or to dppz with weak oscillator strengths. From this MLCT states the only efficient process should be intersystem crossing to the corresponding low-lying  $^3\text{MLCT}$  states. From the lowest  $^3\text{MLCT}$  efficient luminescence could be observed [98] the quantum yield of which will depend on the experimental conditions. For instance moderately strong emission from a MLCT species is easily observed in acetonitrile, while in water no significant emission is apparent. Acetonitrile/water solvent mixtures are intermediate in shoulder [147]. The question of MLCT luminescence quenching by water has been extensively discussed in the literature.

The key of the photophysical properties of these Ru(II) complexes seems to be the presence of the  $^1\text{IL}$  localized on the dppz ligand in the lowest part of the absorption spectrum. Obviously the energetics of this state may be influenced by the environment effects at the dppz side, in particular the presence of water molecules creating hydrogen bonds could modify completely the mechanism proposed above. We have to specify that the hydrogen bonds are not taken into account in the simple PCM model. Consequently we cannot discuss further these effects.

## 2.3 $[Ru(TAP)_2dppz]^{2+}$ intercalates to DNA

### 2.3.1 Structure of $[Ru(TAP)_2dppz]^{2+}$ and 6CG

Fig 2. 17 illustrated the perpendicular moleds proposed for the intercalation of the  $[Ru(TAP)_2dppz]^{2+}$  in DNA.

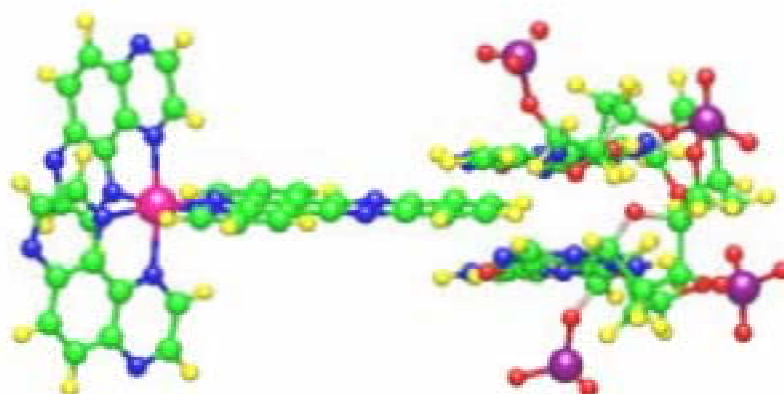


Fig. 2.17  $[Ru(TAP)_2dppz]^{2+}$  intercalates to 2CG of Z-DNA.

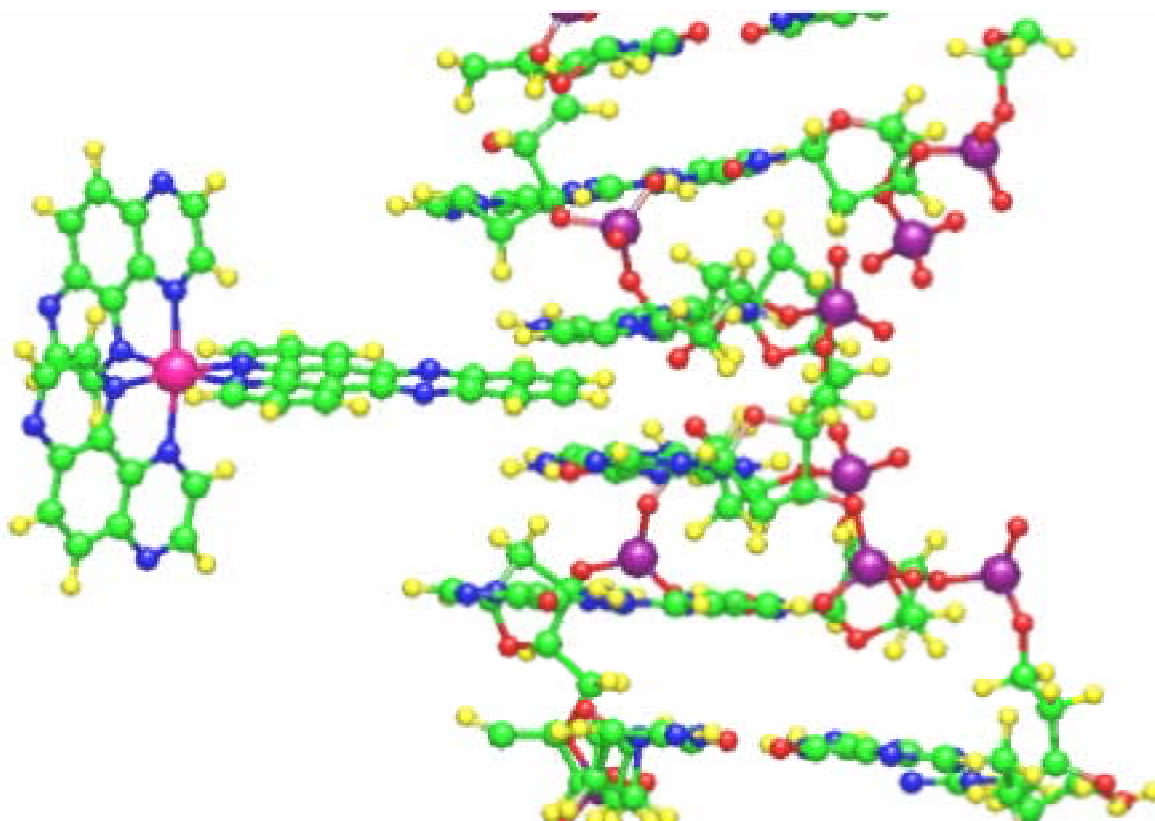


Fig. 2.18  $[Ru(TAP)_2dppz]^{2+}$  intercalates to 6CG of Z-DNA.

To confirm the electron transfer trends between metal complexes binding to DNA, the intercalative depth was defined as the distance from Ru(II) atom to nucleobase N3 atom (Fig. 2.3). Simultaneously, on the basis of the initial position of intercalative ligand, where the head part just contacts with base-pairs, the intercalative depth was partitioned into minor groove region and base-pairs region (Fig. 2.3). Next, the potential energy of intercalative process was plotted according to the above results (Fig. 2.19). The best relative position of  $[\text{Ru}(\text{TAP})_2\text{dppz}]^{2+}$  complex bound to the Z-DNA was found by analyzing the potential curve.

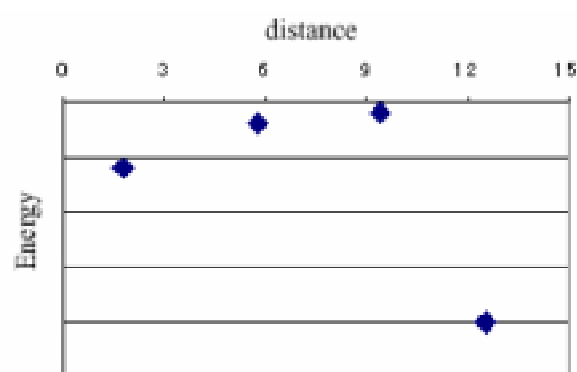


Fig. 2.19 Potential energy for the  $[\text{Ru}(\text{TAP})_2\text{dppz}]^{2+}$  binding Z-DNA.

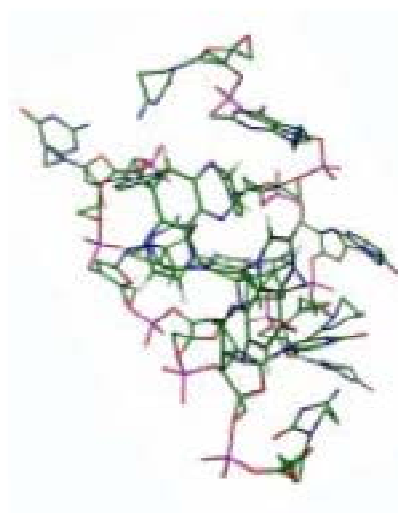


Fig. 2.20(a)

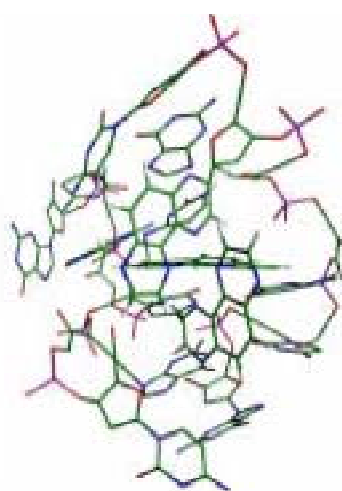


Fig. 2.20(b)

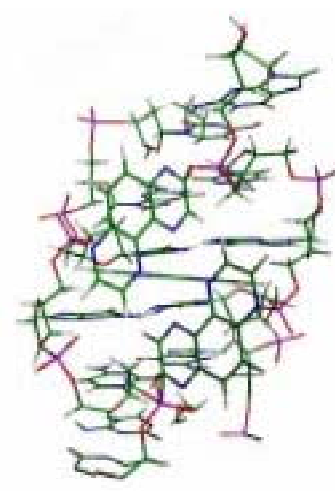


Fig. 2.20(c)

Fig. 2.20 Geometry optimization by MM (a), QM/MM (b), and QM/MM of single point calculation(c).

Fig 2.21 and the Table 2.4 show the structure of  $[\text{Ru}(\text{TAP})_2\text{dppz}]^{2+}$  intercalating to the 6CG. At the MM level optimization, its biological system is crumpled; it becomes to make spherical shape at QM/MM level, the distance of Ru-N is extended by single point calculation.

Table 2.4 Comparison between the Ru-N distance of intercalating Z-DNA obtained with MM, QM/MM.

	Ru-N1 (Å)	Ru-N2 (Å)	Ru-N3 (Å)	Ru-N4 (Å)	Ru-N5 (Å)	Ru-N6 (Å)
MM	2.13	2.13	2.13	2.12	2.12	2.11
QM/MM	1.74	1.67	1.85	1.62	1.67	1.63
QM/MM (Single point)	2.11	2.11	2.10	2.12	2.11	2.11

Clearly QM/MM geometry optimization converges to underestimated Ru-N bond distances. It points to the limit of the method for this large system. However QM/MM single point calculation leads to Ru-N bond distances very close to those of the Ru complex in vacuum or solution. MM optimized bond distances seem to be reasonable. Future work should also investigate intercalative geometry generated by chirality.

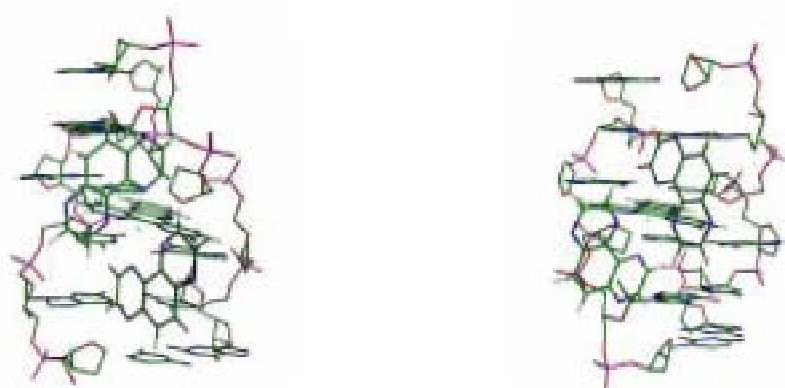


Fig. 2.21 The chiral  $[\text{Ru}(\text{TAP})_2\text{dppz}]^{2+}$  complex intercalates to DNA.



## 2.4 Conclusion

The structure and electronic properties of  $[\text{Ru}(\text{TAP})_2\text{dppz}]^{2+}$  and  $[\text{Ru}(\text{phen})_2\text{dppz}]^{2+}$  complexes used as luminescent probes by intercalation in DNA have been studied by means of Density Functional Theory. The geometries of the title complexes have been optimized and validated by calculation performed on  $[\text{Ru}(\text{TAP})_3]^{2+}$  the experimental structure of which is available. A tentative investigation of the solvent effects on the structural properties has failed due to convergence problems which should be solved in a futur work. Preliminary QM/MM calculations modeling the TAP complex intercalated in six nucleotides have been reported.

The absorption spectra of the two complexes have been analysed on the basis of TD-DFT calculations. Whereas the lowest part of the electronic absorption spectroscopy of the TAP complex is characterized by a variety of excited states such as IL, MLCT or LLCT, the spectrum of the phen system is made of MLCT states. In particular it has been shown that absorption at about 400 nm (experimental wavelength) will populate the low-lying IL states of  $[\text{Ru}(\text{TAP})_2\text{dppz}]^{2+}$  with delocalization of the electronic density from the outside side of the dppz intercalated ligand to the inside site (nearby the Ru atom). This electronic delocalization should favorize the electron transfer process from a nearby electron donor such as the guanine leading to the formation of the G<sup>•+</sup> radical cation. In contrast absorption towards the low-lying MLCT states of  $[\text{Ru}(\text{phen})_2\text{dppz}]^{2+}$  opens the route to efficient luminescent processes via intersystem crossing to the lowest <sup>3</sup>MLCT states. The competition between these two processes is the key point of the mechanism of "light switch" which characterizes this class of molecules, the efficiency of which depends strongly on the experimental conditions and of the surrounding ligands. This could be explained by the influence on these external parameters on the relative position of the IL and MLCT states in the absorption spectra. When low-lying IL states are present in the electronic absorption spectrum the luminescence could be quenched leading to an efficient electron transfer process. In contrast the presence of MLCT states will increase the luminescence efficiency. Further work should be oriented towards the study of environment effects on the proposed mechanism.

## **Chapter 3**

Highly correlated methods on Ag(I) halides



**S**ilver halides crystals are used as conventional light sensors in photography due to their highly efficient photoinduced electron transfer process occurring from the valence state to the conduction bands of the crystal. Silver halides can also be used as liquid semiconductors [101] or solid electrolytes [102]. Because their well known technological applicability, there has been a large number of studies devoted to the understanding of these compounds; however, the description of their electronic structure and spectroscopy has resulted to be not trivial. The calculation of the band-gap of the solid structures requires fully relativistic pseudopotentials corrected for self-interaction and relaxation effects. The isolated systems AgX (X=F,Cl,Br and I) are not much easier to describe. The interatomic distances, vibrational frequencies and binding energies of these compounds in the electronic ground state have been studied [116,117]. The potential energy curves for the electronic excited states and spectroscopic properties have been recently investigated by Ramírez-Solís and Daudey [118-120] and by Guichemere *et al.* using highly correlated multiconfigurational and multireference techniques. The difficulty in these calculations is related with the description of relativistic effects and the proper inclusion of dynamical electronic correlation with enough flexible basis sets. The silver halides are characterized by the presence of Ag 4d orbitals in near degeneracy with the p-valence orbitals of the halogen atoms. In the electronic ground state the ionic character of the AgX decreases when going down in the periodic table, from F to I. As expected, AgF is the most ionic and AgI the most covalent of the silver halides, with AgCl and AgBr accordingly in between. The description of the electronic excited states on the other hand, involves a non-straightforward elucidation of the ionic/covalent character of the corresponding states which leads to avoided crossings between the ionic and covalent configurations. The emission of AgF was observed for the first time in 1937 by Mulliken around 280 nm [103]. Lower energy bands (311-343 nm) were vibrationally assigned by Joshi and

Sharma [104], and the rotational structure was determined by Clements and Barrow [105]. The dipole moment (6.22 D) for the ground state and the rotational constants were also obtained from microwave spectroscopy [106]. The calculation of the ground and lowest singlet and triplet  $^1\Sigma^+$ ,  $^1\Pi$  and  $^1\Delta$  excited states have been tackled for the first time by Ramírez-Solis *et al.* [107, 108] using self-consistent-field plus perturbational second order multireference Møller-Plesset configuration interaction (SCF+CIPSI) and complete-active space SCF plus second order perturbation theory (CASSCF+CASPT2) calculations, and later by Guichemere *et al.* [103] employing Multireference CI with singles and double excitations (MRCISD) and equation-of-motion coupled-cluster with single and double excitations (EOM-CCSD) techniques. These calculations revealed that it is extraordinarily hard to obtain reliable electronic excitations and therefore it is very difficult to assign correctly the nature of the experimental bands [109].

For the AgCl and AgBr several rotational studies have been done. The absorption of AgBr has been observed already [110] in 1927, but the spectrum of AgCl and AgI together with that of AgBr, has been examined using modern fluorescence excitation and mass resolved excitation spectroscopies only in 1998 by Stueber *et al.* [111]. The electronic ground state and low lying  $^1\Sigma^+$ ,  $^1\Pi$  and  $^1\Delta$  excited states of AgCl and AgI have been theoretically predicted. As in the case of AgF, it is shown that the large amount of valence electrons of the Ag and halogen atoms which must be correlated in the CASSCF calculations, together with the heavy mixing of covalent and ionic configurations for Ag and halogen atoms make the calculations very demanding.

In contrast to AgX molecules, silver dihalides, AgX<sub>2</sub> or AgXY, serve as a paradigm of transition metals bonded to two—equal or different—halogen atoms. Under light irradiation it will be interesting to know in which halogen atom the charge transfer occurs, which one will be more efficiently dissociated under different wavelengths and how the potential energy surfaces look like in comparison to those of silver monohalides. In passing we note that silver mixed dihalides crystals have been grown as waveguides for transmitting mid-infrared-IR radiation [112]. Opposite to AgX, silver dihalides are open-shell systems in the electronic ground state, and only the anionic species presents a closed-shell configuration. As a result, the molecular complexes are difficult to synthesize and no spectroscopic constants have ever been measured; furthermore, up to our knowledge, no theoretical results have been published. In this paper we will treat for the first time the description of the ground and low-lying excited states of a mixed silver dihalide, exemplarily [AgClBr] and its anionic counterpart [AgClBr]<sup>-</sup>. Challenging enough, already the ground state doublet configuration is not trivially described using mono-determinantal quantum chemical methods. As it will be discussed later, our benchmark calculations show that, very large basis sets as well as

static and dynamical correlation are needed to correctly account for the delicate balance of the electron charges in both halogen atoms, and the bonding of the Ag atom with the two halogen atoms.

In addition this study has possibility to apply for as a model to perform the silver(I) complex with the DNA base pair. Also the availability of host materials that are highly transparent in developing solid-state lasers that operate in the mid-IR spectral range. Meanwhile the silver halide crystals can be attractive candidates for extending laser emission to the mid-IR range which properties of silver halide crystals such as AgClBr are highly transparent in the near-IR and mid-IR ranges and have desirable mechanical and optical properties. Furthermore considering the redox and Ernst formula, the silver halides synthesis  $\text{AgCl} + \text{Br}^- \rightarrow \text{ClAgBr}$  is difficult to make the linear structure, we hazard the making theoretical structure and molecular predict for this molecule.

## 3.1 Computational Details

### 3.1.1 Geometry Optimization

In the absence of experimental data on the structure of AgClBr and [AgClBr]<sup>-</sup>, we have started our study by optimizing the equilibrium geometries employing *ab initio* Møller-Plesset theory (MP2) and coupled-cluster methods including single, double and perturbative triple (CCSD(T)), as well as density functional theory based on B3LYP. For the silver we employed the MWB relativistic effective core potential (RECP) implemented by Dolg and co-workers [89] which leaves 19 valence electrons and associated valence basis sets within the scheme of contraction (6s5p3d)/[8s7p6d]. For the Cl and Br atoms we employed the Pople basis set 6-311++G(2d) [113 - 116], except noted otherwise. The theoretical study extended to AgF<sub>2</sub> with the same methods. For the F atom we used the basis set 6-311++G(2d). These calculations have been performed with the Gaussian03 program package [3].

### 3.1.2 Single configuration calculations

Using the CCSD(T) systematic Hartree-Fock and B3LYP calculations have been performed to elucidate the open-shell electronic ground state configuration of the AgClBr compound and its bonding properties. For the sake of comparison, the same set of calculations has also been performed in the anion. The single determinant calculations have been carried out with all electrons, relativistic, or non relativistic, ECP (See table 3.1). The ANO-RCC basis sets are generated similarly to the ANO-L basis sets, but they are contracted using the Douglas-Kroll Hamiltonian and, therefore, they include scalar relativistic effects, as well as correlation of semicore electrons[117]. All electron ANO-RCC [17s12p5d4f2g]/(8s7p5d4f2g), [20s17p11d4f2g]/(9s8p6d4f2g), and [14s9p4d3f2g]/(8s7p4d3f2g) basis sets were used for the Cl, Br, and F atoms, respectively. For the Ag atom the all electron as well different RECPs, and non-relativistic (NR) ECPs have been used, with different contraction schemes for the valence electrons. In the all electron basis sets for Ag, we have employed the ANO-RCC basis set [118], contracted as [21s18p13d6f4g2h]/(10s9p8d6f4g2h) and the ANO-DK3 [119], contracted as [23s19p12d]/(6s5p4d). The ANO-DK3 basis set includes scalar relativistic effects using a third-order Douglas-Kroll approximation. Among the RECPs, we have used two different pseudopotential methods: the RECP of

Hay and Wadt (LANL2DZ) [120] and that of Dolg21 (MWB); as well as two model potential frozen core approximations of the type Ab Initio Model Potentials (AIMP): the Cowan-Griffin-based scalar relativistic CG-AIMP [121] and the no-pair Douglas-Kroll NP-AIMP [122] methods. All the RECPs used 19 valence electrons, except for the CG-AIMP which uses 17 valence electrons. The corresponding schemes of contraction are  $[5s,6p,4d]/(3s,3p,2d)$  for the 19e-LANL2DZ,  $[8s,7p,6d]/(6s,5p,3d)$  for the 19e-MWB, [131],  $[11s,8p,7d]/(1s,2p,2d)$  and the uncontracted  $[11s,8p,7d]/(3s,3p,4d)$  for the 17e-CG-AIMP and  $[11s,8p,7d,3f]/(5s,4p,4d,1f)$  in the 19e-NP-AIMP RECP. Additionally, we have also employed the non-relativistic core AIMP, which describes 17 electrons in the valence (17e-NR-AIMP) with the schemes of contraction,  $[11s,8p,7d]/(1s,2p,2d)$  and the uncontracted  $[11s,8p,7d]/(3s,3p,4d)$ . All the employed basis sets and ECPs are summarized in Table 3.1, together with the number of primitives and contracted basis functions that they involve for  $[\text{AgClBr}]$  and  $[\text{AgClBr}]^-$ . In the case of  $[\text{AgF}_2]$  and  $[\text{AgF}_2]^-$  the number of primitives and contracted basis functions used 440 and 353 respectively. These calculations have been performed using the MOLCAS 6.0 quantum chemistry software [4].

Assuming  $C_s$  symmetry for a collinear geometry (vide infra) and using as a reflection plane the  $yz$  (see Fig. 1), the orbitals  $4d_{z^2}$ ,  $4d_{x^2-y^2}$  and  $4d_{yz}$  of the Ag atom are of  $A'$  symmetry, together with the  $np_y$  and  $np_z$  of the halogen atoms, while the  $4d_{xy}$  and  $4d_{xz}$  of the Ag and the  $np_x$  orbitals of the Br, Cl, and F atoms belong to the  $A''$  irreducible representation. On the following we will use the notation  $4d\sigma$  to indicate the  $\sigma$  bonding orbital between the  $4d_{z^2}$  and  $np_z$  orbitals, and  $4d\pi$  for the  $4d_{yz}$  and  $4d_{xz}$  orbitals. The electronic structure of the anion  $[\text{AgClBr}]^-$  corresponds to the  $^1A'$   $(d_{z^2}/p_z(\text{Cl}))^2 (d_{yz})^2 (d_{x^2-y^2})^2 (p_x(\text{Br})/p_x(\text{Cl}))^2 (p_y(\text{Cl}))^2 (p_z(\text{Br}))^2 (d_{z^2})^2 (d_{xz})^2 (d_{xy})^2 (p_x(\text{Cl}))^2 (p_x(\text{Br}))^2$ , the anion  $[\text{AgF}_2]^-$  is consistent with the  $^1A'$   $(p_z(\text{F})/d_{z^2}/p_z(\text{F}))^2 (p_y(\text{F})/d_{yz}/p_y(\text{F}))^2 (p_x(\text{F})/p_x(\text{F}))^2 (p_x(\text{F})/p_x(\text{F}))^2 (d_{x^2-y^2})^2 (p_y(\text{F})/d_{yz}/p_y(\text{F}))^2 (d_{z^2})^2 (p_x(\text{F})/d_{xz}/p_x(\text{F}))^2 (p_x(\text{F})/p_x(\text{F}))^2 (d_{xy})^2 (p_x(\text{F})/d_{xz}/p_x(\text{F}))^2$ .



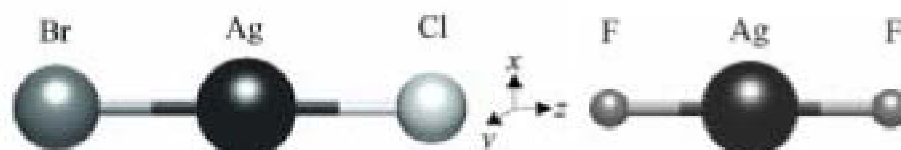


Figure 3.1 Molecular-fixed orientation of AgClBr and AgF<sub>2</sub>.

**Table 3.1.** Basis sets and ECPs used in this work, with their contraction schemes and number of primitives and basis functions for AgClBr.

Basis sets & ECPs	Scheme of contraction	#Primitives	#BF
All electron			
ANO-RCC [118]	(21s18p13d6f4g2h)[10s9p8d6f4g2h]	500	261
ANO-DK3 [119]	(23s19p12d)[6s5p4d]	400	125
ANO-DK3-u [119]	(25s22p12d4f)[11s11p5d4f]	439	181
RECPs			
17e-CG-AIMP [121]	(11s8p7d)[1s2p2d]	366	226
17e-CG-AIMP-u [121]	(11s8p7d)[3s3p4d]	366	241
19e-NP-AIMP [122]	(11s8p7d3f)[5s4p4d1f]	387	253
19e-MWB Dolg [89]	(8s7p6d)[6s5p3d]	355	245
19e-LANL2DZ HW [120]	(5s6p4d)[3s3p2d]	339	231
NRECPs [118]			
17e-NR-AIMP [121]	(11s8p7d)[1s2p2d]	366	226
17e-NR-AIMP-u [121]	(11s8p7d)[3s3p4d]	366	241

### 3.1.3 Multiconfigurational calculations

To elucidate the bonding properties of AgClBr and AgF<sub>2</sub> in the doublet electronic ground state we have performed state-average SA-CASSCF calculations with 7 or 4 roots equally weighted, for A' and A'' symmetry, respectively. The active space comprises all the 21 valence electrons distributed in the 7 A' + 4 A'' occupied orbitals, keeping all other occupied orbitals frozen, i.e. it consists of 7 and 4 configurations, respectively. These calculations, denoted by 7-SA-CASSCF(21,11) and 4-SA-CASSCF(21,11), allow the single electron to be allocated in any of the valence

orbitals. The dynamical correlation was taken into account by multi-state MS-CASPT2 over the 7 or 4 roots, respectively. In contrast to the single determinant HF and DFT approaches, as it will be shown in Section III, this reduced active space is able to describe correctly the bonding of AgClBr because of the inclusion of dynamical correlation. A more proper description (including static correlation) of the electronic correlation would require at least an active space of 21 electrons in  $14 A' + 8 A''$  orbitals. However, a MS-CASPT2/ CASSCF(21,22) is beyond the capabilities of our current computer facilities. Therefore, we have restricted to employ separate active spaces to treat the states of  $A'$  and  $A''$  symmetry. Accordingly, MS-CASPT2/7-SA-CASSCF(13,14) and MS-CASPT2/4-SA-CASSCF(7,8) calculations including ca.  $4 \cdot 10^6$  and  $8 \cdot 10^3$  spin-adapted configurations for the  $A'$  and  $A''$  symmetries, respectively, have been performed.

The calculation of the quartet electronic excited states have also been done independently for the  $A'$  and  $A''$  symmetries, that is at MS-CASPT2/7-SA-CASSCF (13,14) and MS-CASPT2/4-SA-CASSCF(7,8) level of theory, respectively. These set of calculations have been done using the ANO-RCC basis set for all atoms, with the schemes of contraction described in Table I.

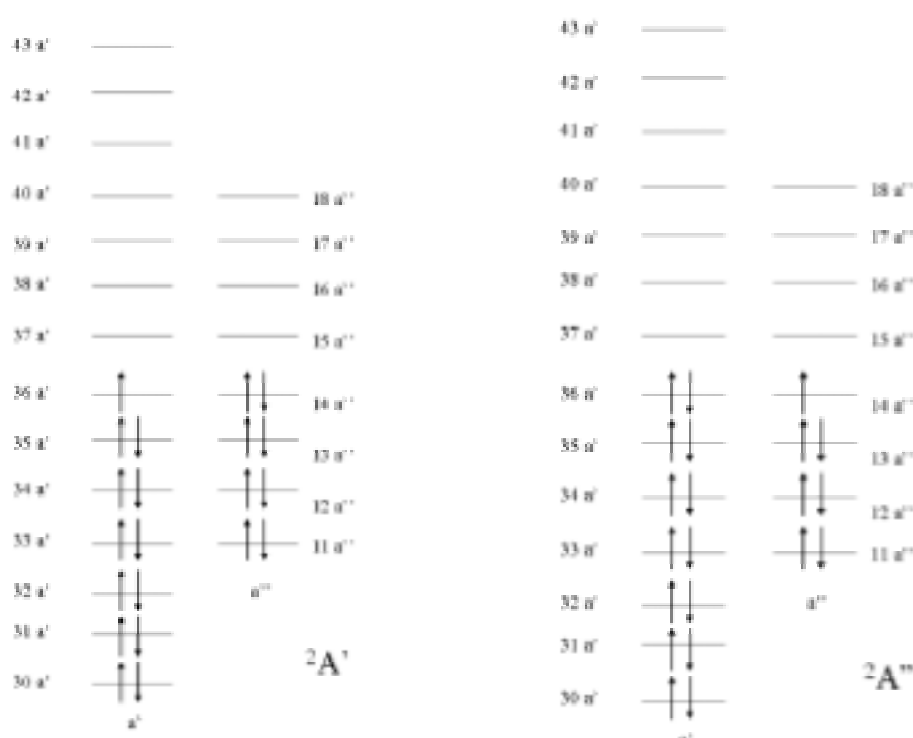


Figure 3.2. The active space of AgClBr which is applied for All electron model. This scheme is applied for AgF<sub>2</sub>.

## 3.2 AgClBr

### 3.2.1 Structures of the metal complexes

The optimization of the AgClBr and [AgClBr]<sup>-</sup> complexes at MP2, CCSD(T) and B3LYP levels of theory resulted in a collinear structure. The nature of the obtained critical point was verified checking that all frequencies are positive. The equilibrium bond lengths at the vibrational potential minimum between the metal and the halogen atoms are collected in Table 3.2, together with the experimental AgX bond distances for reference. As expected, Br—Ag bond lengths are longer than Ag—Cl ones. In comparison with the silver monohalides, the distances in the dihalides are elongated by ca.0.02 Å for the strong Ag—Cl bond and about double for the weak Ag—Br one. The calculated bond distances with the different methods agree reasonably well, especially within the anionic structure and in predicting Ag—Cl distances. The exception is the MP2 value for Br—Ag bond distance in the neutral structure which is overestimated by almost 0.1 Å. In general, the calculation employing RECPs in all atoms overestimates Br—Ag and Ag—Cl values by 0.05 Å in comparison with the values obtained when all electron basis sets are used for the halogen atoms. In view of this overall qualitative agreement, we have chosen the collinear geometry obtained with CCSD(T) for the forthcoming calculations using the molecular-fixed orientation shown in Fig.1. Meanwhile this linear is more stable than co-linear structure in Table 3.2-b.

**Table 3.2.** Equilibrium distances (in Å) of the collinear neutral and anion Cl—Ag—Br at different levels of theory.

$r_{eq}$ (Å)	neutral AgClBr		anion AgClBr <sup>-</sup>	
	Br—AgCl	BrAg—Cl	Br—AgCl	BrAg—Cl
MP2	2.526	2.304	2.505	2.379
CCSD(T)	2.445	2.299	2.526	2.401
B3LYP	2.435	2.309	2.507	2.384
B3LYP/MWB <sup>a</sup>	2.478	2.372	2.541	2.437
exp. <sup>b</sup>	2.393 <sup>c</sup>	2.280 <sup>d</sup>	—	—

<sup>a</sup>Calculation performed using the MWB RECP in all three atoms.

<sup>b</sup>The experimental values are reported for the corresponding AgBr and AgCl diatomics.

<sup>c</sup>[123]

<sup>4</sup>[140]

**Table 3.2-b**

The comparison with linear and co-linear energy at HF level. The degree shows between Br-Ag-Cl.

angle	180	175
Energy (a.u.)	-8377.026013	-8377.021187

### 3.2.2. Electronic ground state

*Single-determinants calculations.* Let us first discuss the results obtained with single-determinant methods. Tables 3.3 and 3.4 show the electronic configurations and Mulliken charges of AgClBr and AgClBr<sup>-</sup> obtained using different basis sets and ECPs, at HF and B3LYP levels of theory, respectively. The first striking fact is that there is no systematic link between the HF and DFT electronic configurations obtained using any basis set. Sometimes the single electron is allocated in the p orbital of the Br atom, others in the Cl atom. Furthermore, sometimes is the p<sub>y</sub> orbital, others the p<sub>x</sub> orbital. This apparent erratic behaviour can be directly mirrored in the charge distributions calculated within the Mulliken approach. We are aware the Mulliken charge partition is as arbitrary as any other but in the present work we solely aim at a qualitative charge distribution picture.

The use of relativistic ANO-RCC predicts both at HF and DFT the single electron to be in the 4p<sub>y</sub> of the Br (analogously in the 4p<sub>x</sub> of the Br—not shown in the Table), which is associated with a strong ionic bond between the Cl and Ag, and a less ionic bond between the Ag and Br. This is a reasonable result in view of the electronegativities of the Cl and Br atoms and the expected single determinant configuration (*vide supra*).

When going from the neutral to the anion, we have a closed-shell structure, i.e. the 4p<sub>y</sub> (or 4p<sub>x</sub>) orbital of the Br atom is filled. Accordingly, one would expect the charge distribution reflecting the fact that the Cl atom recovers some negative charge in comparison to the neutral case. Indeed, the Mulliken charges calculated with the all-electron approaches show an (accidental) symmetric charge distribution between the Cl and Br atoms, both at HF and DFT (see Tables 3.3 and 3.4). The use of ECPs for the Ag atom does not permit to reproduce the delicate balance of the Br and Cl charges. As a consequence, the differences between the different ECPs cannot be easily rationalized. At the HF level the results are consistent with the fact that the Cl atom is more negatively charged than Br atom, maintaining the Ag positive (cf. Table 3.3). Note that the use of AIMP<sub>s</sub> systematically underestimates the positive charge in the Ag atom. This erroneous tendency of AIMP<sub>s</sub> is even more pronounced in the case of the Kohn-Sham orbitals where Ag reverses its charge from positive to negative. The use of uncontracted AIMP significant enhances this erroneous behaviour (cf. Table 3.4) making the Ag atom strongly negative. From this results we deduce that to describe correctly the intimate interplay of bonding and charge distribution in AgClBr one should describe the Ag and the halogen atoms on the same footing in an all electron calculation, that is, e.g. using relativistic ANO-RCC basis sets.

In general, in view of the unsteady results obtained with the single determinant HF and

KS calculations, we now proceed to include static and dynamical correlation using multiconfigurational perturbation methods. The results are collected in Tables 3.6 to 3.9.

### *Multiconfiguration calculations.*

In order to determine the lowest  ${}^2A'$ / ${}^2A''$  degenerate states of AgBrCl MS-CASPT2 calculations have been performed on SA-CASSCF correlating 21 electrons in 11 active orbitals. The results are reported in Table 3.6. The doublet electronic ground state of AgBrCl corresponds to the  ${}^2A'$   $(p_x(\text{Br})/p_x(\text{Cl}))^2(d_{xz}/p_x(\text{Cl}))^2(d_{xy})^2(p_z(\text{Br})/d_{z^2}/p_z(\text{Cl}))^2(d_{x^2-y^2})^2(d_{yz}/p_y(\text{Cl}))^2(p_z(\text{Br})/p_z(\text{Cl}))^2(p_y(\text{Br})/p_y(\text{Cl}))^2(p_z(\text{Br})/d_{z^2}/p_z(\text{Cl}))^2(p_y(\text{Br})/d_{yz}/p_y(\text{Cl}))^1(p_x(\text{Br})/d_{xz}/p_x(\text{Cl}))^2$  calculated at -8377.82061 a.u. nearly degenerate with the  ${}^2A''$  corresponding to the following configuration

$(p_x(\text{Br})/p_x(\text{Cl}))^2(d_{xz}/p_x(\text{Cl}))^2(d_{xy})^2(p_z(\text{Br})/d_{z^2}/p_z(\text{Cl}))^2(d_{x^2-y^2})^2(d_{yz}/p_y(\text{Cl}))^2(p_z(\text{Br})/p_z(\text{Cl}))^2(p_y(\text{Br})/p_y(\text{Cl}))^2(p_z(\text{Br})/d_{z^2}/p_z(\text{Cl}))^2(p_y(\text{Br})/d_{yz}/p_y(\text{Cl}))^2(p_x(\text{Br})/d_{xz}/p_x(\text{Cl}))^1$  calculated at -8377.82242 a.u. The total energies are not strictly the same due to artefacts of the CASSCF calculations performed in  $C_s$  symmetry. MS-CASPT2 calculations based on restricted symmetry blocked CASSCF including non-dynamical correlation effects are reported in Table 3.7. These calculations based on different active spaces in the two symmetries  $A'$  and  $A''$  cannot reproduce the degeneracy. However they converge to the same electronic ground state solution, namely  ${}^2A'$  and  ${}^2A''$  with the electronic configuration described above. The results of the same calculations based on ECP are reported in Tables 3.8 and 3.9. Again the lowest MS-CASPT2 electronic states correspond to the above configurations with one single electron in the  $(p_y(\text{Br})/d_{yz}/p_y(\text{Cl}))^1$  and  $(p_x(\text{Br})/d_{xz}/p_x(\text{Cl}))^1$  molecular orbitals for the nearly degenerate  ${}^2A'$  and  ${}^2A''$  states, respectively.

### 3.2.3. Spectroscopy

Several CASSCF active spaces have been defined for the calculation of the lowest quadroplet states of Ag, Cl, Br. Generated single excitations from the  ${}^2A'$  to  ${}^2A''$  determined previously.  ${}^4A'$  and  ${}^4A''$  have been obtained on the basis of 13 electrons 14 actives, 7 electrons 8 actives and 7 electrons 11 actives orbitals CASSCF space according to the following the scheme.

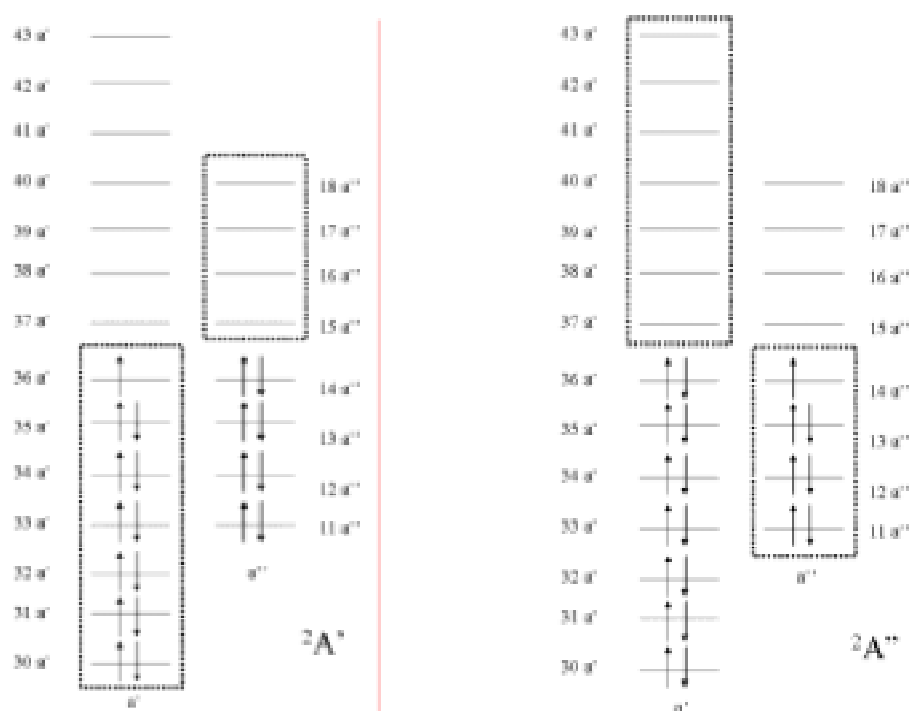


**Table 3.3.** Electronic configurations and Mulliken charges obtained at Hartree-Fock level of theory and different basis sets and ECPs.

Basis sets	Configuration	Mulliken charges		
		Br	Ag	Cl
Neutral AgClBr				
ANO-RCC	$(3p_x, Cl)^2 (4d\pi)^2 (4d\pi)^2 (4d\sigma)^2 (3p_x, Cl)^2 (4p_x, Br)^2 (4p_x, Br)^1$ $(3p_x, Cl)^2 (4d\pi)^2 (4d\pi)^2 (4p_x, Br)^2$	0.16	0.59	-0.75
ANO-DK3	$(4d\sigma)^2 (4d\pi)^2 (4d\pi)^2 (4p_x, Br)^2 (3p_x, Cl)^2 (3p_x, Cl)^2 (4p_x, Br)^1$ $(4d\pi)^2 (4d\pi)^2 (4p_x, Br)^2 (3p_x, Cl)^2$	-0.21	0.66	-0.45
ANO-DK3 -u	$(4d\sigma)^2 (4d\pi)^2 (4d\pi)^2 (4p_x, Br)^2 (3p_x, Cl)^2 (3p_x, Cl)^2 (4p_x, Br)^1$ $(4d\pi)^2 (4d\pi)^2 (4p_x, Br)^2 (3p_x, Cl)^2$	-0.12	0.58	-0.46
17e- CG-AIMP	$(4d\sigma)^2 (4d\pi)^2 (4d\pi)^2 (4p_x, Br)^2 (3p_x, Cl)^2 (3p_x, Cl)^2 (4p_x, Br)^1$ $(4d\pi)^2 (4d\pi)^2 (4p_x, Br)^2 (3p_x, Cl)^2$	0.04	0.37	-0.41
17e- CG-AIMP-u	$(4d\pi)^2 (4d\pi)^2 (4d\sigma)^2 (3p_x, Cl)^2 (4p_x, Br)^2 (4p_x, Br)^2 (3p_x, Cl)^1$ $(4d\pi)^2 (4d\pi)^2 (3p_x, Cl)^2 (4p_x, Br)^2$	-0.39	0.77	-0.38
19e- NP-AIMP	$(4d\pi)^2 (4d\sigma)^2 (4d\pi)^2 (4p_x, Br)^2 (3p_x, Cl)^2 (3p_x, Cl)^2 (4p_x, Br)^1$ $(4d\pi)^2 (4d\pi)^2 (4p_x, Br)^2 (3p_x, Cl)^2$	0.03	0.47	-0.5
19e-MWB	$(3p_x, Cl)^2 (4d\pi)^2 (4d\pi)^2 (d\sigma)^2 (3p_x, Cl)^2 (4p_x, Br)^2 (4p_x, Br)^1$ $(4d\pi)^2 (4d\pi)^2 (3p_x, Cl)^2 (4p_x, Br)^2$	-0.06	1.07	-1.01
19e-LANL2D Z	$(4d\pi)^2 (d\sigma Cl)^2 (4d\pi)^2 (3p_x, Cl)^2 (4p_x, Br)^2 (4p_x, Br)^2 (3p_x, Cl)^1$ $(4d\pi)^2 (4d\pi)^2 (3p_x, Cl)^2 (4p_x, Br)^2$	-0.53	1.12	-0.59
17e- NR-AIMP	$(4d\sigma)^2 (4d\pi)^2 (4d\pi)^2 (4p_x, Br)^2 (3p_x, Cl)^2 (3p_x, Cl)^2 (4p_x, Br)^1$ $(4d\pi)^2 (4d\pi)^2 (4p_x, Br)^2 (3p_x, Cl)^2$	0.07	0.36	-0.43
17e- NR-AIMP-u	$(4d\pi)^2 (4d\pi)^2 (4d\sigma)^2 (3p_x, Cl)^2 (4p_x, Br)^2 (4p_x, Br)^2 (3p_x, Cl)^1$ $(4d\pi)^2 (4d\pi)^2 (3p_x, Cl)^2 (4p_x, Br)^2$	-0.35	0.71	-0.36
Anion AgClBr <sup>-</sup>				
ANO-RCC	$(4d\sigma)^2 (4d\pi)^2 (4d\pi)^2 (3p_x, Cl)^2 (3p_x, Cl)^2 (4p_x, Br)^2 (4p_x, Br)^2$ $(4d\pi)^2 (4d\pi)^2 (3p_x, Cl)^2 (4p_x, Br)^2$	-0.77	0.56	-0.78
ANO-DK3	$(4d\sigma)^2 (4d\pi)^2 (4d\pi)^2 (3p_x, Cl)^2 (3p_x, Cl)^2 (4p_x, Br)^2 (4p_x, Br)^2$ $(4d\pi)^2 (4d\pi)^2 (3p_x, Cl)^2 (4p_x, Br)^2$	-0.81	0.61	-0.81
ANO-DK3 -u	$(4d\sigma)^2 (4d\pi)^2 (4d\pi)^2 (3p_x, Cl)^2 (3p_x, Cl)^2 (4p_x, Br)^2 (4p_x, Br)^2$ $(4d\pi)^2 (4d\pi)^2 (3p_x, Cl)^2 (4p_x, Br)^2$	-0.77	0.54	-0.76
17e- CG-AIMP	$(4d\sigma)^2 (4d\pi)^2 (4d\pi)^2 (3p_x, Cl)^2 (3p_x, Cl)^2 (4p_x, Br)^2 (4p_x, Br)^2$ $(4d\pi)^2 (4d\pi)^2 (3p_x, Cl)^2 (4p_x, Br)^2$	-0.61	0.32	-0.71
17e- CG-AIMP-u	$(4d\sigma)^2 (4d\pi)^2 (4d\pi)^2 (3p_x, Cl)^2 (3p_x, Cl)^2 (4p_x, Br)^2 (4p_x, Br)^2$ $(4d\pi)^2 (4d\pi)^2 (3p_x, Cl)^2 (4p_x, Br)^2$	-0.57	0.41	-0.74
19e- NP-AIMP	$(4d\sigma)^2 (4d\pi)^2 (4d\pi)^2 (3p_x, Cl)^2 (3p_x, Cl)^2 (4p_x, Br)^2 (4p_x, Br)^2$ $(4d\pi)^2 (4d\pi)^2 (3p_x, Cl)^2 (4p_x, Br)^2$	-0.66	0.38	-0.72
19e-MWB	$(4d\sigma)^2 (4d\pi)^2 (4d\pi)^2 (3p_x, Cl)^2 (3p_x, Cl)^2 (4p_x, Br)^2 (4p_x, Br)^2$ $(4d\pi)^2 (4d\pi)^2 (3p_x, Cl)^2 (4p_x, Br)^2$	-0.71	0.93	-1.21
19e-LANL2D Z	$(4d\sigma)^2 (4d\pi)^2 (4d\pi)^2 (3p_x, Cl)^2 (3p_x, Cl)^2 (4p_x, Br)^2 (4p_x, Br)^2$ $(4d\pi)^2 (4d\pi)^2 (3p_x, Cl)^2 (4p_x, Br)^2$	-0.79	0.73	-0.94
17e- NR-AIMP	$(4d\sigma)^2 (4d\pi)^2 (4d\pi)^2 (3p_x, Cl)^2 (3p_x, Cl)^2 (4p_x, Br)^2 (4p_x, Br)^2$ $(4d\pi)^2 (4d\pi)^2 (3p_x, Cl)^2 (4p_x, Br)^2$	-0.57	0.31	-0.74
17e- NR-AIMP-u	$(4d\sigma)^2 (4d\pi)^2 (4d\pi)^2 (3p_x, Cl)^2 (3p_x, Cl)^2 (4p_x, Br)^2 (4p_x, Br)^2$ $(4d\pi)^2 (4d\pi)^2 (3p_x, Cl)^2 (4p_x, Br)^2$	-0.62	0.34	-0.72



**Table 3.4.** Electronic configurations and Mulliken charges obtained using B3LYP and different basis sets and ECPs.

Basis sets	Configuration	Mulliken charges		
		Br	Ag	Cl
Neutral AgClBr				
ANO-RCC	$(3p_z, Cl)^2 (4d\pi)^2 (4d\pi)^2 (4d\sigma)^2 (3p_z, Cl)^2 (4p_z, Br)^2 (4p_y, Br)^1$ $(3p_z, Cl)^2 (4d\pi)^2 (4d\pi)^2 (4p_z, Br)^2$	0.32	0.55	-0.87
ANO-DK3	$(4d\sigma)^2 (4d\pi)^2 (4d\pi)^2 (4p_z, Br)^2 (4p_y, Br)^2 (4p_z, Br)^2 (3p_z, Cl)^1$ $(4d\pi)^2 (4d\pi)^2 (4p_z, Br)^2 (3p_z, Cl)^2$	-0.75	0.41	0.34
ANO-DK3 -u	$(4d\sigma)^2 (4d\pi)^2 (4d\pi)^2 (3p_z, Cl)^2 (3p_z, Cl)^2 (4p_z, Br)^2 (4p_y, Br)^1$ $(4d\pi)^2 (4d\pi)^2 (4p_z, Br)^2 (3p_z, Cl)^2$	0.24	0.34	-0.58
17e- CG-AIMP	$(3p_z, Cl)^2 (3p_z, Cl)^2 (4d\pi)^2 (4d\pi)^2 (4d\sigma)^2 (4p_z, Br)^2 (4p_y, Br)^1$ $(3p_z, Cl)^2 (4d\pi)^2 (4d\pi)^2 (4p_z, Br)^2$	0.85	-0.13	-0.71
17e- CG-AIMP-u	$(3p_z, Cl)^2 (3p_z, Cl)^2 (4d\pi)^2 (4d\pi)^2 (4d\sigma)^2 (4p_z, Br)^2 (4p_y, Br)^1$ $(3p_z, Cl)^2 (4d\pi)^2 (4d\pi)^2 (4p_z, Br)^2$	0.85	-0.28	-0.56
19e- NP-AIMP	$(4d\sigma)^2 (4d\pi)^2 (4d\pi)^2 (3p_z, Cl)^2 (3p_z, Cl)^2 (4p_z, Br)^2 (4p_y, Br)^1$ $(4d\pi)^2 (4d\pi)^2 (3p_z, Cl)^2 (4p_z, Br)^2$	0.52	0.04	-0.56
19e-MWB	$(4d\pi)^2 (4d\sigma)^2 (4d\pi)^2 (3p_z, Cl)^2 (3p_z, Cl)^2 (4p_z, Br)^2 (4p_y, Br)^1$ $(4d\pi)^2 (4d\pi)^2 (3p_z, Cl)^2 (4p_z, Br)^2$	0.58	0.41	-0.99
19e-LANL2D Z	$(4p_z, Br)^2 (4d\pi)^2 (4d\pi)^2 (4p_z, Br)^2 (4p_z, Br)^2 (3p_z, Cl)^2 (3p_z, Cl)^1$ $(4d\pi)^2 (4d\pi)^2 (4p_z, Br)^2 (3p_z, Cl)^2$	-0.83	0.71	0.11
17e- NR-AIMP	$(4d\sigma)^2 (4d\pi)^2 (4d\pi)^2 (4p_z, Br)^2 (4p_y, Br)^2 (3p_z, Cl)^2 (3p_z, Cl)^1$ $(4d\pi)^2 (4d\pi)^2 (4p_z, Br)^2 (3p_z, Cl)^2$	-0.23	0.03	0.20
17e- NR-AIMP-u	$(3p_z, Cl)^2 (4d\pi)^2 (4d\pi)^2 (3p_z, Cl)^2 (4d\sigma)^2 (4p_z, Br)^2 (4p_y, Br)^1$ $(3p_z, Cl)^2 (4d\pi)^2 (4d\pi)^2 (4p_z, Br)^2$	0.89	-0.32	-0.57
Anion AgClBr <sup>-</sup>				
ANO-RCC	$(4d\sigma)^2 (4d\pi)^2 (4d\pi)^2 (3p_z, Cl)^2 (3p_z, Cl)^2 (4p_z, Br)^2 (4p_y, Br)^2$ $(4d\pi)^2 (4d\pi)^2 (3p_z, Cl)^2 (4p_z, Br)^2$	-0.68	0.36	-0.68
ANO-DK3	$(4d\sigma)^2 (4d\pi)^2 (4d\pi)^2 (3p_z, Cl)^2 (3p_z, Cl)^2 (4p_z, Br)^2 (4p_y, Br)^2$ $(4d\pi)^2 (4d\pi)^2 (3p_z, Cl)^2 (4p_z, Br)^2$	-0.78	0.56	-0.78
ANO-DK3 -u	$(4d\sigma)^2 (4d\pi)^2 (4d\pi)^2 (3p_z, Cl)^2 (3p_z, Cl)^2 (4p_z, Br)^2 (4p_y, Br)^2$ $(4d\pi)^2 (4d\pi)^2 (3p_z, Cl)^2 (4p_z, Br)^2$	-0.67	0.33	-0.66
17e- CG-AIMP	$(4d\sigma)^2 (4d\pi)^2 (4d\pi)^2 (3p_z, Cl)^2 (3p_z, Cl)^2 (4p_z, Br)^2 (4p_y, Br)^2$ $(4d\pi)^2 (4d\pi)^2 (3p_z, Cl)^2 (4p_z, Br)^2$	-0.37	-0.04	-0.59
17e- CG-AIMP-u	$(4d\sigma)^2 (4d\pi)^2 (4d\pi)^2 (4p_z, Br)^2 (3p_z, Cl)^2 (3p_z, Cl)^2 (4p_z, Br)^2$ $(4d\pi)^2 (4d\pi)^2 (3p_z, Cl)^2 (4p_z, Br)^2$	-0.32	-0.25	-0.43
19e- NP-AIMP	$(4d\sigma)^2 (4d\pi)^2 (4d\pi)^2 (4p_z, Br)^2 (3p_z, Cl)^2 (3p_z, Cl)^2 (4p_z, Br)^2$ $(4d\pi)^2 (4d\pi)^2 (3p_z, Cl)^2 (4p_z, Br)^2$	-0.45	0.03	-0.58
19e-MWB	$(4d\sigma)^2 (4d\pi)^2 (4d\pi)^2 (4p_z, Br)^2 (3p_z, Cl)^2 (3p_z, Cl)^2 (4p_z, Br)^2$ $(4d\pi)^2 (4d\pi)^2 (3p_z, Cl)^2 (4p_z, Br)^2$	-0.52	0.63	-1.11
19e-LANL2D Z	$(4d\sigma)^2 (4d\pi)^2 (4d\pi)^2 (3p_z, Cl)^2 (3p_z, Cl)^2 (4p_z, Br)^2 (4p_y, Br)^2$ $(4d\pi)^2 (4d\pi)^2 (3p_z, Cl)^2 (4p_z, Br)^2$	-0.70	0.63	-0.93
17e- NR-AIMP	$(4d\sigma)^2 (4d\pi)^2 (4d\pi)^2 (3p_z, Cl)^2 (4p_z, Br)^2 (3p_z, Cl)^2 (4p_z, Br)^2$ $(4d\pi)^2 (4d\pi)^2 (3p_z, Cl)^2 (4p_z, Br)^2$	-0.32	-0.04	-0.64
17e- NR-AIMP-u	$(4d\sigma)^2 (4d\pi)^2 (4d\pi)^2 (3p_z, Cl)^2 (3p_z, Cl)^2 (4p_z, Br)^2 (4p_y, Br)^2$ $(4d\pi)^2 (4d\pi)^2 (3p_z, Cl)^2 (4p_z, Br)^2$	-0.27	-0.31	-0.42

Table 3.5-a. Coefficient of single occupied on each basis set and SCF energy at HF level.

Basis sets & ECPs				SCF Energy
	Br	Ag	Cl	
All electron				
ANO-RCC	$p_y$ (0.88)			-8377.026013
ANO-DK3	$p_y$ (-0.78)	$d_{yz}$ (-0.43)	$p_y$ (0.55)	-8377.071715
ANO-DK3-u	$p_y$ (-0.88)	$d_{yz}$ (-0.14)	$p_y$ (-0.14)	-8377.061955
RECPs				
17e-CG-AIMP	$p_y$ (0.88)	$d_{yz}$ (-0.30)	$p_y$ (0.46)	-3121.656973
17e-CG-AIMP-u	$p_z$ (0.28)	$d_{z2}$ (-0.6)	$p_z$ (-0.48)	-3121.663797
19e-NP-AIMP	$p_z$ (0.84)	$d_{z2}$ (-0.47)	$p_z$ (-0.3)	-3156.546232
19e-MWB Dolg	$p_y$ (-0.77)	$d_{yz}$ (0.35)	$p_y$ (0.59)	-3156.273081
19e-LANL2DZ HW	$p_z$ (-0.39)	$d_{z2}$ (0.49)	$p_z$ (0.59)	-3155.080177
NRECPs				
17e-NR-AIMP	$p_y$ (0.87)	$d_{yz}$ (0.28)	$p_y$ (-0.48)	-3121.384930
17e-NR-AIMP-u	$p_z$ (-0.29)	$d_{z2}$ (0.54)	$p_z$ (0.56)	-3121.390391

Table 3.5-b. Coefficient of single occupied on each basis set and SCF energy at B3LYP level.

Basis sets & ECPs				KS Energy
	Br	Ag	Cl	
All electron				
ANO-RCC	$p_y$ (0.96)			-8382.020131
ANO-DK3	$p_y$ (0.16)	$d_{yz}$ (0.33)	$p_y$ (-0.94)	-8382.014782
ANO-DK3-u	$p_y$ (0.91)	$d_{yz}$ (0.16)	$p_y$ (-0.31)	-8382.047948
RECPs				
17e-CG-AIMP	$p_y$ (-0.98)	$d_{yz}$ (-0.18)	$p_y$ (0.07)	-3125.888722
17e-CG-AIMP-u	$p_y$ (-0.98)	$d_{yz}$ (-0.23)	$p_y$ (0.08)	-3125.994490
19e-NP-AIMP	$p_y$ (-0.96)	$d_{yz}$ (-0.32)	$p_y$ (0.20)	-3160.286745
19e-MWB Dolg	$p_y$ (-0.97)	$d_{yz}$ (-0.18)	$p_y$ (0.20)	-3159.660398
19e-LANL2DZ HW	$p_y$ (0.09)	$d_{yz}$ (0.23)	$p_y$ (-0.96)	-3158.066841
NRECPs				
17e-NR-AIMP	$p_y$ (-0.37)	$d_{yz}$ (-0.32)	$p_y$ (0.91)	-3125.742052
17e-NR-AIMP-u	$p_y$ (0.97)	$d_{yz}$ (0.19)	$p_y$ (-0.07)	-3125.724297

**Table 3.6.** Total energies, Mulliken charges and schematic wavefunction in terms of molecular orbitals corresponding to the low-lying doublet electronic states calculated at MS-CASPT2/CASSCF level of theory by ANO-RCC basis sets for all the atoms corresponding to the  $^2A'$  and  $^2A''$  at 21 electrons in 11 active orbitals.

MS-CASPT2/7-SA-CAS(21,11) $^2A'$						
CASSCF (a.u.)	SS- CASPT2 (a.u.)	Single occupied orbitals	MS- CASPT2 (a.u.)	Mulliken charge		
				Br	Ag	Cl
-8377.146830	-8377.794174		-8377.79651	-0.44	0.95	-0.52
-8377.131771	-8377.812368		-8377.82061	-0.26	0.69	-0.44
-8377.090166	-8377.758914		-8377.75881	-0.15	0.45	-0.31
-8377.088252	-8377.776611		-8377.77647	-0.16	0.40	-0.24
-8377.058294	-8377.685880		-8377.68587	-0.64	1.35	-0.72
-8377.025213	-8377.712141		-8377.70404	-0.52	1.01	-0.49
-8376.989998	-8377.667052		-8377.66482	-0.43	0.86	-0.43
MS-CASPT2/7-SA-CAS(21,11) $^2A''$						
CASSCF (a.u.)	SS- CASPT2 (a.u.)	Single occupied orbitals	MS- CASPT2 (a.u.)	Mulliken charge		
				Br	Ag	Cl
-8377.133113	-8377.811256		-8377.82242	-0.23	0.72	-0.49
-8377.084076	-8377.775559		-8377.77537	-0.22	0.44	-0.22
-8377.065187	-8377.685556		-8377.68556	-0.66	1.34	-0.68
-8377.025717	-8377.713587		-8377.70262	-0.56	0.93	-0.37





**Table 3.7.** Total energies, Mulliken charges and schematic wavefunction in terms of molecular orbitals corresponding to the low-lying doublet electronic states calculated at MS-CASPT2/CASSCF level of theory by ANO-RCC basis sets for all the atoms corresponding to the  $^2A'$  at 13 electrons in 14 active orbitals and the  $^2A''$  at 7 electrons in 8 active orbitals.

MS-CASPT2/7-SA-CAS(13,14) $^2A'$						
CASSCF (a.u.)	SS- CASPT2 (a.u.)	Single occupied Orbitals	MS- CASPT2 (a.u.)	Mulliken charge		
				Br	Ag	Cl
-8377.236084	-8378.204492		-8378.20905	-0.30	0.58	-0.28
-8377.233719	-8378.188455		-8378.19116	-0.41	0.77	-0.37
-8377.198300	-8378.177703		-8378.17543	-0.16	0.48	-0.32
-8377.189858	-8378.167803		-8378.16758	-0.19	0.50	-0.31
-8377.144701	-8378.093059		-8378.09397	-0.46	0.98	-0.52
-8377.126680	-8378.096247		-8378.09389	-0.42	0.87	-0.46
-8377.086493	-8378.071536		-8378.06822	-0.36	0.77	-0.41
MS-CASPT2/4-SA-CAS(7,8) $^2A''$						
CASSCF (a.u.)	SS- CASPT2 (a.u.)	Single occupied orbitals	MS- CASPT2 (a.u.)	Mulliken charge		
				Br	Ag	Cl
-8377.173336	-8377.230008		-8377.23030	-0.16	0.62	-0.46
-8377.128674	-8377.188504		-8377.18844	-0.28	0.44	-0.17
-8377.094759	-8377.146052		-8377.14605	-0.61	1.25	-0.64
-8377.061763	-8377.117993		-8377.11776	-0.54	0.96	-0.42

**Table 3.8.** Total energies, Mulliken charges and schematic wavefunction in terms of molecular orbitals corresponding to the low-lying doublet electronic states calculated at MS-CASPT2/CASSCF level of theory by MWB basis sets for all the atoms corresponding to the  $^2A'$  and  $^2A''$  21 electrons in 11 active orbitals.

MS-CASPT2/7-SA-CAS(21,11) $^2A'$						
CASSCF (a.u.)	SS- CASPT2 (a.u.)	Single occupied orbitals	MS- CASPT2 (a.u.)	Mulliken charge		
				Br	Ag	Cl
-173.98879	-174.20494		-174.21848	-0.29	0.75	-0.46
-173.97834	-174.21384		-174.20667	-0.06	0.51	-0.45
-173.93800	-174.15589		-174.17528	-0.14	0.40	-0.26
-173.93657	-174.17798		-174.15490	-0.22	0.36	-0.15
-173.90059	-174.11700		-174.12253	-0.42	0.95	-0.53
-173.86785	-174.12447		-174.11699	-0.42	0.83	-0.40
-173.83404	-174.07690		-174.07536	-0.37	0.71	-0.34
MS-CASPT2/4-SA-CAS(21,11) $^2A''$						
CASSCF (a.u.)	SS- CASPT2 (a.u.)	single occupied orbitals	MS- CASPT2 (a.u.)	Mulliken charge		
				Br	Ag	Cl
-173.97838	-174.21572		-174.22151	-0.12	0.58	-0.46
-173.93394	-174.17649		-174.17473	-0.16	0.39	-0.23
-173.90737	-174.11730		-174.12246	-0.42	0.98	-0.56
-173.87108	-174.12649		-174.11730	-0.41	0.82	-0.41

**Table 3.9.** Total energies, Mulliken charges and schematic wavefunction in terms of molecular orbitals corresponding to the low-lying doublet electronic states calculated at MS-CASPT2/CASSCF level of theory by MWB basis sets for all the atoms to the  $^2A''$  at 7 electrons in 8 active orbitals.

MS-CASPT2/4-SA-CAS(7,8) $^2A''$						
CASSCF (a.u.)	SS- CASPT2 (a.u.)	single occupied orbitals	MS- CASPT2 (a.u.)	Mulliken charge		
				Br	Ag	Cl
-174.01945	-174.026118		-174.02642	0.13	0.49	-0.62
-173.98063	-173.993754		-173.99347	-0.47	0.45	0.02
-173.88613	-173.898259		-173.89826	-0.56	1.25	-0.69
-173.86747	-173.880370		-173.88035	-0.53	1.15	-0.62

Transition energies to the low lying  $^4A'$  and  $^4A''$  states of AgClBr are reported Table 3.10.

This transitions correspond mainly to excitations from the occupied orbitals describe in previous Tables to the diffuse Rydberg p-orbitals of the silver.

### 3.3 $AgF_2$

#### 3.3.1 Structures of the metal complexes

The optimization of  $AgF_2$  and  $AgF_2^-$  complexes at MP2, CCSD(T) and B3LYP levels of theory resulted in a collinear structure. The nature of the obtained critical points was verified checking that all frequencies are positive. The equilibrium bond lengths at the vibrational potential minimum between the metal and the halogen atoms are collected in Table 3.11, together with the experimental  $AgF_2$  bond distances for reference. The experimental structure was solved by Patterson methods. The calculated bond distance by MP2 and CCSD(T) methods are in agreement with the experimental value. Based on these points we have chosen the collinear geometry obtained with CCSD(T) for the appearing calculations using the molecular-fixed orientation shown in Fig. 1.

**Table 3.11.** Equilibrium distances (in Å) of the collinear neutral and anion F—Ag—F at different levels of theory.

	neutral $AgF_2$	anion $AgF_2$
$r_{eq}$ (Å)	Ag-F	Ag-F
MP2	1.919	2.061
CCSD(T)	1.926	2.061
B3LYP	1.935	2.046
B3LYP/MWB <sup>a</sup>	1.958	2.06
exp. <sup>b</sup>	--	2.07 <sup>c</sup>

<sup>a</sup>Calculation performed using the MWB RECP in all three atoms.

<sup>b</sup>The experimental values are reported by Patterson methods.

<sup>c</sup>Reference [124]



### 3.3.2. Electronic ground state

The choice of the computational strategy has been motivated by the results of the methodological study performed on AgBrCl. ANO-RCC basis sets have been used for silver and fluorine atoms. Even though the theoretical study of this symmetric molecule is easier than the previous one some nearly degeneracy has occurred at the CASSCF and CASPT2 level.

HF and DFT results are reported in Table 3.11. Like in the previous study reported on AgBrCl the monodeterminantal methods are not adapted to the description of the electronic configuration in this dihalide system. Indeed the HF and KS description do not coincide.

**Table 3.11a.** Electronic configurations and Mulliken charges obtained using HF and ANO-RCC basis sets.

Basis sets	Configuration	Mulliken charges		
		F2	Ag	F1
Neutral AgF <sub>2</sub>				
ANO-RCC	$(4d\pi)^2(4d\sigma)^2(4d\pi)^2(2p_xF1F2)^2(4d\pi)^2(2p_xF1F2)^2(4d\pi)^1$ $(2p_xF1F2)^2(2p_xF1F2)^2(4d\pi)^2(4d\pi)^2$	-0.67	1.34	-0.67

**Table 3.11b.** Electronic configurations and Mulliken charges obtained using B3LYP and ANO-RCC basis sets.



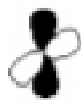








Basis sets	Configuration	Mulliken charges		
		F2	Ag	F1
Neutral AgF <sub>2</sub>				
ANO-RCC	$(2p_xF1)^2(2p_xF1)^2(2p_xF2)^2(4d\pi)^2(4d\pi)^2(4d\pi)^2(4d\sigma)^1$ $(2p_xF2)^2(4d\pi)^2(4d\pi)^2(2p_xF1)^2$	-0.32	1.24	-0.34

**Table 3.11c.** Coefficient of single occupied on each basis set and SCF energy at HF and B3LYP level.

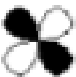



Basis sets				SCF/KS Energy
	F	Ag	F	
ANO-RCC (HF)		$d_{z^2}(-0.79)$		-5510.846382
ANO-RCC (B3LYP)		$d_{z^2}(0.69)$	$2p_z(-0.60)$	-5514.109475

In order to determine the electronic ground state configuration CASSCF/MS-CASPT2 calculations were performed following the same protocol than for AgBrCl. The results are reported in Table XI. The lowest degenerate states  $^2A'$  correspond to the  $(d_{z^2})^1$  electronic configurations and is calculated at -5511.75580 a.u. In contrast to AgBrCl the electronic ground state is not degenerate but still very close to the next pair of  $^2A'/^2A''$  calculated at -5511.75139 a.u. and -551.75109 a.u. and corresponding to the following electronic configurations  $(p_x(F)/d_{z^2}/p_x(F))^2 (p_x(F)/d_{xz}/p_x(F))^2 (p_y(F)/d_{yz}/p_y(F))^2 (d_{xy})^2 (d_{x^2-y^2})^2 (p_x(F)/p_x(F))^2 (p_z(F)/p_z(F))^2 (p_y(F)/p_y(F))^2 (d_{xz})^2 (d_{yz})^2$ .

**Table 3.13** Total energies, Mulliken charges and schematic wavefunction in terms of molecular orbitals corresponding to the low-lying doublet electronic states calculated at MS-CASPT2/CASSCF level of theory by ANO-RCC basis sets for all the atoms to the  $^2A''$  at 7 electrons in 8 active orbitals.

MS-CASPT2/7-SA-CAS(21,11) $^2A'$						
CASSCF (a.u.)	SS- CASPT2 (a.u.)	Single occupied orbitals	MS- CASPT2 (a.u.)	Mulliken charge		
				F	Ag	F
-5510.95461	-5511.75149		-5511.75580	-0.75	1.50	-0.75
-5510.90864	-5511.73793		-5511.75139	-0.73	1.47	-0.73
-5510.85373	-5511.63805		-5511.63805	-0.87	1.75	-0.87
-5510.79978	-5511.66884		-5511.66885	-0.38	0.80	-0.38
-5510.79093	-5511.68670		-5511.68670	-0.40	0.76	-0.40
-5510.75650	-5511.64750		-5511.63404	-0.52	1.03	-0.52
-5510.71724	-5511.59669		-5511.59238	-0.52	1.04	-0.52
MS-CASPT2/4-SA-CAS(21,11) $^2A''$						
CASSCF (a.u.)	SS- CASPT2 (a.u.)	Single occupied orbitals	MS- CASPT2 (a.u.)	Mulliken charge		
				F	Ag	F
-5510.91552	-5511.73354		-5511.75109	-0.74	1.48	-0.74
-5510.86043	-5511.63518		-5511.63518	-0.87	1.73	-0.87
-5510.78806	-5511.68566		-5511.68566	-0.37	0.75	-0.37
-5510.75615	-5511.64655		-5511.62900	-0.50	0.99	-0.50

**Table 3.14.** Total energies, Mulliken charges and schematic wavefunction in terms of molecular orbitals corresponding to the low-lying doublet electronic states calculated at MS-CASPT2/CASSCF level of theory by ANO-RCC basis sets for all the atoms to the  $^2A'$  at 7 electrons in 8 active orbitals.

MS-CASPT2/4-SA-CAS(7,8) $^2A'$						
CASSCF (a.u.)	SS- CASPT2 (a.u.)	Single occupied orbitals	MS- CASPT2 (a.u.)	Mulliken charge		
				F	Ag	F
-5510.97441	-5511.02769		-5511.02770	-0.70	1.41	-0.70
-5510.92475	-5510.97780		-5510.97780	-0.79	1.58	-0.79
-5510.81557	-5510.88010		-5510.88010	-0.32	0.64	-0.32
-5510.79250	-5510.85617		-5510.85617	-0.39	0.79	-0.39

### ***3.4 Conclusion***

The complex electronic structure problem which characterizes XMY molecules has been undertaken under the light of ab initio analysis of AgBrCl and AgF<sub>2</sub> and of their anionic species. These compounds have been found to be collinear at different levels of calculation. The neutral species are characterized by a doublet electronic ground state described by two degenerate <sup>2</sup>A' and <sup>2</sup>A" states in the case of the asymmetric system and by a <sup>2</sup>A' state in AgF<sub>2</sub>. These electronic structures cannot be obtained by means of monodeterminantal methods. It is necessary to treat this problem by multiconfigurational SCF methods completed by a perturbational approach including the dynamical correlation effects. This study demonstrates that the size of the molecule is not necessarily the bottleneck of the quantum chemical study and that the investigation of three-atomic systems may need very complicated and costly calculations beyond the present computational capabilities.

Symmetry blocked CASSCF /MS-CASPT2 calculations have enabled us to obtain the low-lying <sup>4</sup>A' and <sup>4</sup>A" electronic states describing the electronic spectroscopy of the neutral molecules.





## Conclusion

The purpose of this work was to investigate the potential of computational tools at studying various problems of chemistry such as electron transport in large polycyclic aromatic hydrocarbons (PAH) networks, luminescence and electron transfer processes in ruthenium complexes intercalated in biological environment and electronic structure analysis in three atomic silver compounds.

In the first case the challenge is the understanding of the role of metal-based catalysts in the growing of nanotubes. The electronic structure of different classes of PAH has been investigated by means of semi-empirical methods. The trends related to the amount, type and routes of electron transfer in the network in term of groups of atoms pairs have been deduced from the theoretical study. The use of semi-empirical methods correctly parametrized is a good compromise when dealing with this type of problem in large systems.

The second topics was related to the theoretical study of photophysical properties in large Ru(II) complexes used as intercalators in DNA within the context of molecular switches research. Previous studies performed in the Laboratoire de Chimie Quantique (Strasbourg) have shown that the Density Functional Theory may help at analysing absorption spectroscopy in these molecules within the limit of a correct description of charge transfer states which has to be validated by experimental data. In the present field, characterized by an intense experimental activity since the early 90's TD-DFT was the method of choice. Eventhough ab initio calculations can be performed nowadays on these molecules, the severe compromises which have to be done and their cost make them inappropriate. Our calculations have put in evidence for the first time the difference between the absorption/emission spectroscopy of the two most studied complexes, namely  $[\text{Ru}(\text{TAP})_2\text{dppz}]^{2+}$  and  $[\text{Ru}(\text{phen})_2\text{dppz}]^{2+}$ . In particular it has been shown that the lowest part of their spectra differ by the presence or not of IL ( $\pi^*\text{dppz} \rightarrow \pi^*\text{dppz}$ ) absorbing states. These states responsible for an electron density deficiency at



the end of the long intercalated dppz ligand may favorize electron transfer from a guanine to the Ru(II) complex quenching the luminescence process. In contrast when the lowest part of the absorption spectrum is made exclusively of MLCT states the luminescent process will become more efficient. Further work should be devoted to environment effects: effects of water, acetonitrile and biological environment on the observed photophysics. Indeed the large number of available experimental data has to be rationalized. Preliminary calculations have been performed in this direction and open the route to a new field of theoretical investigations.

In the last part of the thesis the difficult problem of accurate electronic structure calculations in small three atomic silver compounds has been undertaken. It is shown that the description of electronic structure in small transition metal molecules cannot get away from highly correlated multiconfigurational methods. HF and DFT approaches based on various basis sets associated either to all-electrons scheme or to pseudopotentials lead to erratic behaviors. Large Relativistic Atomic Natural Orbitals are necessary to get some stability in the mono-determinantal response. Moreover several nearly degenerate states need to be described by large CASSCF/MS-CASPT2 methods in order to determine without any ambiguity the electronic ground state of the neutral species. The very scarce experimental data on these compounds add some difficulties. Whereas the asymmetric AgBrCl molecule has not been detected experimentally, AgF<sub>2</sub> does exist. It could be explained by the description of their electronic ground states, namely two degenerate <sup>2</sup>A' and <sup>2</sup>A" (AgBrCl) and a single <sup>2</sup>A' state in AgF<sub>2</sub>.

This thesis gives an illustration of the limits of various methods of quantum chemistry, not only due to computer facilities, but also to theoretical developments. It is especially very difficult to treat excited states coherently and there is actually no ideal method able to take up this challenge.





## Bibliography

[1] S. Iijima, T. Ichihashi, *Nature* 363 603 (1993).

[2] D.M.Roundhill. Photochemistry and photophysics of metal complexes. New York, Plenum, 1994 *Modern inorganic chemistry*.

[3] C. W. Bauschlicher, Jr., B. Roos, *J.Chem.Phys.*, 91, 4785,(1989)

[4] M. J. Frisch, G. W. Trucks, H. B. Schlegel, G. E. Scuseria, M. A. Robb, J. R. Cheeseman, V. G. Zakrzewski, J. A. Montgomery, Jr., R. E. Stratmann, J. C. Burant, S. Dapprich, J. M. Millam, A. D. Daniels, K. N. Kudin, M. C. Strain, O. Farkas, J. Tomasi, V. Barone, M. Cossi, R. Cammi, B. Mennucci, C. Pomelli, C. Adamo, S. Clifford, J. Ochterski, G. A. Petersson, P. Y. Ayala, Q. Cui, K. Morokuma, P. Salvador, J. J. Dannenberg, D. K. Malick, A. D. Rabuck, K. Raghavachari, J. B. Foresman, J. Cioslowski, J. V. Ortiz, A. G. Baboul, B. B. Stefanov, G. Liu, A. Liashenko, P. Piskorz, I. Komaromi, R. Gomperts, R. L. Martin, D. J. Fox, T. Keith, M. A. Al-Laham, C. Y. Peng, A. Nanayakkara, M. Challacombe, P. M. W. Gill, B. Johnson, W. Chen, M. W. Wong, J. L. Andres, C. Gonzalez, M. Head-Gordon, E. S. Replogle, and J. A. Pople, *Gaussian 98*. Gaussian, Inc., Pittsburgh PA, 2001.

[5] M. J. Frisch, G. W. Trucks, H. B. Schlegel, G. E. Scuseria, M. A. Robb, J. R. Cheeseman, J. A. Montgomery, Jr., T. Vreven, K. N. Kudin, J. C. Burant, J. M. Millam, S. S. Iyengar, J. Tomasi, V. Barone, B. Mennucci, M. Cossi, G. Scalmani, N. Rega, G. A. Petersson, H. Nakatsuji, M. Hada, M. Ehara, K. Toyota, R. Fukuda, J. Hasegawa, M. Ishida, T. Nakajima, Y. Honda, O. Kitao, H. Nakai, M. Klene, X. Li, J. E. Knox, H. P. Hratchian, J. B. Cross, V. Bakken, C. Adamo, J. Jaramillo, R. Gomperts, R. E.

Stratmann, O. Yazyev, A. J. Austin, R. Cammi, C. Pomelli, J. W. Ochterski, P. Y. Ayala, K. Morokuma, G. A. Voth, P. Salvador, J. J. Dannenberg, V. G. Zakrzewski, S. Dapprich, A. D. Daniels, M. C. Strain, O. Farkas, D. K. Malick, A. D. Rabuck, K. Raghavachari, J. B. Foresman, J. V. Ortiz, Q. Cui, A. G. Baboul, S. Clifford, J. Cioslowski, B. B. Stefanov, G. Liu, A. Liashenko, P. Piskorz, I. Komaromi, R. L. Martin, D. J. Fox, T. Keith, M. A. Al-Laham, C. Y. Peng, A. Nanayakkara, M. Challacombe, P. M. W. Gill, B. Johnson, W. Chen, M. W. Wong, C. Gonzalez, and J. A. Pople, *Gaussian 03*. Gaussian, Inc., Wallingford CT, 2004.

[6] K. Andersson, M. Barysz, A. Bernhardsson, M. R. A. Blomberg, Y. Carissan, D. L. Cooper, M. P. Fülscher, L. Gagliardi, C. de Graaf, B. A. Hess, D. Hagberg, G. Karlström, R. Lindh, P.-Å. Malmqvist, T. Nakajima, P. Neogrády, J. Olsen, J. Raab, B. O. Roos, U. Ryde, B. Schimmelpfennig, M. Schütz, L. Seijo, L. Serrano-Andrés, P. E. M. Siegbahn, J. Stålring, T. Thorsteinsson, V. Veryazov, P.-O. Widmark. *MOLCAS 6.0*, Department of Theoretical Chemistry, Lund University, Sweden 2004.

[7] Paul von Raugé Schleyer et al. *Encyclopedia of computational chemistry*. 1997, John Wiley & Sons

[8] C. C. J. Roothan, *Rev. Mod. Phys.* 23, 69(1951).

[9] J. A. Pople and R. K. Nesbet, *J. Chem. Phys.* 22, 571 (1954).

[10] R. McWeeny and G. Dierksen, *J. Chem. Phys.* 49, 4852 (1968).

[11] P.-Å. Malmqvist and B. O. Roos. *Chem. Phys. Letters*, 155:189, (1989).

[12] Trigve Helgaker, Poul Jorgensen, Jeppe Olsen, *Molecular Electronic-Structure Theory* John Wiley & Sons Inc

[13] Björn O. Roos and Per-Olof Widmark, Eds. *European Summerschool in Quantum Chemistry Book I, II, III*

[14] Computational Chemistry

[15] J. B. Foresman, M. Head-Gordon, J. A. Pople, and M. J. Frisch, *J. Phys. Chem.* 96, 135 (1992).

- [16] M. Head-Gordon, J. A. Pople, and M. J. Frisch, *Chem. Phys. Lett.* 153, 503 (1988).
- [17] M. J. Frisch, M. Head-Gordon, and J. A. Pople, *Chem. Phys. Lett.* 166, 275 (1990).
- [18] M. J. Frisch, M. Head-Gordon, and J. A. Pople, *Chem. Phys. Lett.* 166, 281 (1990).
- [19] M. Head-Gordon and T. Head-Gordon, *Chem. Phys. Lett.* 220, 122 (1994).
- [20] S. Saebo and J. Almlöf, *Chem. Phys. Lett.* 154, 83 (1989).
- [21] K. Andersson, P.-Å. Malmqvist, B. O. Roos, A. J. Sadlej, and K. Wolinski, *J. Phys. Chem.*, 94, 5483, (1990).
- [22] K. Andersson, P.-Å. Malmqvist, and B. O. Roos. *J. Chem. Phys.*, 96,1218, (1992).
- [23] B. O. Roos and K. Andersson, *Chem. Phys. Letters*, 245:215, (1995).
- [24] B. O. Roos, K. Andersson, M. P. Fülcher, L. Serrano-Andrés, K. Pierloot, M. Merchán, and V. Molina, *J. Mol. Struct. Theochem*, 388, 257, (1996).
- [25] J. Cizek, *Adv. Chem. Phys.* 14, 35 (1969).
- [26] G. D. Purvis and R. J. Bartlett, *J. Chem. Phys.* 76, 1910 (1982).
- [27] G. E. Scuseria, C. L. Janssen, and H. F. Schaefer III, *J. Chem. Phys.* 89, 7382 (1988).
- [28] G. E. Scuseria and H. F. Schaefer III, *J. Chem. Phys.* 90, 3700 (1989).
- [29] P. Hohenberg and W. Kohn, *Phys. Rev.* 136, B864 (1964).
- [30] W. Kohn and L. J. Sham, *Phys. Rev.* 140, A1133 (1965).
- [31] R. G. Parr and W. Yang, *Density-functional theory of atoms and molecules* Oxford Univ. Press, Oxford, (1989).
- [32] R. E. Stratmann, G. E. Scuseria, and M. J. Frisch, *J. Chem. Phys.* 109, 8218 (1998).

- [33] R. Bauernschmitt and R. Ahlrichs, *Chem. Phys. Lett.* 256, 454 (1996).
- [34] M. E. Casida, C. Jamorski, K. C. Casida, and D. R. Salahub, *J. Chem. Phys.* 108, 4439 (1998).
- [35] J. J. P. Stewart, *MOPAC 2000*, Fujitsu Limited, Japan (1999).
- [36] F. Maseras and K. Morokuma, *J. Comp. Chem.* 16, 1170 (1995).
- [37] S. Humbel, S. Sieber, and K. Morokuma, *J. Chem. Phys.* 105, 1959 (1996).
- [38] T. Matsubara, S. Sieber, and K. Morokuma, *Int. J. Quant. Chem.* 60, 1101 (1996).
- [39] M. Svensson, S. Humbel, R. D. J. Froese, T. Matsubara, S. Sieber, and K. Morokuma, *J. Phys. Chem.* 100, 19357 (1996).
- [40] M. Svensson, S. Humbel, and K. Morokuma, *J. Chem. Phys.* 105, 3654 (1996).
- [41] S. Dapprich, I. Komáromi, K. S. Byun, K. Morokuma, and M. J. Frisch, *J. Mol. Struct. Theochem* 462, 1 (1999).
- [42] T. Vreven and K. Morokuma, *J. Comp. Chem.* 21, 1419 (2000).
- [43] S. Miertus, E. Scrocco, and J. Tomasi, *Chem. Phys.* 55, 117 (1981).
- [44] B. Mennucci and J. Tomasi, *J. Chem. Phys.* 106, 5151 (1997).
- [45] J. Tomasi, B. Mennucci, and E. Cancès, *J. Mol. Struct. Theochem* 464, 211 (1999).
- [46] M. Cossi, V. Barone, B. Mennucci, and J. Tomasi, *Chem. Phys. Lett.* 286, 253 (1998).
- [47] R. Robinson, *J. Soc. Chem. Ind.* 44, 456-458 (1925).
- [48] R. Robinson, *Outline of an Electrochemical Theory of the Course of Organic Reactions*; Inst. Chem. Great Britain and Ireland: London, (1932).
- [49] C. K. Ingold, *Principles of an Electron Theory of Organic Reactions*. Chem. Rev.

15, 225-274 (1934).

[50] C. K. Ingold, *Structure and Mechanism in Organic Chemistry*, Cornell University Press: Ithaca, (1953).

[51] S. J. Cyvin,; I. Gutman. *Kekulé Structures in Benzenoid Hydrocarbons*; Lecture Notes in Chemistry 46; Springer: Berlin, (1988).

[52] Y. Shibuta and S. Maruyama. *Physica B* 323, 187–189, (2002).

[53] A. Thess, R. Lee, P. Nikolaev, H. Dai, P. Petit, J. Robert, C. Xu, Y.H. Lee, S.G Kim, A.G Rinzler, D.T. Colbert, G.E. Scuseria, D. Tománek, J.E. Fischer, R.E. Smalley, *Science* 273 483 (1996).

[54] C. Journet, W.K. Maser, P. Bernier, A. Loiseau, M.L. de la Chapelle, S. Lefrant, P. Deniard, R. Lee, J.E. Fisher, *Nature* 388 756 (1997)

[55] H. Dai, A.G Rinzler, P. Nikolaev, A. Thess, D.T. Colbert, R.E. Smalley, *Chem. Phys. Lett.* 260 471 (1996).

[56] A.M. Cassell, J.A. Raymakers, J. Kong, H. Dai, *J. Phys. Chem. B* 103 6484 (1999).

[57] S. Maruyama, R. Kojima, Y. Miyauchi, S. Chiashi, M.Kohno, *Chem. Phys. Lett.* 360 229 (2002).

[58] M.J. Bronikowski, P.A. Willis, D.T. Colbert, K.A. Smith, R.E. Smalley, *J. Vac. Sci. Technol. A* 19 1800 (2001).

[59] M. Yudasaka, R. Yamada, N. Sensui, T. Wilkins, T. Ichihashi, S. Iijima, *J. Phys. Chem. B* 103 6224 (1999).

[60] H. Kataura, Y. Kumazawa, Y. Maniwa, Y. Ohtsuka, R. Sen, S. Suzuki, Y. Achiba, *Carbon* 38 1691 (2000).

[61] S.L. Laira, W.C. Herndon, L.E. Murra, S.A. Quinones, End cap nucleation of carbon nanotubes *Carbon* 44, 3 447 (2006).

[62] S. Maruyama, R. Kojima, Y. Miyauchi, S. Chiashi and M. Kohno, *Chem. Phys. Lett.*,



360, 3-4 229 (2002).

[63] Y. Murakami, Y. Miyauchi, S. Chiashi and S. Maruyama, *Chemical Physics Letters*, 374, 1-2, 53 (2003).

[64] S. Chiashi , Y. Murakami , Y. Miyauchi and S. Maruyama, *Chemical Physics Letters*, 386, 1-3, 89 (2004).

[65] Y. Miyauchi , S. Chiashi , Y. Murakami , Y. Hayashida and S. Maruyama, *Chemical Physics Letters*, 387, 1-3, 198 (2004).

[66] X. Guo, J.B. Wang and H.W. Zhang, *International Journal of Solids and Structures*, 43, 1276 (2006).

[67] M. Vaezzadeh, E. Noruzifar, S. F. Atashzar, M. Vaezzadeh and M. Ahmadi, *Chemical Physics Letters*, In Press,

[68] Marvin L. Cohen, *Nanoscience: The quantum frontier Physica E* 29 447 (2005).

[69] H. Hosoya, S. Iwata, M. Murokoshi, and M. Atsumi *J. Chem. Inf. Comput. Sci.* 41, 512-516 (2001).

[70] <http://wikipedia.org/>

[71] A. E. Friedman, J-C. Chambron, J-P. Sauvage, N. J. Turro, and J. K. Barton *J. Am. Chem. Soc.* 112, 4960 (1990)

[72] R. M. Hartshorn and J. K. Barton *J. Am. Chem. SOC.* 114, 5919 (1992).

[73] Y. Jenkins, A. E. Friedman, N. J. Turro and J. K. Barton *Biochemistry* 31, 10809 (1992).

[74] P. Lincoln and B. Nordén *J. Phys. Chem. B* 102, 9583 (1998)

[75] P. Lincoln, A. Broo, and B. Nordén *J. Am. Chem. Soc.* 118, 2644, (1996)

[76] I. Ortman, S. Content, N. Boutonnet, A. K DeMesmaeker, W. Bannwarth, J.-F. Constant, E. Defrancq, and J. Lhomme *Chem. Eur. J.*, 5, 2712 (1999)

- [77] C. G. Coatesa, P. Callaghana, J. J. McGarvey, J. M. Kelly, L. Jacquet and A. K. De Mesmaecker *Journal of Molecular Structure* 598, 15, (2001).
- [78] J. M. Kelly, C. M. Creely, M. M. Feeney, S. Hudsona, W. J. Blaub, B. Elias, A. K. DeMesmaecker, P. Matousek, M. Towrie, and A. W. Parker *Central Laser Facility Annual Report* 111 (2001/2002)
- [79] J.K.Barton, *Science*. 233, 727 (1986)
- [81] Q.L. Zhang, J. H. Liu, J. Z. Liu, P. X. Zhang, X. Z. Ren, Y Liu, Y Huang, L.N Ji, *Journal of Inorganic Biochemistry* 98, 1405 (2004)
- [80] R. Blasius, C. Moucheron, and A. K. DeMesmaecker *Eur. J. Inorg. Chem.* 3971 (2004).
- [82] J. G. Liu, B. H. Ye, H. Li, Q. X. Zhen a, L. N. Ji, Y. H. Fu. *Journal of Inorganic Biochemistry* 76 265 (1999).
- [83] J-P Lecomtet, A. K. DeMesmaecker, M. M. Feeney and J. M. Kelly. *Inorg. Chem.* 34, 6481 (1995)
- [84] Y. Jenkins, A. E. Friedman, N. J. Turro and J. K. Barton. *Biochemistry* 31 10809 (1992)
- [85] I. Ortmans, B. Elias, J. M. Kelly, C. Moucheron and A. K. DeMesmaecker. *Dalton Trans* 668 (2004).
- [86] C. G. Coastes, P. Callaghan, J. J.McGarvey, John M. Kelly, Luc Jacquet, A.Kirsch-De Mesmaecker, *Journal of Molecular Structure* 598 (2001)
- [87] D. Han, H. Wang, N. Ren *Journal of Molecular Structure (Theochem)* 711, 185 (2004)
- [88] C. Lee, W. Yang, and R. G Parr. *Phys. Rev.* B37 385 (1988)
- [89] D. Andrae, U. Haussermann, M. Dolg, and H. Preuss, *Theor. Chim. Acta*, 77, 123 (1990).

- [90] R. Ditchfield, W. J. Hehre, and J. A. Pople. *J. Chem. Phys.* 54, 724 (1971).
- [91] G. A. Petersson and M. A. Al-Laham. *J. Chem. Phys.* 94, 6081 (1991).
- [92] T. H. Dunning Jr. and P. J. Hay, in *Modern Theoretical Chemistry*, Ed. H. F. Schaefer III, Vol. 3 (Plenum, New York, 1976) 1-28.
- [93] H. Ohishi, K. Suzuki, M. Ohtsuchi, T. Hakoshima and A. Rich. *FEBS Lett.* 523, 29 (2002). <http://ndbserver.rutgers.edu/atlas/xray/structures/Z/zd0003/zd0003.html>
- [94] <http://winmostar.com/>
- [95] [http://www1.bbiq.jp/zzzfelis/Facio\\_Jp.html](http://www1.bbiq.jp/zzzfelis/Facio_Jp.html)
- [96] Babel version 1.6 Copyright (C) 1992-1996 by Pat Walters and Matt Stahl Dolata Research Group, Department of Chemistry, University of Arizona, Tucson, AZ 85721. <http://smog.com/chem/babel/>
- [97] A. S. F. Osvaldo, F. V. Daniel. *Biorg. Med. Chem. Lett.* 13 1797 (1997)
- [98] E. J. C. Olson, D. Hu, A. Hörmann, A. M. Jonkman, M. R. Arkin, E. D. A. Stemp, J. K. Barton, and P. F. Barbara *J. Am. Chem. Soc.* 119, 11458-11467 (1997)
- [99] A. Dreuw, J. L. Weisman, and M. Head-Gordon *J. Chem. Phys.*, 119, 6 (2003).
- [100] A. Dreuw and M. Head-Gordon *J. Am. Chem. Soc.* 126, 4007 (2004).
- [101] J E Enderby, and A C Barnes, *Rep. Prog. Phys.* 53, 85 (1990)
- [102] I. Ebbjo, P. Vanhishta, R. Dejus, and K. Skold, *J. Phys. Chem.* 20, 441 (1987)
- [103] R. S. Mulliken, *Phys. Rev.* 51, 310 (1937)
- [104] R. M. Clements and R. F. Barrow, *Chem. Comm. (London)*, 1, 27 (1968);
- [105] R. F. Barrow, and R. M. Clements, *Proc. R. Soc. London Ser. A* 322, 243 (1971)

- [106] J. Hoefl, F. J. Lovas, E. Tiemann, and T. Topping, *Z. Naturforsch. A* 25, 35 (1970).
- [107] A. Ramirez-Solis, *J. Chem. Phys.* 117, 1047 (2002)
- [108] A. Ramirez-Solis, and J. Schamps, *J. Chem. Phys.* 102, 4482 (2005)
- [109] H. Wang, and J. L. Gole, *J. Chem. Phys.* 98, 9311 (1993)
- [110] J. Frank, and H. Kuhn, *Z. Phys.* 44, 607 (1927)
- [111] G. J. Stueber, M. Foltin, and E. R. Bernstein, *J. Chem. Phys.* 109, 9831 (1998).
- [112] B. Dekel, Z. Barkay, and A. Katzir, *Opt. Comm.* 199, 383 (2001).
- [113] G. A. Petersson and M. A. Al-Laham, *J. Chem. Phys.* 94, 6081 (1991).  
0 (1980).
- [114] G. A. Petersson, A. Bennett, T. G. Tensfeldt, M. A. Al-Laham, W. A. Shirley, and J. Mantzaris, *J. Chem. Phys.* 89, 2193 (1988).
- [115] A. D. McLean and G. S. Chandler, *J. Chem. Phys.* 72, 5639 (1980).
- [116] R. Krishnan, J. S. Binkley, R. Seeger, and J. A. Pople, *J. Chem. Phys.* 72, 65
- [117] B. O. Roos, R. Lindh, P.-A. Malmqvist, V. Veryazov, and P.-O. Widmark, *J. Phys. Chem. A* 108, 2851 (2004)
- [118] B. O. Roos *Not Published yet* (2005)
- [119] T. Tsuchiya, M. Abe, T. Nakajima and K. Hirao, *J. Chem. Phys.*, 115, 4463 (2001);
- [120] P.J. Hay and W.R. Wadt, *J. Chem. Phys.* 82, 299 (1985)
- [121] Z. Barandiaran, L. Seijo, S. Huzinaga, *J. Chem. Phys.* 93, 5843 (1990)
- [122] F. Rakowitz, C. M. Marian, and L. Seijo, *J. Chem. Phys.*, to appear

[123] E. Pearson, and W. Gordy, *Phys. Rev.* 152, 42 (1966)

[124] P. Fischer, *Journal of Physics and Chemistry of Solids*, 32, 543 (1971)

[125] J. Bossert. *Spectroscopie électronique et photochimie de complexes à transfert de charge du rhénium et du ruthénium*. Thèse de Doctrat, Université Louis Pasteur, Strasborug, 2004.

[126] S. Villaume. *Electronic spectroscopy and photochemistry of small transition metal complexes studied via coupled cluster calculations and wavepacket propagation*. Thèse de Doctrat, Université Louis Pasteur, Strasborug, 2005.